UCRL-53870
Distribution Category UC-420

UCRL--53870

DE88 013164

Measurements of Radial Profiles of Ion Cyclotron Resonance Heating on the Tandem Mirror Experiment-Upgrade

Steven Falabella

P.h.D. Thesis

Manuscript date: May 11, 1988

LAWRENCE LIVERMORE NATIONAL LABORATORY
University of California • Livermore, California • 94550

eb

Measurements of Radial Profiles of Ion Cyclotron Resonance Heating on the Tandem Mirror Experiment-Upgrade

By

Steven Falabella

B.S., (University of Lowell) 1980
M.S., (University of California, Davis) 1982

DISSERTATION

Submitted in partial satisfaction of the requirements for the degree of

DOCTOR OF PHILOSOPHY

in

Engineering - Applied Science

in the

GRADUATE DIVISION

of the

UNIVERSITY OF CALIFORNIA - DAVIS

Approved:

Richard F. Post

Gary R Smith

Hans L Fick

Committee in Charge

Measurements of Radial Profiles of Ion Cyclotron Resonance Heating on the Tandem Mirror Experiment-Upgrade

Steven Falabella
University of California - Davis
Department of Applied Science
Livermore, California 94550

May 11, 1988

ABSTRACT

A small Radial Energy Analyzer (REA) was used on the Tandem Mirror Experiment-Upgrade (TMX-U), at Lawrence Livermore National Laboratory, to investigate the radial profiles of ion temperature, density, and plasma potential during Ion Cyclotron Resonance Heating (ICRH). The probe has been inserted into the central-cell plasma at temperatures of 200 eV and densities of $3 \times 10^{12} cm^{-3}$ without damage to the probe, or major degradation of the plasma. This analyzer has indicated an increase in ion temperature from near 20 eV before ICRH to near 150 eV during ICRH, with about 60 kW of broadcast power. The REA measurements were cross-checked against other diagnostics on TMX-U and found to be consistent. The ion density measurement was compared to the line-density measured by microwave interferometry and found to agree within 10 to 20%. A radial integral of $n_i T_i$ as measured by the REA shows good agreement with the diamagnetic loop measurement of plasma energy. The radial density profile is observed to broaden during the RF heating pulses, without inducing additional radial losses in the core plasma. The radial profile of plasma potential is seen to

vary from axially peaked, to nearly flat as the plasma conditions varied over the series of experiments. To relate the increase in ion temperature to power absorbed by the plasma, a power balance as a function of radius was performed. The RF power absorbed is set equal to the sum of the losses during ICRH, minus those without ICRH. This method accounts for more than 70% of the broadcast power using a simple power balance model. The measured radial profile of the RF heating was compared to the calculations of two codes, ANTENA and GARFIELD, to test their effectiveness as predictors of power absorption profiles for TMX-U.

Acknowledgements

I would like to express my appreciation to everyone that has made this project possible. First and foremost I would like to thank Dr. Arthur W. Molvik for his continued advice and guidance throughout this project. He always took the time to provide critical review of my work, and to point me in more productive directions when needed.

I would also like to thank all the members of the TMX-U physics staff especially Drs. Steve Allen, Jamie Barter, Tom Casper, Fred Coensgen, Don Correll, Bill Cummins, Guy Dimonte, Jim Foote, Dave Hill, Bear Hornady, Robert Horton, Reed James, and Tom Simonen, for their support in carrying out this research.

This project could not have been completed without the talents and efforts of the entire TMX technical staff, but I must give special thanks for the contributions of Don Antelman, Walter Ferguson, Al Henderson, Bob Philbrook, and Dennis Scofield, who kept everything in the ICRH system working.

I would also like to acknowledge the support and guidance the Department of Applied Science faculty and staff, especially Ms. Donna Clifford and the late Dr. Abraham Goldberg, from whom I have learned so very much.

For many productive discussions along the way, I would like to thank my fellow classmates and friends especially Leon Berzins, Bruce Bogohsian, Mike Carter, Scott Ducar, and Robert White. Thanks also to the people behind LaTeX, and fellow students for the development of the thesis style used to generate this document.

For their continuing support and encouragement, special thanks to my parents, Benjamin and Martha Falabella, who always knew I could do it. Finally, above all, I would like to thank my wife, Lauri, who came into my life just when I needed her.

What is essential

is invisible to the eye.

- Antione de Saint-Exupéry

Contents

List of Figures

List of Tables

Chapter 1

Introduction

1.1 Overview

Nuclear fusion, the joining of two light nuclei to form a heavier element, has the potential to become an almost inexhaustible source of energy for man's needs. Research in fusion has always had the eventual goal of generating electric power. Any new ideas or breakthroughs must be examined in that light. The basic process of fusing two nuclei has been demonstrated repeatedly in the laboratory, but always at the expense of much more energy than is released in the reaction. If the reactants can be heated and confined together long enough, net *thermonuclear* fusion energy can be produced.

Currently, there are three main approaches to the problem of confinement. The first relies on gravity to compress and heat. This takes place in the heart of stars, but cannot be scaled down to terrestrial proportions. The second relies on the inertia of the reactants. If the proper isotopes can be compressed and heated with great force, enough fusion reactions can take place before the whole assembly has time to expand and cool. This was first demonstrated with the detonation of the H-bomb, which required a small fission bomb to compress and ignite. On a smaller scale, powerful lasers can be focused onto tiny capsules of deuterium and tritium, the two isotopes of hydrogen that are the easiest to fuse, to compress

and heat them to thermonuclear conditions. Although fusion conditions have been produced, current experiments consume many times more energy than is released. The third approach utilizes magnetic fields in evacuated chambers to contain the hot, ionized gases while they are heated. Although they are not yet net producers of energy, magnetic confinement devices are getting close to breakeven conditions.

One of the promising configurations for magnetic-confinement fusion research is the tandem mirror. In its most basic form, the tandem mirror consists of a long, straight solenoidal cell with smaller, high field *mirror* cells at either end. These mirror cells provide both magnetic and electrostatic confinement for the center-cell ions. The Tandem Mirror Experiment-Upgrade, (TMX-U), at Lawrence Livermore National Laboratory (LLNL), was the first tandem mirror to investigate the practicality of tailoring the axial potential profile to provide isolation between end-cell and central-cell electron populations. This concept, the thermal barrier, enables the potential in the end-cells to increase without having to increase the electron temperature in the entire device, a large savings in power. The thermal barrier, while effective on electrons, acts as a potential well for ions. To maintain the barrier, ions that scatter and trap there must be selectively removed. If one can increase the temperature of ions passing through the barrier from the central cell, the scattering rate into the barrier can be reduced, and requirements on removal relaxed. It is the purpose of Ion Cyclotron Resonance Heating (ICRH) to heat the central-cell ions in TMX-U and reduce the rate of collisional filling. However, the physics of ICRH is complicated. To assess its effect .ess, code modeling and experimental measurements must be employed. It is the goal of this dissertation to measure the radial profile of ion heating in the central-cell of TMX-U, and compare this profile to code predictions.

Toward this goal, the Radial Energy Analyzer (REA) was implemented on

TMX-U to investigate the radial profiles of ion temperature, density, and plasma potential during ICRH.

1.2 Outline

This dissertation is divided into nine chapters and three appendices. This chapter gives an overview of the problems addressed in the subsequent chapters. Chapter 2 provides a brief description of the physics governing the operation of a tandem mirror, and describes the TMX-U facility. Also, included is a brief description of the diagnostics used in calibrating the REA, and those providing measurements required to calculate the radial profile of ion heating. Ion Cyclotron Resonance Heating is discussed in Chapter 3, as well as the RF system used on TMX-U. A brief discussion of wave propagation in a bounded plasma is also presented. The two codes used to calculate the RF fields and power absorption in the plasma are introduced as well.

Chapter 4 covers the theory and design of the REA system as implemented on TMX-U. The REA probe head and the front-end electronics were obtained from TRW, but the sweep voltage supply and data acquisition system were developed and constructed at LLNL for this project. Chapter 5 describes the data analysis techniques used to deduce the ion temperature, density, and plasma potential from the traces of tip-current vs. time and tip-voltage vs. time. Chapter 6 gives an account of the calibration of the REA against other diagnostics available on TMX-U. Where possible, measurements made by the REA are compared with measurements made by other diagnostic techniques. The measurements from each are found to be equal, within reasonable experimental uncertainties. Other supporting diagnostic data are also shown. Chapter 7 contains the radial profiles obtained by the REA under several different plasma conditions. Correlations between profile shape and

plasma heating and fueling variations are noted.

To relate the ion temperature profiles to ion heating profiles, a power balance was performed. Chapter 8 contains the description of the power balance model used, and the resultant ion heating profiles. These are compared to the heating profiles predicted by two modeling codes. Chapter 9 summarizes the results of this endeavor, and suggests additional applications for the REA. Appendix A describes a code written to investigate the effects of space-charge within the REA tip. Appendix B lists, in table form, the numerical values for all the terms used in the power balance performed in Chapter 8. Appendix C lists the input decks for the code runs used in the comparisons.

Chapter 2

Tandem Mirror Physics

2.1 Introduction

The tandem mirror approach to magnetic confinement was proposed independently by both Fowler and Logan[1], and Dimov[2] in 1976. The concept seeks to utilize the large potentials generated in single-cell magnetic mirrors to provide axial confinement for a long, straight solenoid. The relative simplicity of a straight solenoid compared to toroidal configurations could mean significant engineering and economic advantages for the tandem mirror. The success of the tandem mirror, however, relies on creating the axial confining potentials simply and inexpensively. The physics of a tandem mirror can best be explained by first reviewing the principles governing the interaction of charged particles with electro-magnetic fields. MKS units will be used throughout, except as noted.

2.2 Mirror Confinement

The force on charged particles in electric and magnetic fields is described by the Lorentz equation:

$$\vec{F} = m\frac{d\vec{v}}{dt} = q(\vec{E} + \vec{v} \times \vec{B}) \tag{2.1}$$

The basic motion of a particle can be described as the sum of three motions: gyration about a magnetic field line, net drift across field lines, and motion along

the direction of the magnetic field.

The gyration of particles in a magnetic field takes place at a frequency and radius determined by the particle's charge, q, mass, m, and velocity perpendicular, $v_\perp$, to the local magnetic field (strength, B). The frequency is expressly independent of the particle's velocity, except for relativistic mass corrections. Gyrofrequency, ω, and radius, ρ, are given by:

$$\omega = \frac{qB}{m} \tag{2.2}$$

$$\rho = \frac{mv_\perp}{qB} \tag{2.3}$$

The center of the particle's gyro-orbit is called the *guiding center*. Under conditions where the gyro. dius is small compared to the scale lengths of the magnetic and electric fields, the motion of the guiding center can be followed instead of the detailed gyromotion. For these conditions, the particle can be treated as located at the guiding center and only the motion of the guiding center followed.

There are a number of *guiding-center drifts*[3], which result from forces perpendicular to the magnetic field. The drift motion due to electric fields perpendicular to the magnetic field, the $\vec{E} \times \vec{B}$ drift, can be treated in this approximation. The $\vec{E} \times \vec{B}$ drift velocity, which is independent of the charge of the particle, is given by:

$$\vec{v}_{drift} = \frac{\vec{E} \times \vec{B}}{B^2} \tag{2.4}$$

Another important guiding-center drift is that resulting from curvature of magnetic field lines. The drift associated with a field line radius of curvature, R_c, can be expressed as:

$$\vec{v}_{curve} = \frac{m}{q} v_\parallel^2 \frac{\vec{R}_c \times \vec{B}}{R_c^2 B^2} \tag{2.5}$$

where: $\vec{R}_c \equiv R_c \hat{r}$, and $\hat{r}$ is a unit vector drawn in the direction from the local center of curvature to the particle position.

The motion of particles along the magnetic field lines[4] is described by the component of Eqn. 2.1 along the field. The component of the electric field in the direction of the magnetic field, $E_{\|}$, accelerates the particles parallel to $\vec{B}$. The force is simply: $qE_{\|}$. In cylindrical coordinates, the radial component of the magnetic field, B_r, provides the force in the parallel direction, equal to: $qv_{\perp}B_r$, where $v_{\perp}$ is the velocity component perpendicular to $\vec{B}$. Assuming that $B_r << B_z$ and using the fact that $\nabla \cdot \vec{B} = 0$, one obtains to first order in B_r:

$$B_r \simeq -\frac{r}{2}\frac{\partial B_z}{\partial z} \tag{2.6}$$

For ease of calculation, one can assume the particle has its guiding center on the z-axis so r is equal to the gyroradius, ρ. Substituting this into the expression for the force yields:

$$F_{\|} = -\frac{q\rho}{2}v_{\perp}\frac{\partial B_z}{\partial z} = -\frac{mv_{\perp}{}^2}{2B}\frac{\partial B_z}{\partial z} = -\mu\frac{\partial B_z}{\partial z} \tag{2.7}$$

where the quantity $(mv_{\perp}{}^2)/(2B)$ is identified as the magnetic moment, μ.

It is this force that is exploited in the magnetic mirror to provide axial confinement. Creating a magnetic field configuration that has higher field strength at both ends than in the middle, can confine plasma within. Fig. 2.1 shows an axial profile of B_z for a simple mirror cell. The mirror trap, however, is not perfect. Particles that have too small a ratio of $v_{\perp}$ to $v_{\|}$ will experience insufficient force to reflect them and they will escape. The *pitch angle* is defined as the inverse tangent of this ratio,

$$\theta = \tan^{-1}(v_{\perp}/v_{\|}). \tag{2.8}$$

The minimum confined pitch angle is called the *loss-cone angle*. The loss-cone angle is determined by the ratio of the maximum to the minimum magnetic field on a particle's trajectory, called the *mirror ratio*, R_m. This angle can be calculated using the fact that energy is conserved, and that the magnetic moment, μ, is invariant

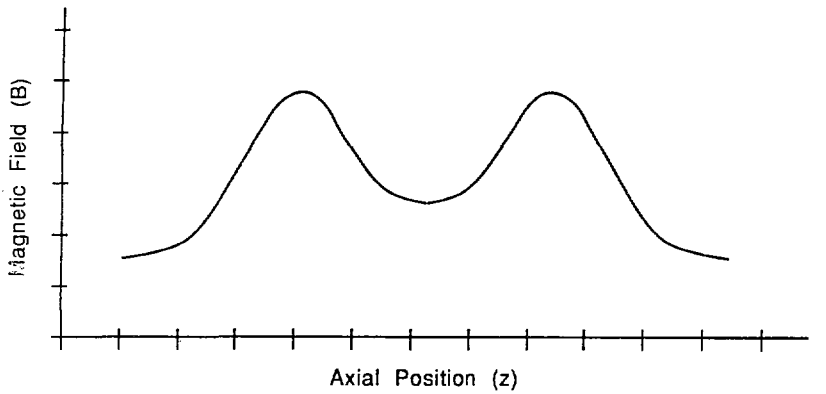

Figure 2.1: Typical Axial Magnetic Field Profile in a Simple Mirror

for fields with spatial scale lengths small compared to the gyroradius. As the magnetic field increases, the perpendicular velocity must increase to maintain the constancy of μ, while the parallel velocity must decrease accordingly to maintain energy conservation. The loss-cone angle (at B_{min}) can be found by first assuming the particle's velocity is all perpendicular at the field maximum, and then use $\mu = constant$, to calculate $v_\perp/v_\parallel$ at the field minimum. This can be written in terms of the velocity components at the field minimum:

$$\mu = \frac{m{v_\perp}^2}{2B_{min}} = \frac{m({v_\perp}^2 + {v_\parallel}^2)}{2B_{max}} = \frac{W_{total}}{B_{max}} \tag{2.9}$$

or,

$$\frac{{v_\perp}^2}{{v_\perp}^2 + {v_\parallel}^2} = \frac{B_{min}}{B_{max}} \tag{2.10}$$

Using the mirror ratio, $R_m = (B_{max}/B_{min})$, and Eq. 2.8, the loss-cone angle can be expressed as:

$$\theta_{loss-cone} = \sin^{-1}\left(\frac{B_{min}}{B_{max}}\right)^{\frac{1}{2}} = \sin^{-1}\left(\frac{1}{R_m{}^{\frac{1}{2}}}\right) \tag{2.11}$$

Particles with pitch angles less than $\theta_{loss-cone}$ are not confined by a simple mirror and can escape out the ends. In the case of a plasma, ions and electrons continually scatter in angle into the loss-cone, and are lost. However, ions at a given temperature scatter much more slowly than electrons at the same temperature and the potential of the plasma increases due to net charge imbalance. The average time for an ion to scatter through 90° is given by Spitzer[5] as(in CGS units):

$$\tau_{ii} = \frac{m^{\frac{1}{2}}(3kT)^{\frac{3}{2}}}{5.712\pi ne^4 Z^4 \ln \Lambda} \tag{2.12}$$

In this equation, m is the ion mass, e is 4.8×10^{-10} e. s. u., Z is the charge, kT is the kinetic temperature in degrees K, n is the ion density in cm^{-3}, and $\ln \Lambda$ is the Coulomb logarithm, which is a measure of average interaction distance in collisions compared to the minimum distance two ions would reach in a head-on collision. This resultant positive potential confines low energy electrons electrostatically, and expels low energy ions. For a simple mirror, the plasma potential continues to rise until the electric field can equilibrate the ion and electron loss rates. Increasing the mirror ratio can improve the ion axial-confinement time, τ_c, by reducing the fraction of solid angle in the loss cone[6], but the dependence is only logarithmic, given approximately by:

$$\tau_c = \tau_{ii} \log_{10}(R_m) \tag{2.13}$$

where τ_{ii} is defined above.

The tandem mirror seeks to utilize the positive potentials generated in two simple mirrors to provide electrostatic axial-confinement for ions contained in a solenoidal region between them. A typical axial magnetic field profile of a tandem mirror is shown in Fig. 2.2. The potential difference, Φ_c, between the solenoidal section, called the *center cell*, and the simple mirrors, called the *end plugs*, is determined by the electron temperature and the ratio of ion densities in the two

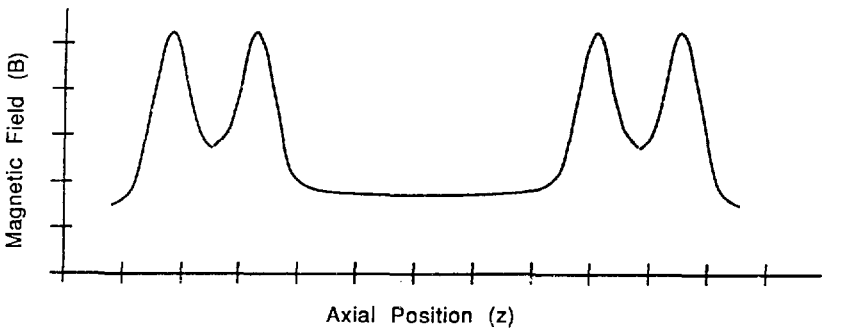

Figure 2.2: Typical Axial Magnetic Field Profile for a Tandem Mirror

regions, as given by the Boltzmann statistics[3]:

$$\Phi_c = T_e \log(\frac{n_p}{n_{cc}}) \tag{2.14}$$

The increase in confinement time as the confining potential increases is greater than exponential, because of the time required to scatter up in energy over the potential.[7] For ions in the central cell, the axial confinement time, τ_c, can be written approximately as:

$$\tau_c = \tau_{ii} \log_{10}(R_m) \frac{\Phi_c}{T_i} \exp(\frac{\Phi_c}{T_i}) \tag{2.15}$$

Appealing as this scaling may be, this approach is not attractive for confining plasmas at thermonuclear temperatures ($\geq$ 10 keV) due to the practical difficulties in generating the high density ratios needed to create confining potentials of 3 to 5 times T_i. One may also increase the confining potential by increasing the electron temperature, but the increased power requirements make this economically unattractive. In 1979, Baldwin and Logan[8] proposed a method for increasing the confining potential without the penalty associated with increasing the electron

temperature in the whole device. They proposed the formation of a region of lower potential between the center cell and the confining potential peak in the end plug. This *thermal barrier* serves to insulate the electron populations of the plugs from the center cell population. Then, the plug electrons can be selectively heated to raise the potential, without the power requirements of heating electrons in the center cell

2.3 The Thermal Barrier

The thermal barrier, while simple in concept, introduces many complications to the tandem mirror. Typical axial profiles of magnetic field, potential, and densities are shown in Fig. 2.3. The potential depression is formed by confining electrons better than ions in the barrier region. In order for the classical loss rate of the electrons to be slower than the ion loss rate, the electron temperature must be high enough to make the electron scattering time longer than the ion scattering time. Equation 2.12 holds for electrons as well (if the electron mass is used) and indicates that the for a given temperature, the electron scattering time is shorter than the ion scattering time by the square root of the ion-electron mass ratio. To create a population with a confinement time longer than the ions in the barrier, these electrons are selectively heated using intense microwaves focused at the electron cyclotron resonance. The ion population, too, must peak in density away from the barrier region, and is prone to various instabilities.[9] However, even if one postulates that a stable configuration can be found, the barrier is a potential well for ions, and collisions can scatter and trap ions there. If there is no mechanism for selectively removing these *trapped ions*, their charge will neutralize the hot, mirror-trapped electrons and the thermal barrier will disappear.

Removal of ions that scatter and are trapped in the barrier's potential well

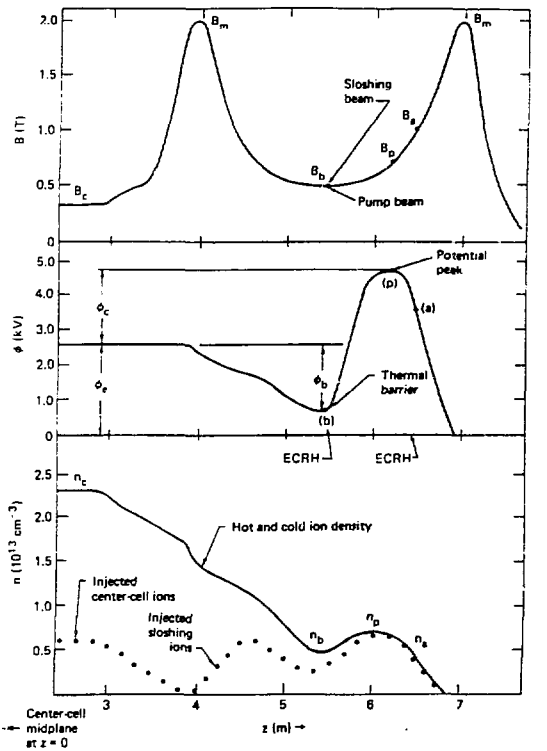

Figure 2.3: Typical Axial Profiles for a Thermal Barrier Tandem Mirror

can be accomplished by several methods. The most straightforward is by charge exchange on an energetic neutral particle beam aimed at the barrier region. Since trapped ions spend more time in the path of the beam, their probability of interaction is greater than ions that only pass through the region. The angle of the beam with respect to the magnetic field can be chosen to be in the loss cone, so the resultant ion leaves the end plug, or the beam can be aimed so the ion is magnetically confined at a pitch angle such that it spends most of its time outside the barrier region. These *sloshing ions* are reflected at a mirror ratio determined by Eq. 2.11 and add to the stability of the device.[10]

Another method for removing trapped ions employs an RF magnetic field tuned to the drift of trapped ions.[11,12] By tuning the frequency of the applied field, the trapped ions can be driven into the loss cone, or walked out radially until they strike a limiter. These techniques, which come under the classification of ***drift pumping***, are not as well understood as the neutral beam pumping, and little experimental experience is available.[13]

In any case, the need for barrier pumping is reduced if the collisional filling rate can be reduced. Raising the temperature of ions passing through the plug from the center cell reduces their scattering rate (see Eq. 2.12). On TMX-U, the center cell ion temperature is raised using Ion Cyclotron Resonance Heating, ICRH. To be effective, the entire plasma cross section must be heated. This dissertation will address the problem of measuring the radial heating profile in TMX-U. The theory and operation of ICRH on TMX-U will be discussed in Chapter 3.

In summary, the thermal barrier is needed in a tandem mirror to ease the plug power requirements. Collisions can scatter and trap ions in the barrier, filling the well, and neutralizing the hot, mirror trapped electrons there. These ions must be removed to keep the potential well from disappearing and destroying the necessary

insulating effect. In order to reduce the pumping requirements, the collisional filling rate is reduced by increasing the center cell ion temperature with ICRH. This must be done uniformly across the plasma cross section. The measurement of radial ion-heating profiles in TMX-U relies on a number of diagnostics, the most important of which is the Radial Energy Analyzer, or REA. The next section discusses the power sources, diagnostics, and resources of the Tandem Mirror Experiment-Upgrade facility, an experiment designed to test the thermal barrier concept.

2.4 Description of TMX-U facility

2.4.1 Overview of TMX-U

Proposed in April of 1980[14], the Tandem Mirror Experiment-Upgrade was an ambitious attempt to bring tandem mirrors into direct competition with toroidal devices, and to provide the necessary experience to guide the operation of the much larger device, the Mirror Fusion Test Facility.[15] Although throughout its operation TMX-U never achieved a thermal barrier configuration at the proposed density of $1 \times 10^{13}\,\mathrm{cm}^{-3}$, much was learned about tandem mirror physics. The technology of high power microwave heating of electrons was advanced, and the formation of thermal barriers at lower densities was demonstrated[16]. Axial confinement times over 100 msec. were measured, but radial losses reduced the overall ion lifetime to less than 10 msec.

TMX-U is a tandem mirror employing quadrupole mirror cells at the ends of a 7 meter central solenoid. The quadrupole fields provide magnetohydrodynamic stability to the plasma.[17] The center cell magnetic field is 0.3 Tesla at the midplane, rising to 2.2 Tesla at the mirror peaks, giving a central-cell mirror ratio of 7.3. The magnetic field at the center of each end cell is 0.5 Tesla, while the outer mirror

peak is 2.0 Tesla, yielding a local mirror ratio of 4.0. The center cell plasma radius is 22 to 25 cm depending on the exact hardware installed. Locations of the plasma fueling and power sources are shown on a diagram of the axial magnetic field profile in Fig. 2.4. On the figure, the label **ECRH** stands for **E**lectron **C**yclotron **R**esonance **H**eating, the microwave heating sources for the electrons. The **10 kG** and **5 kG** systems are 200 kW Gyrotrons, operating at a frequency of 28 GHz. The **18 GHz** systems can deliver up to 20 kW from Klystron sources. The label, **LENI**, stands for **L**ow **E**nergy **N**eutral **I**njection, and indicates the neutral beam injectors that have been modified to operate at either 20 kV or 4 kV injection energy.

By varying the plasma fueling and power sources, TMX-U can operate with or without high axial confining potentials. When operating with long axial confinement times (with thermal barriers), the maximum central-cell density is limited to 1 to $3 \times 10^{12}\text{cm}^{-3}$. However, when operating with smaller confining potentials and greater fueling rates, densities of $6.0 \times 10^{12}\text{cm}^{-3}$ have been achieved. A comparison of the best central-cell confinement parameters for these two modes is shown in Table 2.1[18].

2.4.2 Diagnostics on TMX-U

To measure the many parameters that describe the state of the plasma, TMX-U is outfitted with a multitude of diagnostics. A comprehensive list and schematic location of the diagnostic set is shown in Fig. 2.5. For this investigation of center cell ion heating, however, only a subset of the total diagnostic set is required. These diagnostics measure the plasma density, temperature, and potential, and particle sources and sinks. This subset is shown in Table 2.2. The theory and operational characteristics of each of these will be discussed briefly in the following sections.

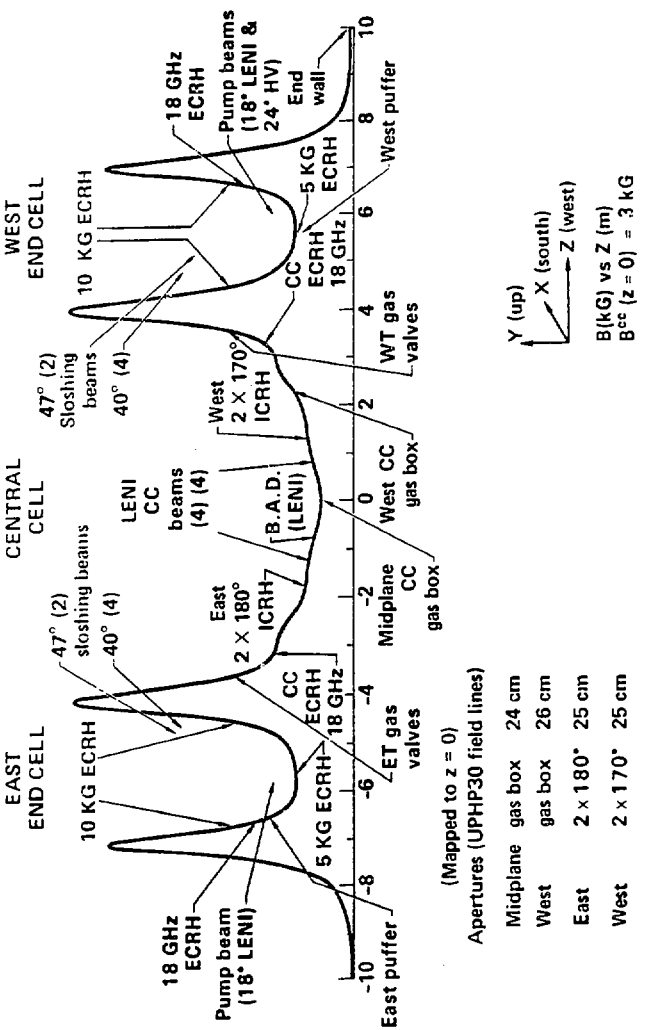

Figure 2.4: TMX-U fueling and heating locations (June 1986)

Parameter	TMX-U high density 6/14/84-6	TMX-U thermal barrier 1/22/85-15	TMX-U design
Density, $\hat{n}_e(10^{12}cm^{-3})$	6	1.2	23
Ion energy			
$E_\perp(keV)$	2.0	1.5	2.9
$E_\parallel(keV)$	0.4	0.1-0.2	0.9
Electron temperature, $T_{ec}(keV)$	0.16	-	0.35
Axial particle lifetime, $\tau_{p\parallel}(ms)$	6	100	43
Radial nonambipolar lifetime without potential control plates $\tau_{p\perp}(ms)$	14	5	22
Global energy confinement time,$\tau_E^g(ms)$	3.5	5	4
$\hat{n}\tau_E^g(10^{10}cm^{-3}s)$	2.1	0.6	9.2

Table 2.1: TMX-U central cell confinement parameters.

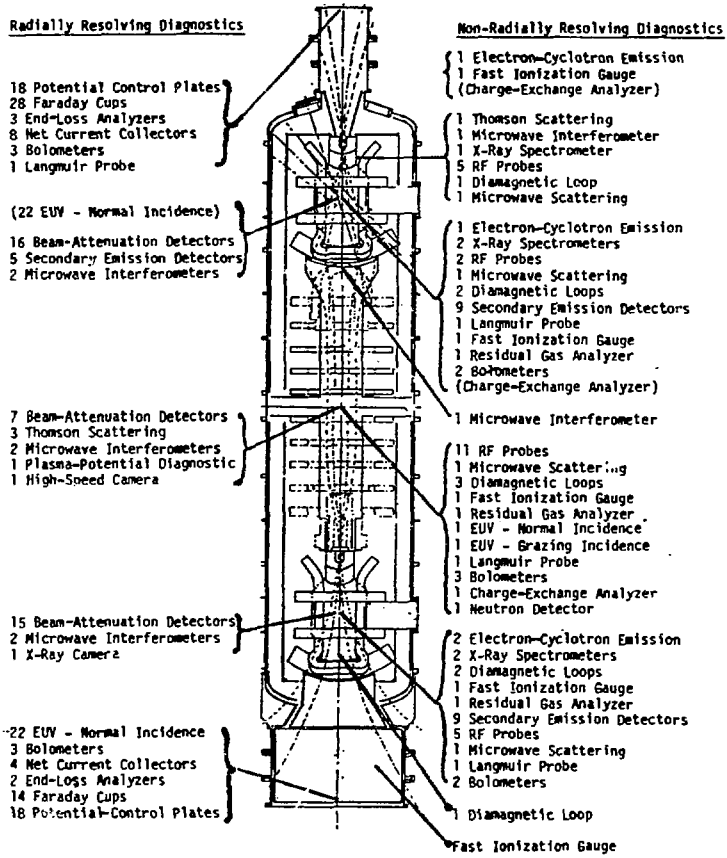

Figure 2.5: The TMX-U diagnostic set and approximate location of each diagnostic on the machine.

Diagnostic Name	Plasma Parameter	Location
H_α Camera	Ionization source	Central Cell
Microwave Interferometry	Line density	9 axial locations
Faraday Cup Array	Ion end-loss current	East & West end wall
Potential Control Plates	Net end-loss current	East & West end wall
Thallium Beam Probe	Plasma potential	Central Cell
Diamagnetic Loop	Stored energy	Central & End Cells
Thompson Scattering	Electron Temperature	Central & End Cells
Langmuir Probe	Electron Temperature	Central Cell
End-Loss Ion Spectrometer	End-loss ion temperature	East & West end wall
Time-of-Flight	Passing-ion Temperature	East Plug
Radial Energy Analyzer	Ion temperature, density, and, potential	Central Cell

Table 2.2: List of Diagnostics Used to Evaluate Power Balance and/or REA performance

These diagnostics measure parameters needed to validate the REA measurements and to evaluate the power loss mechanisms in the central cell of TMX-U. For each radial shell, the difference in power required to sustain the central-Cell plasma conditions with and without ICRH is set equal to the power absorbed from the RF antennas. A radial integral of the calculated absorbed power can be compared to the total broadcast power given by the RF power diagnostics. This provides a check on the radial profile given by the power balance. The radial profile of ICRH can then be compared to modeling code predictions.

2.4.3 Description of the H_α Imaging System

The H_α imaging system records light emitted from the interaction of fueling gas and the plasma. The central-cell plasma of TMX-U is fueled by cold gas fed to a baffled enclosure known as a *gas box*. The gas box is basically a hollow ring that surrounds the plasma column, that has a nearly continuous circumferential slit facing the plasma. The central-cell gas box can be seen in the photograph in Fig. 4.3. Gas is released into the hollow interior of the gas box by pulsed, piezoelectric valves. The gas then escapes out the slits, penetrates the plasma column, and is ionized by the plasma. Close fitting baffles are placed on either side of the gas box in order to reduce the axial flow of the released gas. This restricts the fueling gas to the small region between the baffles.

Unfortunately, the situation is not this simple. There are several processes competing with the ionization of the gas in the plasma. When a gas molecule (D_2) enters the plasma, it can just be broken into two free atoms. Because of the molecular binding energy, these two free neutrals have an energy of about 2 eV, and travel in opposite directions (to conserve momentum). On average, one atom travels toward the plasma, and one toward the wall. The one hitting the wall

can stick there, or give up its energy and come off as another cold neutral. The other atom can undergo a charge exchange event. This is where the cold neutral exchanges its electron with a hot ion in the plasma, creating a cold ion, and a hot neutral, which then leaves the plasma. This maintains the ion density, but represents a loss of energy. As an atom (or molecule) undergoes collisions in the plasma, its electron(s) can be knocked into higher energy states, but not freed. The electron then may return to a lower energy state via photon emission. A common transition is from the second excited state to the first excited state, yielding a photon of wavelength 6562.8Å [19]. This line in the emission spectrum is known as the Balmer-α line. It is this light that is used to infer the ionization rate in the gas box region. Although to be strictly correct, this should be abbreviated D_α, the difference in wavelength from H_α is so slight that H_α filters are used, and the diagnostic is commonly called the H_α system.

Above a plasma electron temperature of about 22 eV, the ratio of probabilities of ionization to photon emission is nearly constant, even though each is varying significantly.[20] So, by accurately measuring the light emitted by the plasma, the ionization rate can be derived.

An absolutely-calibrated, high-speed video camera is mounted on the end-wall of TMX-U and is focussed, through a quartz window, on the gas-box region in the central cell. The camera is fitted with a 6562.8Å bandpass filter, and can record a two-dimensional picture every 0.5 millisecond onto magnetic tape. The recorded images are digitized, integrated and processed by an HP9836 desktop computer to yield the ionization source as a function of plasma radius. Figure 2.6 shows a computer-reconstructed image of the plasma D_α light, with and without ICRH. These images clearly show the change from nearly uniform ionization, to ionization peaking at the plasma edge, with the use of ICRH. The ionization source term,

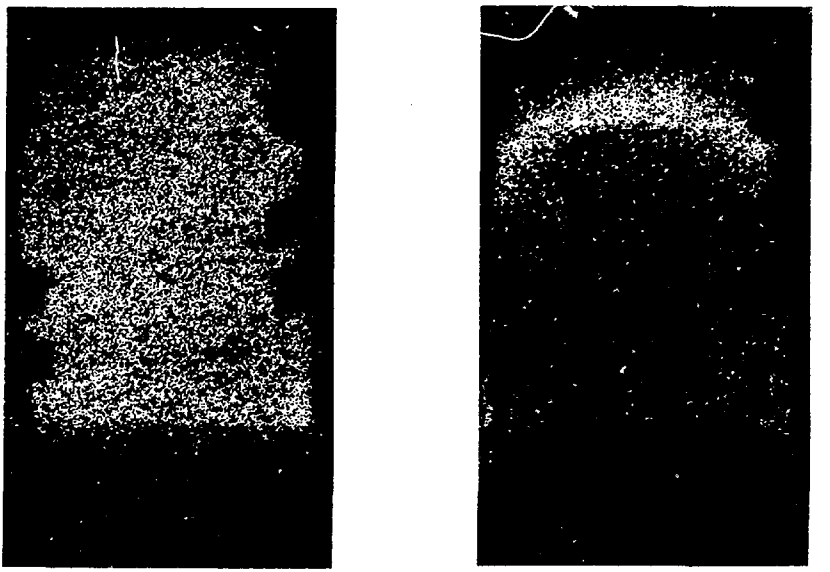

Figure 2.6: Computer-reconstructed image of D_α light from the gas-box region in the central cell of TMX-U. Light areas indicate areas of D_α emission. The dark areas on the sides and bottom are where the magnet cases and support structures in the end cell block the line-of-sight to the central-cell. The image on the right is with ICRH, the left image is without.

and its associated energy loss, as a function of radius, is used in the power balance in Chapter 8.

2.4.4 Microwave Interferometry

The plasma density in TMX-U is measured using the technique of interferometry. This method relies on the fact that the plasma dielectric constant varies with density. The output from a microwave source is split into two beams. One microwave beam passes through the plasma column, and the other beam does not. As the density builds, the dielectric constant of the plasma increases, and the wavelength of the beam going through the plasma shortens. After going through the plasma, the two beams are mixed, and fed into a phase comparator. The phase shift between the two beams is an indication of the line-integrated plasma density the beam traversed. The line-integrated density from this diagnostic is used to calibrate the density measured by the REA, and to group similar plasma discharges for data analysis.

2.4.5 Faraday Cup Array

An important loss channel of both energy and particles is the current of ions that leave the device axially. On each end wall of TMX-U, there are arrays of detectors to measure this ion current. Each *Faraday Cup* consists of a biased aperture in front of an ion collecting can. The aperture plate is held at a -3000 volt potential to prevent electrons from entering the can. The ion current gathered by the cup is measured and recorded as a function of time and position on the end wall. The current is mapped back to the central cell using the ratio of magnetic fields, and is processed to give the end-loss ion current as a function of radius. Due to the limited number of cups, the current is calculated only as radial integrals, at

several discrete radii.

2.4.6 Potential Control Plates

One of the difficulties associated with quadrupole magnetic fields is that they can produce radial diffusion of the plasma. As the plasma potential builds, the radial electric field gives rise to an $\vec{E} \times \vec{B}$ rotation of the plasma column. The quadrupole fields on each end of the device are rotated 90° with respect to one another so the curvature-$\vec{B}$ drifts on each end cancel as the particles bounce back and forth. The rotation of the plasma, if comparable to the bounce time, spoils this cancellation and the plasma can quickly drift out radially. Since the rotational speed is directly proportional to the radial electric field, reducing the plasma potential with respect to the chamber walls can reduce radial losses.

The *Plasma Potential Control Plates*, or PPC plates are an attempt to lower the potential in the device with respect to ground, thereby reducing the radial electric field in the central cell. The theory is conceptually simple. Electrons are lost axially faster than ions, until the resultant positive potential retains them. If the end walls are insulated, their potential can drop, rather than the plasma potential rising. Eight concentric aluminum rings are placed on each end wall and insulated from ground and each other. The rings are elliptical in shape and map to circles in the central cell. Also, they have insulating breaks every 90° azimuthally to prevent currents from flowing around each ring.

For this series of experiments, however, the plates were grounded through a 0.1 ohm resistor, and the net current from each plate to ground was measured. The plates collect both ions and electrons, so the current measured is the net difference between the two. Since charge is conserved globally, net current to the plates indicates preferential radial transport of either ions or electrons. This is

called *non-ambipolar radial transport*. The PPC plate current is thus used to indicate the radial losses as a function of radius.

2.4.7 Diamagnetic Loop

Stored plasma energy is measured on TMX-U with Diamagnetic Loops (DML). An ion in its gyro-orbit can be thought of as a small current loop, directed such that the magnetic field generated by that loop opposes the applied field. The same is true for electrons. The greater the particle's energy, the greater the magnitude of the opposing field. This behavior is known as *diamagnetism*, and is used to measure the stored energy in the plasma column. A loop of wire is placed around the plasma and inside the conducting wall of the vacuum chamber. As the plasma builds in density and temperature, magnetic flux is pushed out of the plasma and into the surrounding space between the plasma and the conducting wall. The change in flux within the loop generates a voltage around the loop in direct proportion to the change. This voltage is given by Faraday's Law:

$$V = -\frac{d\Phi}{dt} \tag{2.16}$$

where $\Phi = \int_s \vec{B} \cdot d\vec{A}$ and $d\vec{A}$ is the normal area element and the integral is taken over the interior of the loop. This voltage is integrated in time to give the flux excluded by the plasma. By knowing the areas of the loop and the flux conserving wall around it, the change in flux can be related to the energy stored in the plasma. This stored energy is just the radial integral of the ion and electron temperatures times the density. This is used as a cross check on the temperature and density profiles measured by the REA.

2.4.8 Thompson Scattering

The electron temperature in the central cell of TMX-U is measured using the Doppler shift of scattered laser light. A beam of light from a ruby laser is passed through the plasma and scatters off the electrons and into a grating spectrometer. The spread in wavelength indicates the spread in electron velocities and is indicative of the electron temperature. The laser is pulsed only once during a plasma shot and the optics are set up to look at only two radii in the central cell. The electron temperature is needed to calculate the power transferred between the ions and electrons.

2.4.9 Langmuir Probe

Named after I. Langmuir[21], this probe consists of a small metal tip inserted into the plasma and swept in voltage. The current measured as a function of tip voltage can indicate several important plasma parameters. An idealized characteristic is depicted in Figure 2.7.[22] The maximum current drawn at large positive voltages, the *electron saturation current*, is proportional to the density times the square root of the electron temperature. The slope of the curve as the voltage is reduced indicates the electron temperature directly. The point at which the probe draws no current is the *floating potential*. Conceivably the ion temperature and density can be determined by the current characteristics at negative voltages, but most often the ion saturation current is governed by the ion sound speed, which is set by the electron temperature. In TMX-U, the Langmuir probe is used only at the plasma edge, and provides a measurement of the electron temperature there.

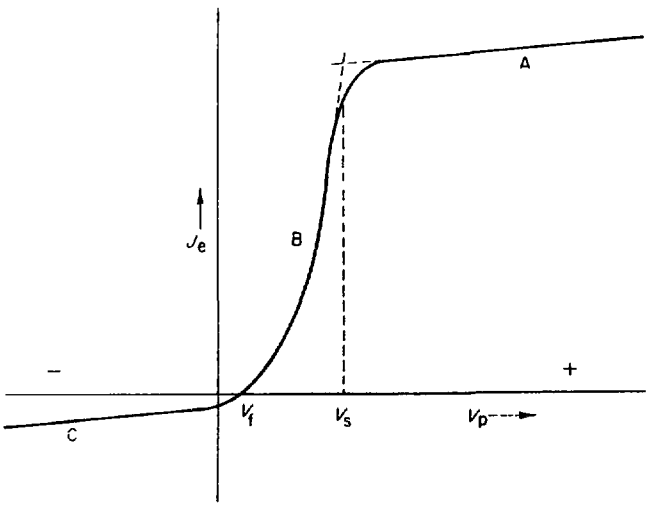

Figure 2.7: Typical Langmuir probe characteristic.[22] The ratio of ion-to-electron mass has been made artificially smaller to show the detail in the ion collection region.

2.4.10 Thallium Beam Probe or Plasma Potential Diagnostic

The measurement of the plasma potential in the central cell is important in the understanding of the operation of TMX-U. In addition to the radial transport issue discussed above, ions that escape radially carry energy out with them and constitute an important loss channel. The plasma potential in the central cell is measured on TMX-U directly using a Thallium Beam Probe, also referred to as the Plasma Potential Diagnostic, or PPD.[23]

The probe consists of a high energy Tl^+ beam injected perpendicular to the central-cell magnetic field. The high mass and 80kV energy give the ions a gyroradius roughly the size of the TMX-U vacuum vessel. As the primary Tl^+ beam traverses the plasma, some of the ions are further ionized to the Tl^{++} state. These secondaries then have a radius of curvature half that of the primaries. By careful alignment, these secondaries enter an electrostatic energy analyzer and their energy measured. The energy of these ions is equal to the primary beam energy, plus the potential at which they were ionized to the +2 state. Only ions from a small region of space have the correct trajectory to reach the energy analyzer, so the potential measurement is essentially a point measurement.

One of the difficulties with the PPD is that the energy analyzer assumes the ion beam is uniform over its cross section. The ion beam is deflected onto a split-plate detector, with the difference in current between the two plates used to infer the position of the beam on the plates. The beam energy is calculated from the position on the plates, and the deflecting voltage on the analyzer. Current density variations across the beam can make it appear the beam center has shifted, with a corresponding energy shift of the beam. This, in turn, shows up as a shift in the plasma potential. Due to this, relative changes in potential are believed accurate,

but the absolute calibration of the potential is questionable. The potential measured by the PPD was compared to the potential measured by the ELIS and the REA and an offset correction applied to the PPD data. This probe was used only to cross-check potential measurements made by the REA and ELIS.

2.4.11 End-Loss Ion Spectrometer

The ions that escape out the ends of a tandem mirror carry with them a substantial amount of energy. In addition to the ion temperature, the plasma potential accelerates the ions, giving them even more energy. The End-Loss Ion Spectrometer, or ELIS, measures the energy distribution of the ions escaping each end of TMX-U. Since the magnetic field strength at the entrance to the ELIS is only 130 gauss versus 22 kG at the mirror peak, conservation of magnetic moment forces all ions to travel nearly parallel (within 4.4°) to the magnetic field at the end wall. Since the ELIS is designed with a 4 degree acceptance angle, nearly all ions escaping to the end wall can enter the ELIS for analysis. The ELIS employs an electric field parallel to a magnetic field, $\vec{E} \parallel \vec{B}$, to separate the end-loss ions by charge-to-mass ratio and velocity.[24,25] Upon entering the ELIS, an ion follows 180° of a helical trajectory, its radius determined according to Eqn. 2.3. As it traverses between the magnetic pole pieces, the electric field accelerates the ions. Since the transit time through the magnetic field is determined by charge and mass alone, all ions with a given charge-to-mass ratio have the same transit time, and therefore are displaced the same distance by the electric field, while ions with a different charge-to-mass ratio are displaced a different distance. The ions are collected on a segmented plate, with the current to each segment recorded as a function of time. A schematic of the geometry is shown in Figure 2.8. The detector plane is broken into 128 segments, arranged in two rows of 62, with the remaining 4 surrounding

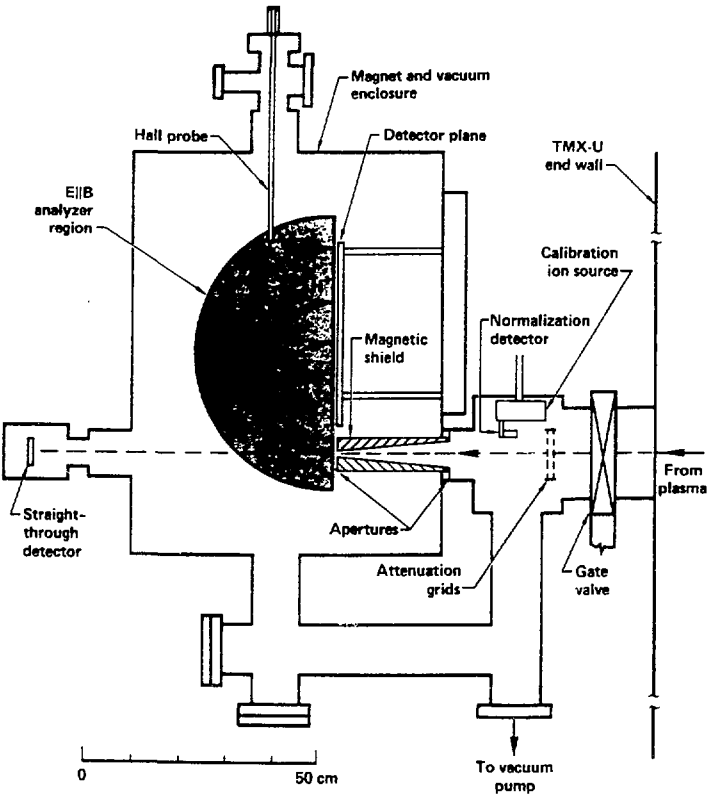

Figure 2.8: Schematic of ELIS geometry.

the rest. These 4 help in adjusting the fields so that the ion trajectories hit the detector arrays.

The current from each segment is recorded by a LeCroy 8212 Data Logger at a 5 kHz rate. The data from these recorders (located within the TMX-U pit) are transferred via a fiber-optic link to an HP9836c desktop computer for analysis. The data are fit to a shifted Maxwellian distribution. The slope on the high energy side gives the ion temperature and the low energy intercept indicates the plasma potential. Figure 2.9 shows a sample energy spectrum from the ELIS as a function of time. Since the ELIS is located near the axis of the machine, and is not designed to be moved, the measurements made by the ELIS are only used to calibrate the REA at this one radial location, and to provide a check on the constancy of plasma discharges.

2.4.12 Time-of-Flight

The Time-of-Flight (TOF) spectrometer measures the velocity distribution of neutral particles that charge-exchange in the East plug of TMX-U.[26] The TOF is used to infer the temperature of ions passing through the plug from the central-cell. These ions charge-exchange off the Neutral Beams in the plug and enter the TOF. The TOF analyzer consists of a chopper wheel near the plasma, a long drift tube, and a detector at the far end. The chopper wheel opens a small slit briefly, and allows a small pulse of neutrals to enter the drift tube. As the neutrals traverse the tube, the pulse spreads in space, the faster neutrals arriving at the detector before the slower. The number of neutrals arriving as a function of time after the slit opened gives the velocity distribution of the incident charge-exchange flux. The flight tube is aimed at the midplane of the East plug, at an angle of 22.5° to the magnetic axis, which is within the magnetic loss-cone.

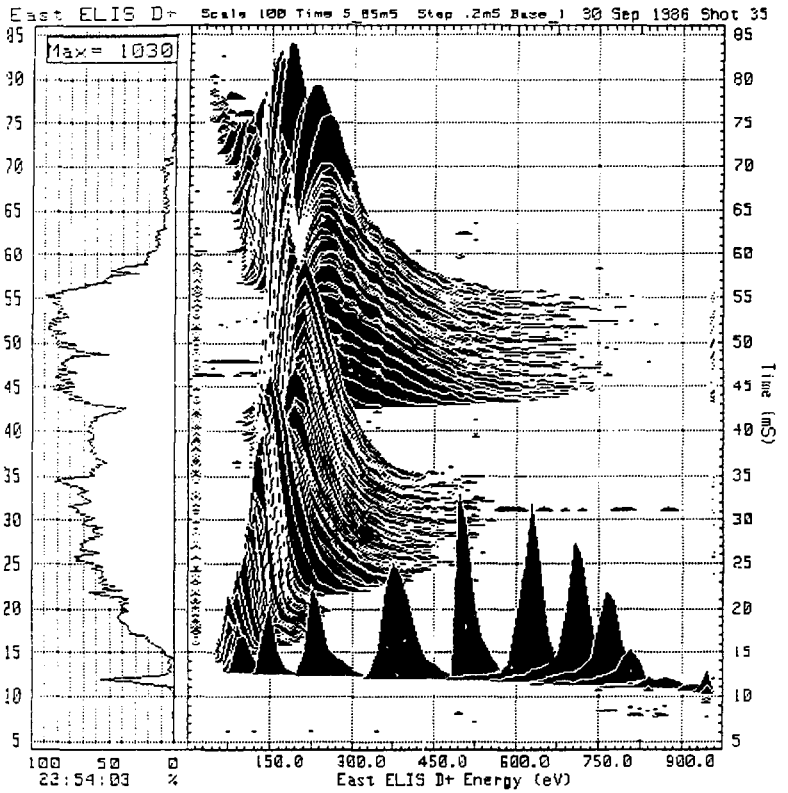

Figure 2.9: Typical ion energy spectrum from the ELIS. In the plot, time runs from bottom to top. Each spectrum plotted shows current vs. energy (channel). The plot on the left shows the sum of the current to all channels, as a function of time. The longer tail on the energy spectrum from 21-34 msec. and 42-55 msec. shows the heating due to ICRH.

2.4.13 Radial Energy Analyzer

The development, implementation, and operation of the REA on TMX-U was the responsibility of the author. Although the probe head and some electronics were obtained from TRW, much work was required to create an operational diagnostic.

The calculation of power balance as a function of radius requires the knowledge of the ion temperature, density, and plasma potential as a function of radius in the central cell. Although in theory, the PPD can give the potential profile, its absolute calibration is suspect (see Section 2.4.10). Also, the PPD is limited to densities over $1.0 \times 10^{11} cm^{-3}$ due to signal-to-noise considerations. The radial dependence of ion temperature, however, can only be measured by the REA. The measurements taken by the REA are, in fact, essential to the calculation of the radial profile of ICRH, which is the goal of this dissertation. The details of the REA construction, operation, and data analysis will be discussed in depth in Chapter 4.

Chapter 3

Description of ICRH System

Ion cyclotron resonance heating, ICRH, has been used on many magnetic confinement experiments[27,28,29,30,31,32,33,34,35], with varied results. This technique is used to add energy to the ions by creating a electric field rotating at a frequency near the cyclotron frequency in the plasma. The magnitude of the center-cell magnetic field in TMX-U places the resonant frequency in the 2-5 MHz range. In this range of frequencies, the wavelength is too long to be transmitted and launched by hollow waveguide structures of practical size, so coaxial waveguides and antennas are used. On TMX-U, there are two separate systems, each consisting of a transmitter, coaxial transmission line, impedance-matching network, and antenna. The following sections discuss the theory and design of these two systems, and the two codes used to model ICRH on TMX-U.

3.1 ICRH Theory

3.1.1 Basic Principle of ICRH

The goal of ICRH is to transfer the energy from an RF electric field to ions in the plasma. Ions gain energy from an electric field when they move along the direction of the field. The change in energy, ΔW, is equal to:

$$\Delta W = \int_b^a q\vec{E} \cdot d\vec{l} \tag{3.1}$$

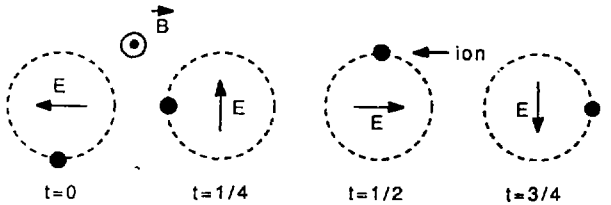

Figure 3.1: A rotating electric field accelerates ions in a magnetic field. The ion position in its gyro-orbit and the direction of the RF electric field is shown every quarter of a gyro-period.

where $d\vec{l}$ is along the path of the ion from points 'a' to 'b'. For an ion in a magnetic field, the gyro-motion returns the ion to the same radius every gyro-orbit. Therefore, a constant, uniform electric field perpendicular to the magnetic field, provides no net energy gain. Static electric fields aligned with the magnetic field can accelerate ions, but it also accelerates electrons, which is not the desired objective. Electrons have greater mobility along the field, due to their small mass, and can absorb the parallel field energy much faster than the ions. However, if the electric field vector can be made to rotate at the same frequency as the gyrofrequency of an ion in the magnetic field, and in the same direction, an ion can be continuously accelerated. In the frame of the ion, the electric field is constant over the orbit. In the notation of optics, this is a left-hand circularly-polarized field. This effect is shown schematically in Fig. 3.1. This field can be produced by a plasma wave, and the absorption of its energy in this manner is called *cyclotron*

damping. Equation 3.1 still holds, although now the electric field is the RF electric field.

The key problem to address in ICRH is the creation of waves in the plasma with the proper characteristics. In order to heat the entire plasma cross section, the magnitude of the electric field should be uniform in radius. To optimize ion heating, the parallel electric field component should be small, and the phase velocity of the wave much different than the electron thermal velocity. This is to minimize electron heating via Landau damping of the wave.[36] The electric field should have a large left-hand circularly-polarized component, to efficiently couple to the ion motion. The production of waves in a plasma with these attributes is discussed in the following sections.

3.1.2 Analytic Theory of Waves in a Magnetized Plasma

The basic theory of wave propagation in a cold, magnetized plasma is set forth in the book by T. H. Stix,[37] *The Theory of Plasma Waves*. This section uses standard notation described therein. The wave propagation is modified by finite ion and electron temperature, but the behavior is qualitatively the same. The plasma response to an applied electromagnetic field can be described by a complex dielectric tensor. The finite temperature effects are contained within the elements of the tensor, $\overleftrightarrow{\epsilon}$, defined by:

$$\overleftrightarrow{\epsilon} = \begin{bmatrix} S & -iD & 0 \\ iD & S & 0 \\ 0 & 0 & P \end{bmatrix} \tag{3.2}$$

$$R = 1 + \sum_{\alpha} \frac{{\omega_{p\alpha}}^2}{\omega k_z v_\alpha} Z\left[\frac{\omega + i\nu_\alpha + \omega_{c\alpha}}{k_z v_\alpha}\right] \tag{3.3}$$

$$L = 1 + \sum_{\alpha} \frac{{\omega_{p\alpha}}^2}{\omega k_z v_\alpha} Z\left[\frac{\omega + i\nu_\alpha - \omega_{c\alpha}}{k_z v_\alpha}\right] \tag{3.4}$$

$$S = \frac{1}{2}(R + L) \tag{3.5}$$

$$D = \frac{1}{2}(R - L) \tag{3.6}$$

$$P = 1 - \sum_{\alpha} \left(\frac{\omega_{p\alpha}}{k_z v_\alpha}\right)^2 \frac{Z'\left(\frac{\omega + i\nu_\alpha}{k_z v_\alpha}\right)}{\left[1 + \frac{i\nu_\alpha}{k_z v_\alpha} Z\left(\frac{\omega + i\nu_\alpha}{k_z v_\alpha}\right)\right]} \tag{3.7}$$

where:

$\omega_{c\alpha}$	=	cyclotron frequency of species α
$\omega_{p\alpha}$	=	plasma frequency of species α
ω	=	wave frequency
k_z	=	parallel wave number
v_α	=	thermal velocity of species α
Z	=	plasma dispersion function
ν_α	=	collision frequency of species α

This tensor models collisionless cyclotron and Landau damping of the waves by the plasma. Collisions are modeled in the above definition by a particle conserving Krook[38] model, where the ν_α's are the respective collision times. The dielectric tensor ignores finite gyroradius effects. The form of the tensor for the cold plasma approximation is the same as the above definitions, with the appropriate limits taken on the terms R, L, and P, as the ν_α 's and v 's $\rightarrow 0$. The expressions for a cold plasma then become:

$$R = 1 - \sum_{\alpha} \frac{{\omega_{p\alpha}}^2}{\omega^2} \left(\frac{\omega}{\omega - \omega_{c\alpha}}\right) \tag{3.8}$$

$$L = 1 - \sum_{\alpha} \frac{{\omega_{p\alpha}}^2}{\omega^2} \left(\frac{\omega}{\omega - \omega_{c\alpha}} \right) \tag{3.9}$$

$$P = 1 - \sum_{\alpha} \left(\frac{\omega_{p\alpha}}{\omega} \right)^2 \tag{3.10}$$

For systems with periodicity, Maxwell's equation are combined and Fourier analyzed in time and spatial coordinates to give the equation:

$$\vec{k} \times (\vec{k} \times \vec{E}) + \frac{\omega^2}{c^2} (\overleftrightarrow{\epsilon} \cdot \vec{E}) = 0 \tag{3.11}$$

Zeros of the determinant of this equation lead to the normal modes of the plasma. For systems without symmetry, the full set of Maxwell's equations must be solved.

3.1.3 RF Modes

The dispersion relation for the plasma can be written in terms of the wave number, n ($\equiv kc/\omega$), the angle of wave propagation with respect to the applied magnetic field, θ, and previously defined elements as:[37]

$$\tan^2 \theta = \frac{-P(n^2 - R)(n^2 - L)}{(Sn^2 - RL)(n^2 - P)} \tag{3.12}$$

For propagation along $\vec{B}$ ($\theta = 0$), the three normal modes occur when $n^2 = R$, $n^2 = L$, and $P = 0$. Of the three, the mode with $n^2 = L$ is left-hand circularly polarized as required to interact with the ion gyro-motion, and propagates at frequencies up to the ion-cyclotron frequency. Although the above is strictly true only in the cold-plasma limit, and for propagation along $\vec{B}$, the mode is still predominantly left-hand polarized for warm plasmas and propagation angles near zero. This mode is known as the Alfvén[39], hydromagnetic, ion-cyclotron or simply *slow* ave. It

is often given this last name because its phase velocity is less than that of the magnetosonic wave (also called the *fast* wave), which is the solution of $n^2 = R$, for $\theta = 0$.

The solution for the wave fields in cylindrical coordinates, as is appropriate for coaxial plasma filled wave guides, takes the form of Bessel functions. The expressions given by Appert[40] et al. show that the magnitude of the left-hand circularly polarized component is proportional to $J_{m+1}(k_r r)$, where m is the azimuthal mode number. Only the $m = -1$ mode (proportional to J_0) is non-zero on axis.

Therefore, it is the $m = -1$ slow wave that has the desired properties. It can propagate along the magnetic field from the antenna location to the absorption region, it is predominantly left-hand circularly polarized, and peaks on-axis. The ICRH system was designed to excite this mode.

3.2 RF Modeling Codes

Two codes, ANTENA[42] and GARFIELD[43], have been used to model the antenna-plasma coupling on TMX-U. Each has its advantages and limitations, with GARFIELD still under development at this time. ANTENA was used to design the present TMX-U antenna systems, and has predicted the plasma loading on the antenna quite accurately.[35,44]

3.2.1 Description of the ANTENA code

In theory, the antenna-plasma coupling could be calculated by hand, but to allow a wide range of parameters to be investigated, a computer code is needed to solve Eq. 3.11. The code, ANTENA, written by B. D. McVey, was the first code generally available to model a straight, cylindrical plasma column surrounded by a conducting shell. Approximating the plasma geometry as an infinite, uniform

plasma cylinder, surrounded by a vacuum annulus and a perfectly conducting, cylindrical wall, standard boundary conditions will provide enough constraints to solve for the modes. In its first version[41], the code could only model a uniform plasma, and a single antenna. McVey has subsequently expanded the code[42] to include a multi-layered radial structure of temperature and density, as well as allowing for multiple antennas. The essence of the code has remained unchanged, however, it has only increased in complexity.

Axial and azimuthal uniformity allow Fourier transforms to be taken in these two dimensions. The currents in the antenna are modeled as a current sheet at the antenna radius, Fourier decomposed into a sum of axial and azimuthal modes. The code uses the general solution to Eqn. 3.11, and solves for the ten arbitrary constants of each mode by imposing boundary conditions at the plasma surface, the current sheet, and the vacuum wall. At the plasma surface, the tangential components of both electric and magnetic fields are continuous. At the outer conducting wall, tangential electric fields are zero. And, at the current sheet, the tangential electric field is continuous, while the tangential magnetic field is discontinuous by an amount given by Ampere's law (in vacuum):

$$\vec{K} = (\vec{B}_1 - \vec{B}_2) \times \hat{a} \tag{3.13}$$

where $\vec{K}$ is the surface current density, and $\hat{a}$ is a unit vector normal to the surface. The electric and magnetic field components of each mode are then summed to give the real-space field values. Power absorbed by the plasma is also calculated by summing $\frac{1}{2} Re(\vec{J} \cdot \vec{E})$ over all modes. This ignores cross-mode contributions to the power, but provides an approximate value of absorbed power. Plasma loading is calculated for each mode and summed.

The code, ANTENA, models the major features of the TMX-U system, but cannot describe the effects due to the axial variation of magnetic field, and the

cyclotron resonance on the wave propagation.

3.2.2 Description of GARFIELD code

The limitations of the ANTENA code prompted M. A. Phillips to write a code to describe wave propagation in plasmas in axially varying magnetic fields. This code, the Grumman Aerospace Radiofrequency field, or GARFIELD[43] code, doesn't rely on axial or radial uniformity and as such, cannot Fourier transform these spatial coordinates. The system, however, is assumed to have rotational symmetry and Maxwell's equations are transformed accordingly. The code treats the antenna currents explicitly, yielding an equation similar to Eq. 3.11:

$$\nabla \times (\nabla \times \vec{E}) - \frac{\omega^2}{c^2}(\overleftrightarrow{\epsilon} \cdot \vec{E}) = i\omega\mu_o \vec{J}_{ext} \tag{3.14}$$

where the dielectric tensor, $\overleftrightarrow{\epsilon}$, is for a cold plasma, with a small collision term added to simulate absorption and to aid in numerical stability. The code solves the equations in flux coordinates numerically, using a finite-difference method. The field quantities are then transformed to cylindrical coordinates for display.

3.2.3 Need for Experimental Verification

Although the global agreement between ANTENA and experiment is good, the fine structure is unmeasured. In order for the thermal barrier concept to work, the plasma cross section must be heated nearly uniformly. To measure the radial profile of power deposition, a means of determining the ion temperature, density, and potential as a function of radius is needed. Although more elaborate and costly means are possible, a small probe was employed, the REA. The implementation and operation of the REA was the responsibility of the author, and forms the basis of this dissertation.

3.3 Design of RF Hardware

3.3.1 Theoretical Design Issues

As stated before, the goal of ICRH on TMX-U was to increase the ion temperature in the center cell. The power requirements and operating scenarios for the start-up of TMX-U were developed by Molvik and Falabella.[45] Drawing on the experience of past experiments (such as the Model C-Stellerator[28], and more recently, TMX[29]), and considerations expressed in Section 3.1.3, heating via the *slow wave* was chosen. The wave is launched from an antenna placed at a higher magnetic field than the center cell midplane, at a frequency below the local cyclotron frequency. The wave propagates toward the midplane where the magnetic field strength is lower, and damps strongly as its frequency matches the cyclotron frequency. This effect is called a *magnetic beach*, an analogy to ocean waves breaking on a beach. Although the physical mechanism is different, the result is the same, the waves give up their energy to the particles (ions or sand) at the beach. This technique of heating at a magnetic beach allows the waves to penetrate and heat the plasma cross section more uniformly. If the antenna is operated at the local cyclotron frequency, the dielectric constant effectively excludes the RF electric field from the core, and the damping is so strong, the majority of the broadcast power is absorbed at the plasma edge.

At the time the ICRH system was proposed for TMX-U, the only code available to model the antenna-plasma coupling was ANTENA. As discussed in Section 3.2.1 above, the code models an infinite, axially uniform plasma cylinder, and as such, cannot correctly model both the cyclotron resonance and the conditions at the location of the antenna. However, we have found[35] that ANTENA correctly predicts the plasma loading resistance seen by the ICRH antenna in TMX-U. The plasma

loading resistance is defined as the ratio of power absorbed by the plasma to the current in the antenna squared. High loading resistances allow more power to be delivered to the plasma before limits on antenna current and voltage are reached, and reduces the fraction of power lost in ohmic heating of the antenna structure. Shown in Fig. 3.2 is a plot of the measured and predicted loading resistances as a function of the frequency, normalized to the cyclotron frequency at the antenna location. This supports the hypothesis that the coupling to the plasma is predominantly governed by the local conditions at the antenna. The waves excited under the antenna then propagate to the resonance where they are strongly damped. The efficiency of the antenna system, ϵ, is defined to be:

$$\epsilon = \frac{\mathcal{R}_{plasma}}{\mathcal{R}_{plasma} + \mathcal{R}_{antenna}} \tag{3.15}$$

where the $\mathcal{R}$'s are the respective resistances. Therefore, optimizing the coupling increases the overall efficiency of the ICRH system. The code was run to find the optimum operating frequency under various plasma conditions.[46] Based on these code results, the ICRH systems are operated at 85% of the local cyclotron frequency when the central-cell density is near $1 \times 10^{12}\text{cm}^{-3}$. As shown in Fig. 3.2, the experimentally measured loading also peaks at $0.85\omega_{ci}$. The plasma loading resistance is calculated from the change in reflection coefficient on the transmission line with and without plasma present. This is performed by an HP9836 desktop computer and associated hardware, described in the following sections.

3.3.2 Description of RF Hardware

The actual hardware used in the ICRH system has evolved over a period of years to its current configuration. The antenna structures have changed several times, each change constrained by compatability with the remaining components. The two systems in use on TMX-U are similar, but not exactly identical. The RF

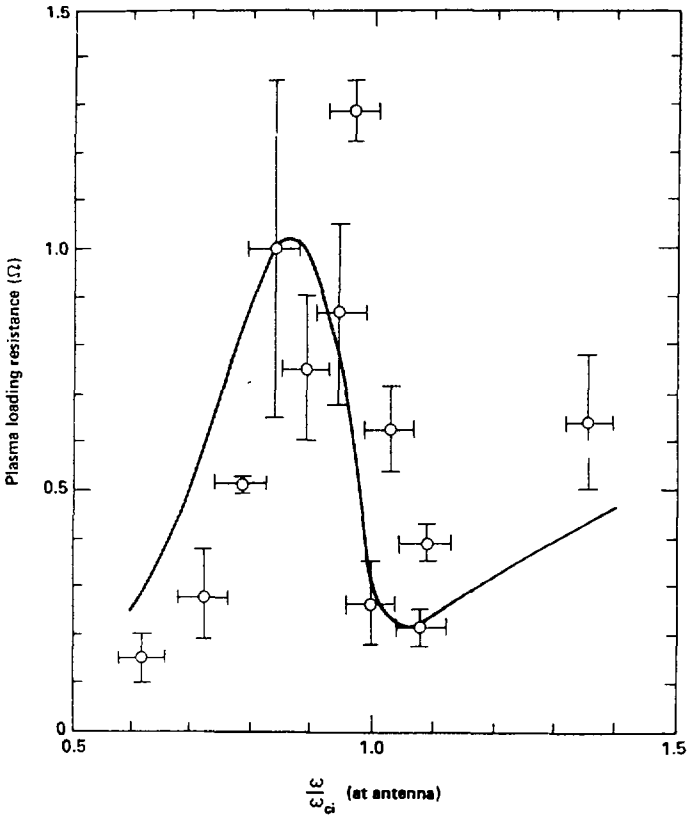

Figure 3.2: *Plot of antenna loading resistance vs. frequency*[35] *for the West antenna at a density of* $1 \times 10^{12}\,\mathrm{cm}^{-3}$. The vertical bars indicate experimental variation, and the horizontal bars the variation in DC magnetic field within the near field of the antenna.

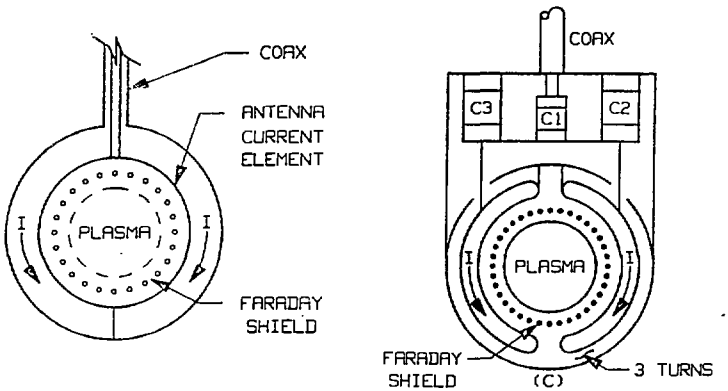

Figure 3.3: Schematics of the "double-half-turn" antennas used on TMX-U. The configuration used for the East antenna is shown on the left, that used for the West antenna is on the right.

power for each system is supplied by a Navy surplus AN/FRT-(86)V transmitter, modified to provide up to 400 kW in Class C operation. The systems are referred to by the location of the antenna for that system. One antenna is centered at an axial position 126 cm west of the central-cell midplane, the other at 186 cm east of the midplane. They are referred to as the West and East *i*CRH systems respectively. The West system was the first to be installed on TMX-U and as such has undergone the most changes since its original design. Both antennas are of the "double-half-turn" configuration, shown in Fig. 3.3. The main feature of this configuration is the RF current path splitting, so the current is in the same phase on each side of the plasma. This distribution of currents couples to odd numbered azimuthal modes, predominantly the $m = \pm 1$ modes. Of all modes, only the $m = -1$ mode has finite electric fields on-axis, and can heat the plasma more uniformly. The West antenna differs from the East in that each of the two

halves of the West antenna are composed of $3\frac{1}{2}$-turn coils. This was necessary to increase the inductance of the antenna to resonate in the 2-4 MHz range with the available tuning capacitors. This also multiplies the effective plasma loading a factor of nine over a single strap, and increases the voltage across the antenna for a given power. The East system was originally designed to feed a *slot* antenna, which had very low inductance, so a single current-carrying strap could be used.

As shown in Fig. 3.2, the plasma load is generally less than an ohm, while the transmitters are designed to drive 50Ω loads. To make the transition between these two, a *series-parallel* matching/resonating circuit is used. Due to the high powers involved, careful matching of line impedances was necessary to deliver the maximum power to the plasma, and to avoid damaging the output tube of the transmitter with high reflected power. The output of the transmitter is matched to the 50Ω coaxial transmission line, while the matching network transforms the plasma/antenna impedance to 50Ω. The circuits used in each of the systems are shown in Fig. 3.4. The inductance of the interconnecting bus bars is comparable to the East antenna inductance, and therefore must be accounted for when the response of the circuit to plasma loading is analyzed. This effective circuit for the East antenna and matching network is shown in Fig. 3.5. The West matching network is located inside the vacuum vessel of TMX-U to avoid high-current or high-voltage feed-throughs. The East matching network is external to the vacuum vessel due to its larger size. As noted above, it is designed to resonate a much smaller inductance than the West, which requires more capacitance for a given frequency.

The resonant frequency for a series RLC circuit is given by the equation, $\omega = \left(\frac{1}{LC} - \frac{R^2}{4L^2}\right)^{\frac{1}{2}}$. The plasma presents both a reactive and resistive load, and changes the resonant frequency of the circuit. The tuning of the matching

network must be adjusted to compensate for this load, to reduce reflected power. This requires accurate measurement of the plasma load to calculate the required tuning adjustments for the variable capacitors in the network.

3.4 Computer Control and Data Acquisition

3.4.1 Hardware Configuration

The transmitters used in the ICRH system are controlled and monitored by an HP9836 desktop computer and CAMAC based system. The system is designed to both control the output power of each transmitter, and to acquire, process and archive pertinent data for each plasma shot. Due to the limited space available inside TMX-U building (B435), the transmitters are located in trailers at the north side of the facility. Six-inch, semi-rigid, coaxial waveguide conducts the RF output to the impedance-matching networks, located on or within the central cell of TMX-U. CAMAC crates in each transmitter trailer communicate with the controlling computer via fiber-optic cables. This ensures ground isolation for the control room in this distributed system.

All the data acquisition, processing, display, and archiving is handled by an HP9836 desk-top computer. It is equipped with 1.75 Mbyte of RAM, a floating-point processor, and two $5\frac{1}{4}$ in. floppy disk drives for data storage. Plots of the reduced data are produced on an HP9876A Thermal Graphics printer. The computer is interfaced to the main TMX-U computer system via a LeCroy 8801 Dual-Port Memory and a Jorway A-2 Crate Controller, set up as the auxiliary controller in the the crate. Communication with the crates in each transmitter trailer is via a Kinetic Systems Serial Highway Driver, and fiber-optic links.

The output power level of the AN/FRT-(86)V transmitter is feed-back

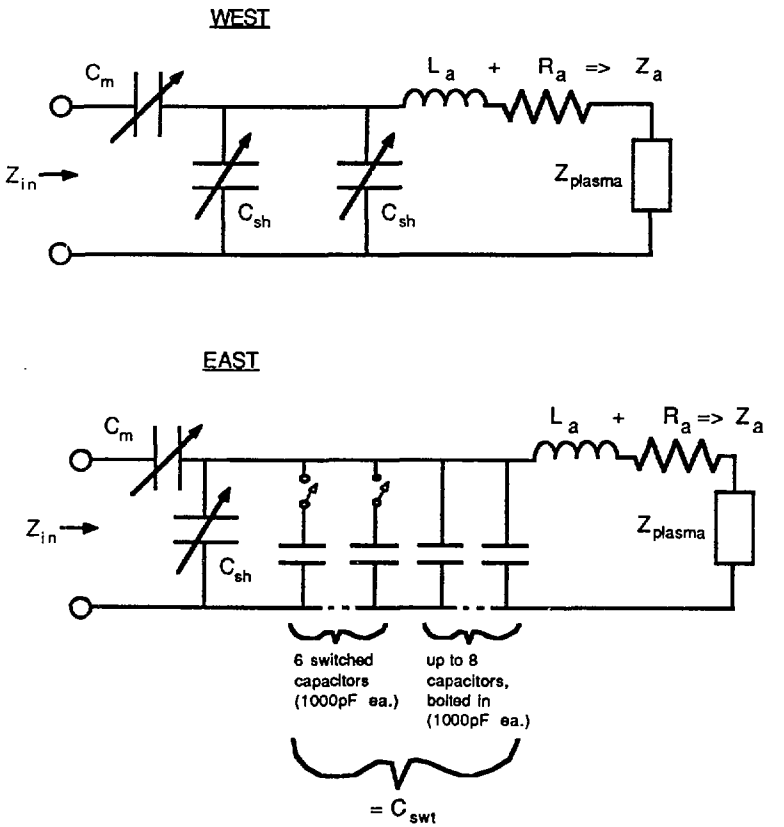

Figure 3.4: Circuit Diagrams for the East and West Matching Networks

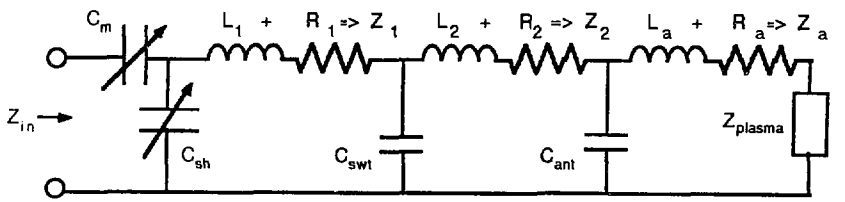

Figure 3.5: Effective Electrical Circuit for the East Matching Network

controlled[47]. A calibrated directional coupler in the output line of each transmitter provides means of monitoring forward and reflected power in the line. The couplers are made by the Dielectric Co., and are adjusted so the output signals are 84dB down from the line powers. The forward power signal from the directional coupler is first amplified to a level comparable to the input signal level to the transmitter and then rectified to a DC voltage. This level is then compared to a voltage set by the controlling computer via a digital-to-analog converter. The output of the comparator controls (with some intermediary circuitry) a voltage-controlled attenuator that adjusts the input signal level to the transmitter. In this way, the output power level is held constant, and can be set remotely from the control room. A similar circuit is used on the reflected power, but its purpose is to protect the transmitter and antenna from damage due to arcing, and as such, reduces the output to zero when the reflected power limit is reached.

The DC levels generated from the forward and reflected power signals are recorded by a LeCroy 8212T Data Logger located in CAMAC crates in the trans-

mitter trailers and are read by the controlling computer via the fiber-optic link. The levels have been calibrated against calorimetric measurements made by operating the transmitters into a water-cooled dummy load.

An HP8505A Network Analyzer is connected to a calibrated directional coupler in the output line of each transmitter to assess the complex impedance of the matching network and plasma load. The analyzer, in addition, provides the low-level RF source to drive the transmitters. The real and imaginary components of the line impedance are displayed on a Smith chart and recorded as a function of time during each shot by the 8212T Data Logger. The values are read and converted to plasma loading by the HP9836, in a procedure described in the section below. This information is also used in tuning the matching network for minimum reflected power during the plasma discharge. The variable capacitors in each matching network are adjusted remotely from each transmitter trailer.

3.5 Data Reduction and Analysis

In addition to providing control and recording of power levels, the HP9836 calculates the plasma loading on each of the ICRH antennas. This loading is used to ascertain the antenna coupling efficiency, to compare to code predictions, and to assist in tuning the matching networks for low reflected power.

The code for the HP9836 was written in BASIC, by the author, and has evolved over the period of several years from 20 lines to over 3500 lines, and now provides easy control over the myriad of parameters necessary for the ICRH system to function. The code is menu driven, using the ten user-definable *soft keys* provided by the HP9836. Data for each plasma shot is acquired, processed, plotted, stored, and transferred to the main TMX-U computer system in under 3 minutes. For each shot, the computer plots the forward and reflected power, real and imaginary

components from the Network Analyzer, and the real and imaginary components of the plasma loading as a function of time during the shot. The ICRH computer runs in a "auto-pilot" mode, receiving triggers from the TMX-U master timing system and the main computer system. The operator can exit this mode to perform more detailed analysis of the current shot, or previous shots.

There are two factors that determine the power actually broadcast from the antenna: the net power supplied to the matching network-antenna system, and the efficiency of the system, as defined in Section 3.3.1. The net power is simply the forward minus the reflected power as measured at the transmitter. The transfer function of the diode used to rectify the RF signal is non-linear in the range of operation, so a "look-up" table is used by the HP9836 to go directly from raw signal to power level, which greatly reduces inter-shot processing time. The raw signal is used as the index into an array, with the value of the element equal to power level corresponding to that signal. The loading resistance calculation, needed for the evaluation of efficiency, is described in the following section.

3.5.1 Plasma Loading Resistance Calculation

Plasma loading is calculated from the measured change in complex impedance seen by the transmitter during the plasma shot. However, the response of the network to the plasma loading is what is actually measured, so the effect of the network must be removed in order to get the plasma loading itself. Each network can be represented as a group of series and parallel elements. Each element is added or subtracted according to the rules of circuit theory for series and parallel elements. For simple resistances, series resistors simply add, and parallel resistors follow the rule:

$$R_{total} = \left(\frac{1}{R_1} + \frac{1}{R_2} \right)^{-1} \tag{3.16}$$

The same holds for capacitors and inductors, and combinations of all types, except that the complex impedance of the elements must be used and the equations must be evaluated in the complex plane.

The plasma loading can therefore be calculated from the complex impedance measured at the input to the matching network by adding or subtracting the impedances of each element of the network from the impedance measured at the output of the network. Written in terms of the labels in Figure 3.5, the plasma loading impedance for the East antenna is given by:

$$Z_{plasma} = ((((((Z_{in} - X_m)^{-1} - X_{sh}^{-1})^{-1} - Z_1)^{-1} - X_{swt}^{-1})^{-1} - Z_2)^{-1} - X_{ant}^{-1})^{-1} - Z_a \tag{3.17}$$

where: $X_i \equiv -\frac{jC_i}{\omega}$ and $Z_i \equiv j\omega L_i + R_i$. The loading for the West antenna is calculated in a similar manner.

The accuracy of the above calculation depends on knowing the exact capacitance of the variable capacitors in the network. The motor drives on each of the variable capacitors have been calibrated as accurately as possible, and the positions of each are read by the HP9836 for each shot, but the high "Q" of the network requires a more accurate measurement of these capacitances. To obtain the required accuracy, the measured values of capacitance are adjusted each shot to give zero plasma loading when no plasma is present. The equation used for this vacuum calibration is just the inverse of Eq. 3.17, with $Z_{plasma} = 0$. Corrections to the capacitance values for the series and shunt capacitors are given by this procedure. The correction for each is generally less than ± 100 pF.

The complex arithmetic needed for the above procedures is not intrinsic to HP BASIC. Routines were written using the vector operations available in HP BASIC, saving processing time. The complex impedances are stored as 2 by 1024 matrices (real and imaginary components for each of 1024 time points), and the routines

add, multiply, subtract and divide them as if they were single ordered pairs.

The above procedure yields both the real and imaginary plasma loading impedance, which is used to assess the coupling efficiency of each ICRH system, the actual power broadcast from each antenna, and provides a global check on ICRH theory.

Chapter 4

Description of REA System

A small probe, the Radial Energy Analyzer or REA, is used to measure the ion temperature, density, and potential as a function of radius in the center cell of TMX-U. This information is used in the calculation of the radial profile of ICRH power deposition, which is the goal of this dissertation.

The REA probe is of the retarding-potential type, but uses the magnetic field of TMX-U, rather than a negatively biased grid to keep electrons from reaching the recessed ion collector. The supporting electronics can sweep the ion collector in voltage up to 1.4 kV, at a 2 kHz rate, while measuring ion currents with magnitudes as small as 50 microamperes. The temperature, density and potential are deduced from the variation in collected current as the voltage is swept on the collector. The data analysis techniques used on the REA data will be discussed in the next chapter. The following sections describe the REA diagnostic in more detail.

4.1 Details of the Probe Design

The REA consists of an ion collector surrounded by two concentric shields. The probe relies on an external magnetic field perpendicular to the probe axis to prevent the free-flow of electrons to the ion collector as it is swept up in voltage. The probe measures only the ion current, and in this way differs from a Langmuir probe.[21] The proper operation of the probe is dependent on the electron gyro-radius being

much smaller than the ion gyro-radius. The ions, with their larger radius orbits, can reach the recessed collector, while the electrons hit the shields. This is true when the electron energy is less than $\frac{m_i}{m_e}$ times the ion energy. The probe is inserted perpendicular to the solenoidal magnetic field of TMX-U, at 72 cm east of the midplane of the device. A diagram of the probe head is shown in Figure 4.1. The ion collector and inner shield are made of tantalum and are housed within a 0.25 inch tantalum tube. The outer shield is insulated from both the inner shield and ground, allowing it to float to an equilibrium potential in the plasma. The small diameter of the probe allows it to be inserted into the center-cell of TMX-U without major perturbation of the plasma. The inner shield is biased 40 volts positive with respect to the ion collector and swept along with it. This inner shield serves to collect any secondary electrons produced within the outer shield before they can reach the ion collector and confuse the ion signal. The probe was originally designed by TRW[48] for a different plasma environment than TMX-U. The probe was built to measure the temperature of a heavy-ion plasma in a device designed for isotope separation. The probe ran un-cooled in the steady-state plasma. The plasma was formed by a microwave source, and the desired isotope resonantly heated by RF.

Two basic changes were made in the probe head when received from TRW. First, the inner shield was centered and insulated by a Pyrex tube which extended approximately half the length of the outer tube. This kept the inner electrodes centered in the outer tube. This change was needed due to the longer probe length required (due to the larger plasma diameter in TMX-U). The tube and the inner shield were held in place with a high-temperature *Sauereisen* cement. The whole probe head was baked overnight at 200° C to drive off residual water in the cement. This baking increased the resistance between the inner and outer shields from

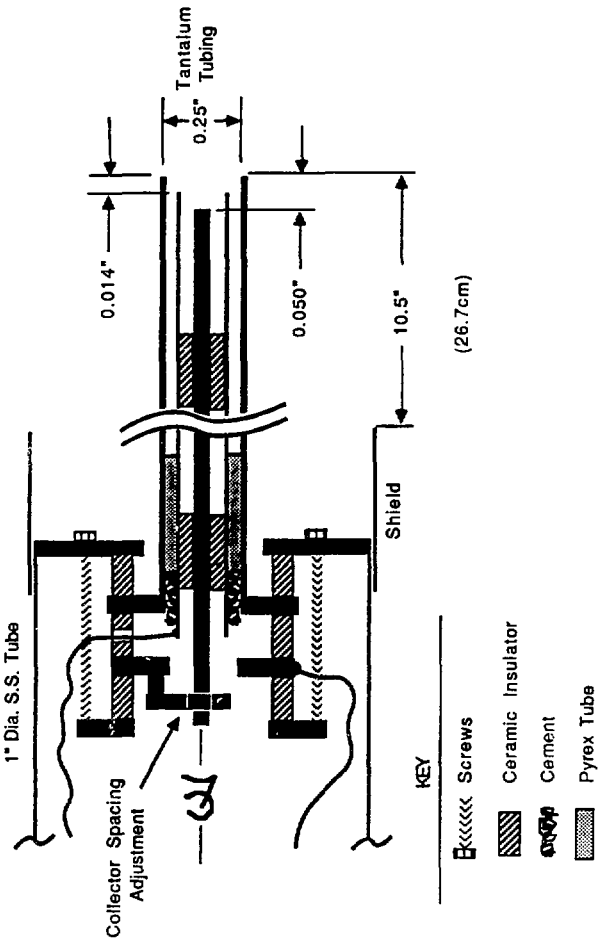

Figure 4.1: REA Tip Detail

$\simeq 10^3\Omega$ to over $10^7\Omega$. Second, the center ion collector was recessed further, from 0.020 to 0.050 inch, to discriminate against higher energy electrons. The presence of a small population of warm ($\geq$1 keV) electrons in the center cell of TMX-U is postulated to be due to the heating of electrons by microwaves scattered from the plug ECRH regions. The presence of these warm electrons was evidenced by a negative collector current at high voltage, during operation before the collector was recessed further. The 0.050 inch recession is sufficient to discriminate against 15 keV electrons, while only rejecting 3 eV deuterons.

The REA is designed to be a fairly rugged probe. The probe head is constructed entirely of refractory metals, high-temperature cement, Pyrex, and ceramic insulating materials. As such, the probe should be usable at temperatures up to 400°C. The Pyrex is the limiting material, the tantalum tip is able to withstand temperatures up to its melting point of 3000° C or until thermal emission from the collector becomes a substantial fraction of the collected current. The temperature limits, however, were not tested.

4.2 Remote Drive

Changing the radial position of the REA during an experimental run is accomplished using a remotely-controlled positioner. A photograph of the drive as mounted on TMX-U is shown in Fig. 4.2. It features a remotely movable range of 60 cm, which is ample to move the tip of the REA from behind the radial limiter in the center cell, to the the axis of the machine. Remote positioning of the probe saved the 10 to 15 minutes required to enter the TMX-U vault, due to the safety procedures required. This allowed data to be taken at many more radial positions than would have otherwise been possible. The radial motion is accomplished by a motor-driven lead screw positioning the bellows-mounted platform that holds

the probe shaft. The shaft passes through a Wilson seal on that platform which enables the probe to be inserted to a position near the plasma while the TMX-U chamber is evacuated. During operation, the shaft is locked at the Wilson seal and the bellows accommodates the range of motor-driven travel. The probe also can be withdrawn back into a spool behind a gate valve. This allows removal and installation of the entire probe while the TMX-U chamber is under vacuum. A photograph of the REA from inside the center cell of TMX-U is shown in Fig. 4.3. The photograph was taken during a maintenance period, during the calibration of the REA positioning. The large ring-shaped object in the foreground is the mid-plane gas-box, used to fuel the plasma. The crosshairs were installed for the REA position calibration. The REA comes down from the top, in the upper right quadrant. Also visible in the photograph is the 8-tip RF probe (at the top), the 2-tip Langmuir probe (at the left edge), and the East ICRH antenna housing (center, with the Faraday shield tubes just visible).

4.3 Sweep Supply Design

The expected plasma conditions determined the design parameters for the sweep voltage supply. The supply had to bias the tip to several times the ion temperature above the plasma potential, at kHz sweep rates, while providing up to 100 mA of current. An audio amplifier and step-up transformer circuit met these requirements without the cost or hazard of large capacitor banks.

The sweep supply for the REA has to satisfy two obviously conflicting requirements. The probe collects ions from the plasma, and to avoid distorting the signal, the supply must provide a low impedance to ground. At the same time, it must bias the tip to over a kilovolt. A compromise is reached by placing a 0.1 microfarad capacitor on the output of the high voltage supply. Although this limits the

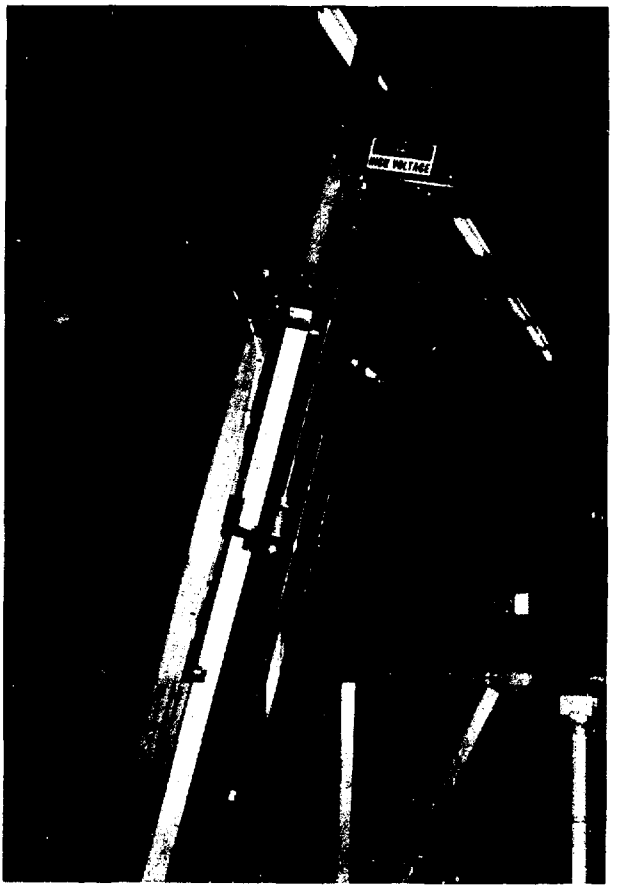

Figure 4.2: Photogragh of the Remote Drive Used to Position the REA on TMX-U

Figure 4.3: Photograph of the TMX-U Center Cell, Showing the Position of the REA and Other Diagnostics

power available at higher sweep rates, it provides an effective low impedance path to ground for the collected charge, and increases the high frequency capabilities of the supply.

A voltage doubler circuit was used to relax the requirements on the transformer (a stock 60 Hz filament type, with the primary and secondary reversed, yielding a 8:1 step-up). The sweep circuit and data acquisition system is diagrammed in Fig. 4.4. The voltage-doubler design also changes the shape of the input waveform, adding a short period of constant, negative voltage while the 2.0 microfarad series capacitor is discharged through the diode (this voltage, $\simeq$25 volts, is the forward bias voltage of the diode stack used). This portion of the waveform, roughly one-quarter of the sweep time, was very useful in determining the level of density fluctuations in the plasma. A representative waveform is shown in Figure 4.5.

As will be explained in Section 4.5, the capacitance of the cabling from the sweep supply (where the current monitor is located) to the probe tip must be kept low. The cabling from the sweep supply to the top of the probe shaft is RG-58 co-axial cable enclosed within a 3-inch diameter corrugated copper conduit. The cable is centered in the conduit by plastic washers secured to the cable approximately every 30 cm. The conduit is terminated at a box at the top of the probe shaft. The inner cable is then connected to a short jumper which connects to the vacuum feed-through at the top of the probe shaft. Connection to the probe head is via teflon-jacketed co-axial cable, held away from the inner walls of the probe shaft by Macor ceramic washers.

4.4 Choice of the Driver Amplifier

Many available commercial amplifiers are suitable for driving the voltage doubler circuit, or replacing it entirely (Kepco, Inc. makes several, for example),

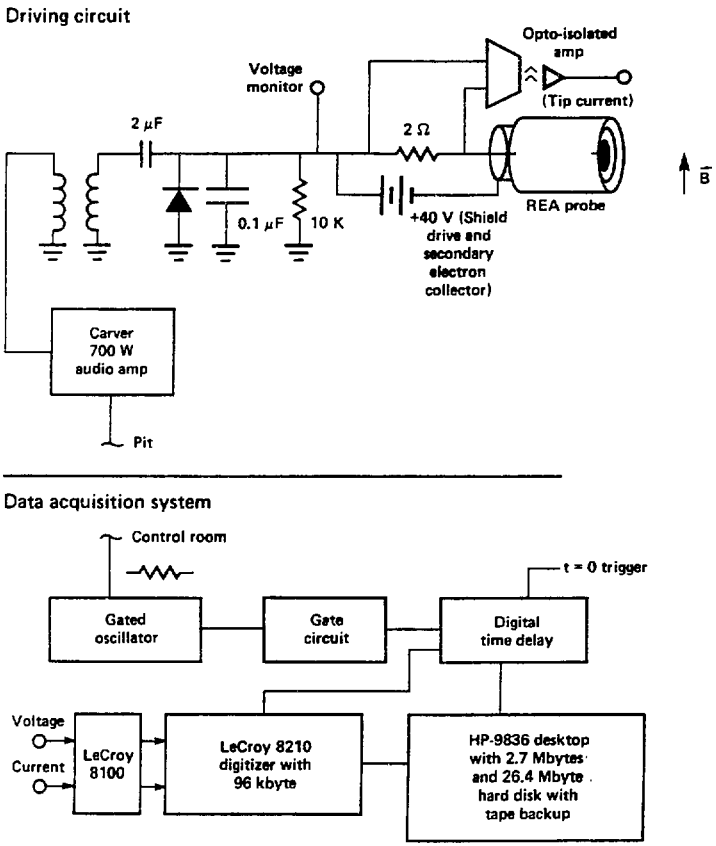

Figure 4.4: Diagram of the Sweep Supply Circuit and Data Acquisition Hardware

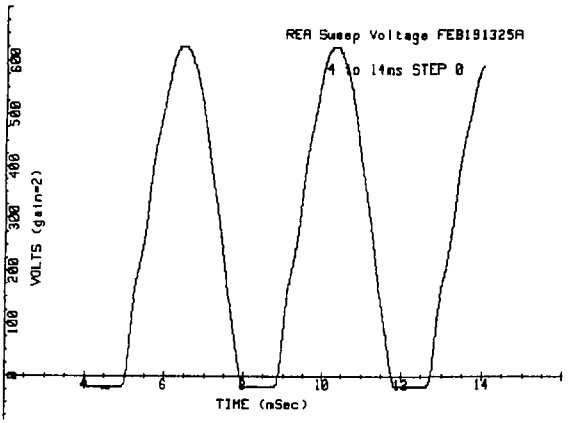

Figure 4.5: Typical Waveform Provided by the Sweep Supply

but considering the constraints of time and money, a less costly alternative was needed. A survey of available hi-fi equipment quickly showed that the Carver 500t amplifier would suit our needs. The amplifier was found at a local stereo shop, ready for immediate pick-up. The amplifier is rated at 700 watts when bridged for a single channel. It was tested and found to supply up to 74 volts into 100k ohms or up to 100 amperes into 0.1 ohms (for short pulses). Even through the transformer and doubler circuit, the amplifier was able to follow the changing load (due to the plasma), until the maximum power rating was reached.

4.5 Current Sensing Electronics

The current sensing electronics were supplied by TRW along with the probe head and were used without major modification. The basic feature of the system is the ability to measure micro-amperes of current while the tip is swept to 1 kV at a $\geq$1kHz rate. Ordinarily, capacitive displacement currents would be near a

milliampere under these conditions, which is comparable to the plasma signal. The circuit employs the technique of shield driving to reduce the effective capacitance of the cabling from the sweep supply to the tip. By sweeping the voltage on the outer shield of the RG-58 cable along with the center conductor, the capacitance is reduced from nearly 500 pF to less than 80 pF. This reduced the displacement current to less than 0.05 mA, which is generally much less than the plasma currents observed on TMX-U.

An optically-coupled amplifier is used to transfer the current signal from the high voltage portion of the circuit to the data recorders safely. A Burr-Brown 3650KG isolation amplifier was used for this purpose. The amplifier has sufficient isolation (120dB at a maximum voltage of 5 kV) but has a limited bandwidth. Its 3dB bandwidth of 15 kHz limits the usable sweep rate to around 1kHz. The effect of the integration effect of the amplifier is discussed in Section 5.4. In retrospect, a higher bandwidth optical coupling would have made the data analysis simpler, and would have allowed better time resolution. This should be considered for subsequent applications of the REA.

Sweep voltage on the tip is monitored with a simple, resistive divider, located at the output of the sweep supply. Line drivers are used to send the signals for current and sweep voltage from the pit to the control room, via tri-axial cable. The rest of the signal handling electronics are located in the TMX-U control room and will be described in the next chapter.

Chapter 5

Data Acquisition and Analysis

An important part of any diagnostic system is the method used to record and process the raw signals from the active portion of the diagnostic. Equally important is the interpretation of the raw data, the corrections for the limitations in the electronics, and the conclusions made from the processed data. The REA signals were recorded digitally, which allowed detailed analysis on a vast amount of data. The hardware used to condition, record, and process data from the REA, as well as the processing algorithms used, are described in the sections below.

5.1 Description of Data Acquisition Hardware

The REA electronics are CAMAC based, and are located in a rack in the south control room of the TMX-U facility. A photograph of the equipment rack containing the REA electronics is shown in Fig. 5.1. The cables from the pit are terminated at the top of the rack, and then go to the electronics in the CAMAC crate below. The control panel for the remote positioner is located below the terminations. A second panel for cable terminations is next, just above the CAMAC crate. Below the crate is a storage oscilloscope which provides an immediate display of the raw signals. This is used to ensure the system is functioning properly, and that the signals are within the ± 5 volt range of the digital recorder. Below that is the HP9836 computer, with the 4.8 Mbyte hard disk and the signal generator on

top. The 26.5 Mbyte hard disk and the ThinkJet printer are located on the table next to the rack. A schematic of the REA electronics is shown in Fig. 5.2.

The current and voltage signals are sent from the TMX-U pit to the control room via tri-axial cables. The cables are driven by high-accuracy and stability PMI Amp-01 line drivers. In the control room, the tri-axial cables carrying the current and voltage signals are first connected to a LeCroy 8100 Dual-Differential Amplifier. This amplifier enables the signal levels to be adjusted to match the ± 5 volt input range of the LeCroy 8210 Data Logger used. The differential input also reduces noise pick-up from the TMX-U magnet system. The outer shield of the tri-axial cables are grounded only at the equipment rack in the control room to avoid ground-loop problems. The recorder is equipped with 96k words of memory and can be run at sample rates of up to 1 MHz. However, to record two channels for the entire shot, the recorder was run at 500 kHz. This gave a 96 millisecond record for each channel, with ample time resolution. The analog filtering required to avoid digital aliasing was performed by the 100 kHz bandwidth of the LeCroy 8100 amplifier. Communication between the CAMAC crate and the Hewlett-Packard 9836 desktop computer is via an AEON 5488 Crate Controller and HPIB interface. The HP9836 computer is equipped with 2 Mbyte of memory, a floating-point arithmetic card, an HP ThinkJet printer, and 4.8 Mbyte and 26.5 Mbyte hard disks (with tape back-up). The system acquires, processes, plots, and stores the data for a each shot in 4 to 9 minutes. This time is shorter than the 10 minute minimum between shots on TMX-U.

5.2 Current-Trace Theory and Data Analysis

The theory and operation of this type of retarding-potential analyzer was first presented by Katsumata and Okazaki[10], and has been used successfully in other

Figure 5.1: Photograph of the REA Equipment Rack

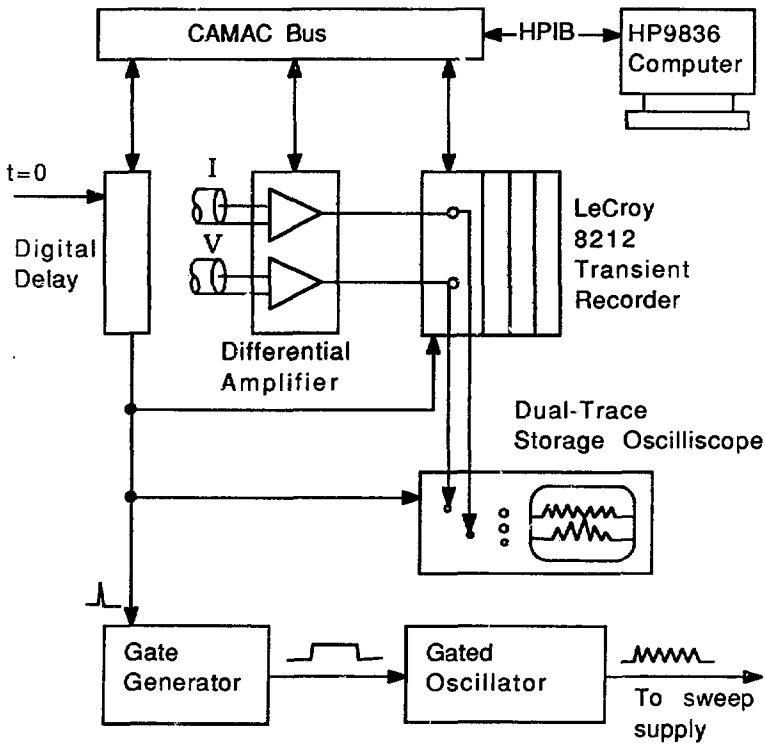

Figure 5.2: Schematic of the REA Data Acquisition Electronics

applications.[51,48,49,52,53] For a Maxwellian distribution of ion energies, the current of ions able to reach a biased collector is given simply by the Boltzmann equation:

$$I = I_0 \cdot \exp\left(\frac{-eV}{kT_i}\right) \tag{5.1}$$

where the current collected with no potential difference between the plasma and the probe, I_0, is taken to be the random ion current. The effective area of the collector is smaller than the physical area of the collector due to geometrical considerations and will be discussed in Section 6.3. The absolute magnitude of the current is not required to ascertain the ion temperature, only the slope of collected current vs. potential on the collector is needed. For an ideal probe, as the ion collector is swept up in voltage, the plasma current remains constant until the voltage on the tip exceeds the plasma potential. At potentials above this, the current falls exponentially, as determined by Eqn. 5.1, where $V \equiv V_{collector} - V_{plasma}$. As such, the data is best interpreted on a plot of $\mathrm{Log_e}(I)$ vs. V. The increase in temperature during ICRH is clearly seen as an increase in the slope of the I-V characteristic, above the plasma potential. This is demonstrated Fig 5.3. In practice, however, the plasma is not necessarily Maxwellian, nor as well-mannered as the theory assumes. Density fluctuations in the plasma on the same time scale as the sweep rate can make the determination of potential and ion temperature more difficult. It is assumed, however, that the basic shape of the $\mathrm{Log_e}(I)$ vs. V plot is two straight lines, intersecting at the plasma potential, with some random fluctuations superimposed on them. A least-squares fit to this shape was performed, with the "break" voltage identified as the plasma potential and the slope to the right of that point equal to the ion temperature. The ion density is proportional to the current at zero-voltage on the tip and the square root of the temperature. These are calculated for every sweep during a shot and plotted.

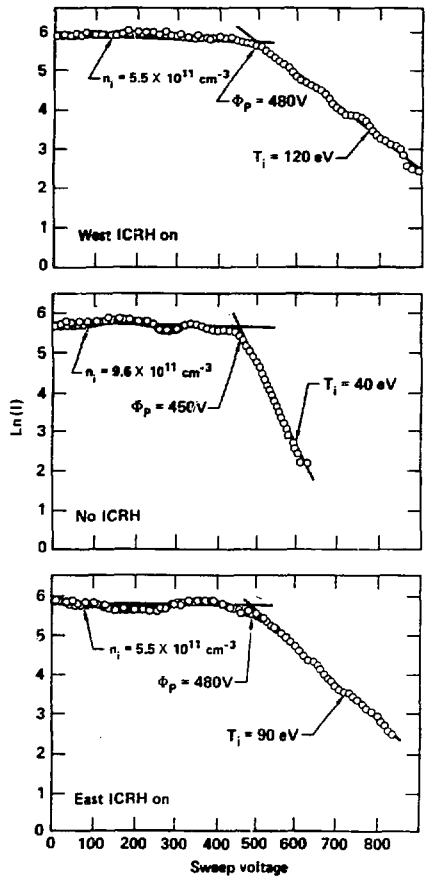

Figure 5.3: The change in slope during ICRH indicates an increase in ion temperature. The tip current at zero voltage and the temperature give the ion density. The voltage where the current starts to decrease is identified as the plasma potential.

5.3 Least-Squares Fit to Data

In order to find the "best" breakpoint, the current monitor data was first sorted, scaled, corrected for high-frequency roll-off (see Section 5.4), and the logarithm taken. Then twenty points, evenly spaced and locally averaged, were fed to a routine that evaluated the best break point, in the least-squares[54] sense, in this reduced set. The breakpoint was marched through the set, and lines fit above and below that point. The sum of the squares of the deviations from lines was calculated for each case, and the best breakpoint was chosen where this sum was at a minimum. This point was then found in the full data set, and two lines were calculated. The intersection of these lines determined the plasma potential. If the point found by the full data set wasn't close to that found by the sample set, a flag was raised, and that sweep was suspect. Large density fluctuations and potentials near or above the maximum sweep voltage were the most common causes of failure of this method. Each sweep used was visually checked to be sure the fitting routine was functioning properly. Sweeps that fooled the automatic routine were fit by hand.

5.4 Uncertainties in the Measurements

It would be misleading not to mention some of the limitations of this instrument, and some of the problems encountered in its use on TMX-U. The first problem that needs to be addressed is that of space-charge limits on the current collected. Since the ion collector is recessed more than a Debye length, and electrons are excluded from this region by the magnetic field of TMX-U, one must consider the effects of space-charge. McCarrick[52] examined this issue for a similar probe and found that near the plasma potential an ion saw the retarding voltage increased proportional

to the ion density, n_0, and the recessed distance, d, squared. The equation given in the paper reduces to:

$$\Delta V \leq \frac{\pi^2}{4} e n_0 d^2 \tag{5.2}$$

If this equation is applied to the high density($\simeq 10^{12}$ cm^{-3}) operation of TMX-U and the REA geometry, the ions would see several hundreds of volts over the applied voltage on the tip. Although not expressly stated, the derivation of Eqn. 5.2 was apparently done for zero temperature. Even though the effects are lessened at finite temperature, this could explain the reduction in current observed as the probe is swept up to the plasma potential.

To model the space charge effects of a finite temperature ion distribution on the REA characteristic, a code was written. The code solves for the self-consistent potential of a Maxwellian ion distribution traversing a gap to a biased plate. The code is 1-D, and is described in detail in Appendix A. The code showed that the effects of space charge are most perturbing at low ion temperature and high density, and modify the I-V characteristic most when the probe bias voltage is near the plasma potential. All these dependences are somewhat intuitive, however, the code quantified their effect. The code showed that the effect of space charge is only significant when the collector voltage is near the plasma potential. At densities above 5×10^{11} cm^{-3}, significant reduction in current occurs for ion temperatures of 5-25 eV, but becomes negligible at higher temperatures. Data taken at low temperature and high density was corrected for space charge by only using data points taken far from the plasma potential. The majority of data, however, did not need to be corrected.

Another problem encountered was the collection of electrons by the inner shield of the REA. This was due to warm electrons($\geq$1 keV) in the central cell, and to a slight misalignment of the probe to the local magnetic field. This warm population

was associated with ECRH in the plugs. Reducing the ECRH power reduced the electron current to the shield. Although it was assumed the electrons were intercepted by the inner shield and did not affect the ion signal, their current, at times, exceeded the power supply capability which reduced the peak voltage on the tip. This electron current to the shield had two effects. First, was to limit the maximum plasma potential the REA could measure (by reducing the maximum sweep voltage). Secondly, rapid changes in current to the shield resulted in a large $\frac{dV}{dt}$ (due to limited bandwidth of the power supply) which resulted in displacement currents in addition to the ion current. However, since the effective capacitance of the cabling is only 80 pF (due to the shield driving), this effect was not overwhelming.

Another anomaly is caused by the current sensing electronics. At low ion temperatures and high sweep rates, the limited bandwidth of the isolation amplifier gives a higher than actual temperature. Even at 1 kHz sweep rates, the decay time of the 3650KG can increase the apparent ion temperature. The response of the amp to a step reduction in current appears as a decaying exponential, and behaves the same as a finite temperature. The response of the 3650KG to a short, square pulse is shown in Fig. 5.4. This distortion can be removed to first order by pre-processing the raw data. At each point in time, the signal recorded is the sum of the actual signal and the signals at past times, multiplied by the proper decaying exponential factors. Subtracting off these contributions is approximated by subtracting the difference between the "i"-th and "$i-1$"-th sample, times the exponential factor, $\exp\left(-\frac{\Delta t}{\tau_a}\right)$. The amplifier decay time, τ_a, of 2.65 μsec. and the time between samples, Δt, is used for this correction.

To correct for the finite bandwidth further, an even number of sweeps are averaged together before the fitting routine is called. In this way, the lag in the

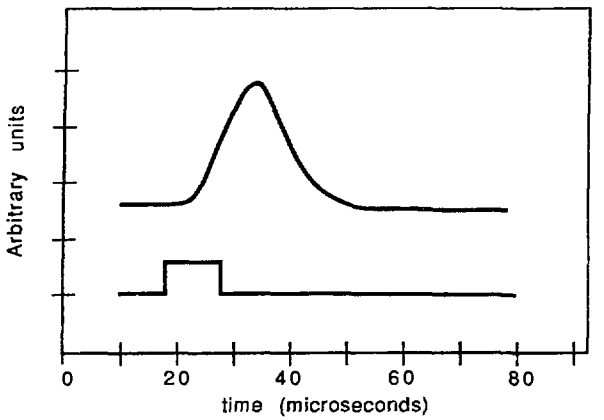

Figure 5.4: Response of the Burr-Brown 3650KG amplifier to a short pulse. This data was taken using a signal generator and the 3650KG installed in the current measuring circuit used.

signal caused by the amplifier on the up-sweep is approximately cancelled by the lag on the down-sweep. To maintain time resolution, only two sweeps are usually averaged, with more averaged if plasma fluctuations are present.

Inherent uncertainties in the measurement of temperature and potential are small. The voltage and current monitors were calibrated to better than 5% on the bench, and cross-checked after installation. This check used the difference in currents recorded as the sweep frequency was varied from a few hertz to several kilohertz into the known load at the output of the sweep supply. At the low frequencies, the 10 kΩ damping resistor predominates. At the higher frequencies, the 0.1 μF capacitor becomes substantial. For this test, the total current drawn from the supply was measured, not just the tip current. From two points, and Ohm's law, both the current monitor and the voltage monitor could be calibrated. The uncertainty in the measurement of ion density is greater, as it depends on

the effective ion collector area, the angle of acceptance, and the ion temperature. Comparison with the line-density obtained from microwave interferometry gave less than 20% difference in most cases. Plasma fluctuations cause some uncertainties, but they should average out. The validity and accuracy of the measurements made by the REA are addressed in the next chapter.

Chapter 6

Correlation with Other Diagnostics

The measurements of ion temperature, density, and potential made by the REA can be compared to similar measurements made by other diagnostics on TMX-U. This provides a check on the calibrations and analysis technique used on the REA data. The following sections describe the comparisons between the REA measurements and the PPD, ELIS, MIS, DML, and TOF measurements. Although these diagnostics generally do not measure exactly the same parameters, or in exactly the same location as the REA, under the proper conditions, they can verify the REA measurements.

6.1 Plasma Potential Diagnostic (Potential)

The potential measured by the Thallium Beam Probe-Plasma Potential Diagnostic (PPD) generally was higher than the potential measured by the REA, even measuring at the same radius. However, the absolute calibration of the PPD is difficult in that the plasma potential is calculated from the difference of two large energies, as discussed in Section 2.4.10. Several calibration shots were taken with a flowing plasma and no axial confining potentials. These shots indicated that the PPD had an offset of 150-300 volts, compared to both the REA and the

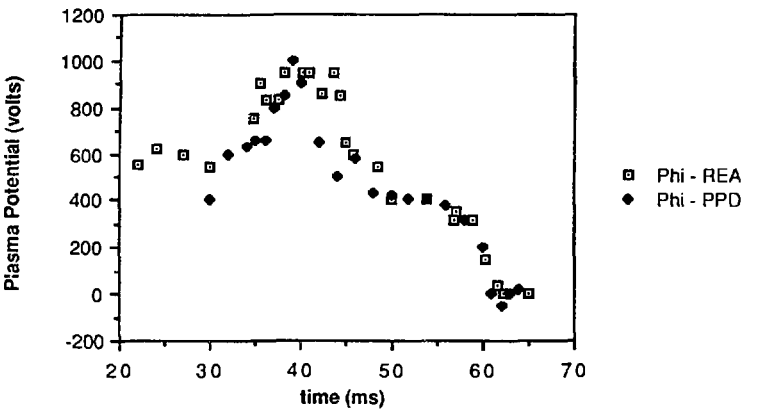

Figure 6.1: The Potential Measured by the REA and PPD as a Function of Time

ELIS. The offset varied on a day-to-day basis, which was attributed to changing the PPD's ion source operating parameters. Relative measurements of potential made by the PPD, however, are accepted as valid. A plot of plasma potential during a shot where the potential ranged from 0 volts to nearly 1000 volts is shown in Fig. 6.1. On this plot, the PPD measurement has a 200 volt offset subtracted. The data shows that the potentials measured by the PPD and REA generally tracked together within ± 50 volts over a range of potential of nearly 1000 volts.

The potential profile for one radial scan is shown in Fig. 6.2. When the comparison is done during a series of shots where the REA and PPD are scanned in radius, there is more scatter in the data, but the two measurements generally are within ± 100 volts. This is partly explained by shot-to-shot variations, and the fact that the PPD wasn't always set to view the same radius as the REA on each shot. For this scan, taken on a different day than the shot used above, the offset in the PPD-measured potential is 300 volts.

The agreement between the PPD and the REA measurement of potential val-

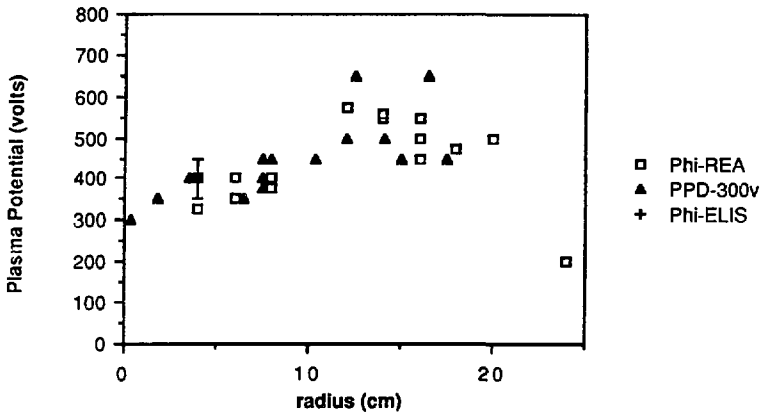

Figure 6.2: Radial Potential Profiles Measur · the REA and the PPD

:s the assignment of the break in the $\log_e(I)$-V plot as the plasma potential. However, since the PPD only can provide relative changes in potential accurately, another, absolute potential measurement is needed. The end-loss ion spectrometer is independently calibrated and can provide another check on the REA measurement of potential.

6.2 End-Loss Ion Spectrometer (Φ_p and T_i)

The potential and temperature given by the REA was compared against the End-Loss Ion Spectrometer (ELIS) measurements under a variety of plasma conditions. The ELIS is located on the end wall of TMX-U and analyses the ions lost out the ends. The shape of the energy distribution of these ions gives the ion temperature and the maximum potential they surmounted to escape. For this calibration, the REA was inserted to 4.0 cm, the same radius as the ELIS measurement, mapped from the end-wall to the central-cell midplane. During

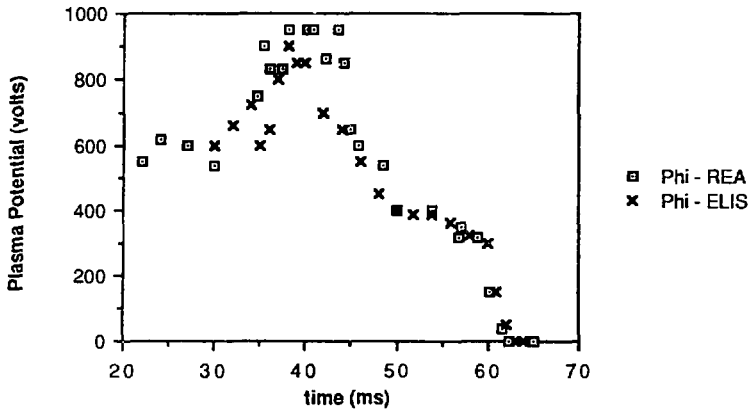

Figure 6.3: Comparison of Potentials Measured by the ELIS and REA

the calibration described above, the potential measured by the two diagnostics was generally within ±20%, throughout each shot. The agreement was better when the plasma was more quiescent, as it was after 45 ms. on the shot shown in Fig. 6.3. Density fluctuations can move the apparent break in the data associated with the potential. The fitting routine that picks out the break in the data cannot distinguish between changes in collected current due to density fluctuations or due to the changes in tip voltage as it is swept. This is especially true when the fluctuation frequency is comparable to the sweep frequency of the voltage on the tip. All data used in the detailed analysis was hand checked to be sure the routine was not obviously in error. This comparison with the ELIS is a more stringent test of the calibration and interpretation of the REA data than the comparison with the PPD as both diagnostics are used without any empirical offsets in the potential given.

The ELIS also provides a check on the REA measurement of ion temperature in the center cell. For conditions where the ions are cold, the two diagnostics

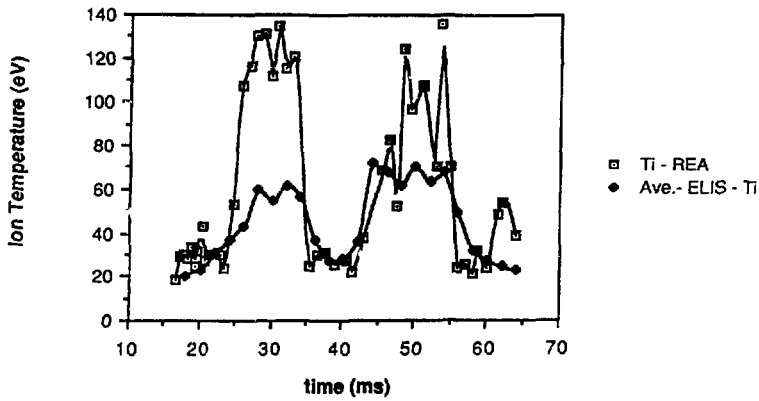

Figure 6.4: Comparison of Ion Temperature Measured by the REA and ELIS

give approximately the same temperature. However, when the center cell ions are heated by RF, the temperature measured by the ELIS is generally lower than that measured by the REA. This is shown in Fig. 6.4. This behavior is not unexpected as the REA measures the perpendicular component of ion temperature in the central cell, whereas the ELIS measures the total energy of the ions that scatter out. The RF heating adds energy to the motion perpendicular to the magnetic field, trapping them more deeply in the magnetic mirror of the center cell. These ions have a chance to drag down in energy before being lost, and must diffuse over any confining potential in the plugs. At higher temperatures, the average temperature measured by the two ELIS's was roughly one-half to three-quarters the temperature measured by the REA, depending on the ion temperature. This temperature-dependent factor was assumed to hold for all radii, and was used to calculate the end-loss power off axis.

6.3 Microwave Interferometry (Density)

The plasma density measured by the REA was checked against the line-integrated density measured by the Microwave Interferometry System (MIS). The REA measures the local density, so the data from a radial scan is needed to compute the line integrated density to compare to the MIS measurement. The REA infers the ion density from the collected current and the measured ion temperature. The random ion-current density, j, in a plasma is given by[3]:

$$j\ (\mathrm{Amp-cm^{-2}}) = \frac{1}{2} ne \left(\frac{2kT}{\pi m}\right)^{\frac{1}{2}} = 4.424 \times 10^{-2} n_{12} T_i^{\frac{1}{2}}\ (\mathrm{eV}) \qquad (6.1)$$

The effective collecting area of the REA tip must be known in order to relate the measured current to the random current density in the plasma. The effective area of the collector is smaller than the physical area because the tip is recessed and some ion trajectories cannot reach it. There are two effects to consider: ions that hit the shields because their pitch angle is too small, and ions that can't reach the collector because their gyro-orbits are too small. The geometry and dimensions of the REA tip are shown in Fig. 6.5. The recessed tip is completely shadowed by the inner and outer shields for ions with pitch angles of 20.8° or less. The area of the tip that can be reached is reduced, in varying degrees, for ions with pitch angles up to 67.4° as well. Since this is a sizable percentage of available pitch-angle space, this reduction in current must be calculated, or at least estimated. The cut-off angle for a point on the collector varies with the position on the collector. The solid angle of view available for each point on the collector is integrated from the cut-off angle to vertical, and over the distance from d_1 to $a + d_1$. This is divided by the total length and 2π steradians to give the reduction fraction compared to an unobstructed view. The calculation is performed for straight-line ion trajectories, and for one direction. Using the notation from Fig. 6.5, the cut-off angle, θ_c, is

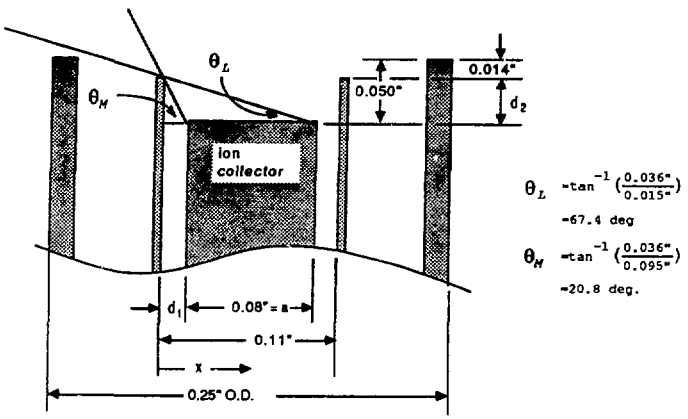

Figure 6.5: REA tip detail, for acceptance angle calculations

given by:

$$\theta_c = \tan^{-1}\left(\frac{d_2}{x}\right) \tag{6.2}$$

where x ranges from d_1 to $a+d_1$. The phase-space area available for a given cut-off angle is:

$$Area = \int_0^{90-\theta_c} \sin\theta \, d\theta \int_0^{2\pi} d\phi \tag{6.3}$$

$$= 2\pi(1-\sin\theta_c) \tag{6.4}$$

Combining equations 6.2 and 6.4, and integrating along the length of the collector, the fraction of the total ion flux that reaches the collector, $\mathcal{F}_a$, is given by:

$$\mathcal{F}_a = \frac{1}{a}\int_{d_1}^{a+d_1}\left(1-\frac{d_2}{(d_2^2+x^2)^{\frac{1}{2}}}\right)dx \tag{6.5}$$

$$= \frac{1}{a}\int_{d_1}^{a+d_1} dx - \frac{d_2}{a}\int_{d_1}^{a+d_1}\frac{dx}{(d_2^2+x^2)^{\frac{1}{2}}} \tag{6.6}$$

$$= 1 - \frac{d_2}{a}\left[\ln(x + (d_2^2 + x^2)^{\frac{1}{2}})\right]_{d_1}^{a+d1} \tag{6.7}$$

which, for the REA dimensions, is:

$$\mathcal{F}_a = 0.419$$

This indicates that the effective area of the ion collector is equal to 0.419 times the physical area. This, however, should be used with some caution. Ions are assumed to have an isotropic distribution for this calculation. A distribution weighted more toward the perpendicular, or with an empty loss cone, would have a smaller reduction in effective area. Also, the straight-line approximation of the ion trajectories is poorer at low energies, and should be considered further.

When there is no potential difference between the plasma and the ion collector, the lower energy limit on collection of ions is when their gyro-radius is equal to *one-half* the tip recession distance. This, however, requires the ion's helical trajectory to be in the exact phase to miss the shields and then spiral into the collector. The pitch angle also must be shallow enough to miss the shields as it gyrates along the magnetic field, yet not so shallow that it cannot hit the collector at all. Using the REA dimensions given above, and the magnetic field at the probe location of 3.2 kG, this threshold is 3 eV. This lower limit is only for ions in a small range of angle and phase. In actuality, the practical limit is two or three times this if only geometrical considerations are made. However, this picture changes when there is a potential difference between the plasma and the collector. During much of the operation of the REA, the plasma potential at the probe was over 100 volts, while the ion temperature was near 20 eV. When the ion collector is near ground potential, the the ions see an accelerating potential into the collector. Once the orbit of an ion takes it inside the REA tip more than a Debye length (only a few thousandths of an inch for TMX-U conditions), the electric field within can distort

the circular orbit sufficiently to hit the collector. This partially offsets the low energy cut-off due to the recession of the ion collector. This effect is not easily quantified, however. An estimate of its effect on the current collected is made by assuming that the potential increases the fraction of angles and phases of ion trajectories that can hit the collector. A low energy cut-off of 3 eV is used to account for the combination of these two effects.

The resultant reduction in current due to this cut-off can be estimated using a Boltzmann-like factor. The scrape-off of ions on the shield is similar to the reduction in flux associated with an increase in potential. The reduction factor, $\mathcal{F}_e$, is dependent on the ion energy, and can be written:

$$\mathcal{F}_e = \exp\left(-\frac{3\,\mathrm{eV}}{\mathrm{T_i(eV)}}\right) \tag{6.8}$$

For an ion temperature of 20 eV, this factor is 0.861, while for 100 eV, this factor is 0.970. The effective area of the ion collector is then the physical area, A (=0.0324 cm^2), times the two correction factors, $\mathcal{F}_e$, and $\mathcal{F}_a$. Starting with Eqn. 6.1, and taking $\mathcal{F}_a$ to be a fixed value of 0.419, the relation between measured current and ion density reduces to:

$$n = \frac{I}{4.424 \times 10^{-2}\, T_i^{\frac{1}{2}}\, \mathcal{F}_e \mathcal{F}_a A} = \frac{I}{6.0 \times 10^{-4}\, T_i^{\frac{1}{2}}\, \mathcal{F}_e} (\times 10^{12}\mathrm{cm}^{-3}) \tag{6.9}$$

Six radial profiles of density measured by the REA were line-integrated and compared to MIS measurements taken during the same sequence of shots. These profiles are used in the power balance performed in Chapter 8 and are shown in Figures 7.9 and 7.10. The line-integrals of the REA data for these profiles are given in Table 6.1. The MIS line-densities listed in the table are averages over the shots in the REA scan. The agreement between the two measurements of line-density is within 20% for all of the six cases, and within 10% for three of the six. The line-density from the MIS also has an associated uncertainty. The accuracy of the MIS

Scan #	ICRH	MIS Line-density ($\times 10^{13}$cm^{-2})	REA Line-density ($\times 10^{13}$cm^{-2})	$\frac{REA}{MIS}$%
4	West	5.9	6.3	106%
4	None	5.1	4.1	81%
4	East	6.3	5.7	91%
5	West	8.8	7.7	87%
5	None	7.6	8.3	109%
5	East	8.8	10.5	119%

Table 6.1: Comparison of MIS and REA measured Line-densities

determination of the line-density is generally taken to be around 10%, and had a shot-to-shot variation of a few percent during the REA scans as well. All effects considered, the agreement between the two was deemed sufficient to use the REA measurement of density in subsequent calculations without modification.

6.4 Diamagnetic Loop (Stored Energy)

The Diamagnetic Loop (DML) measures the plasma energy by measuring the magnetic flux excluded from within an axis-encircling loop, by the gyration of the plasma ions and electrons. This DML measurement provides a cross-check of both the density and ion temperature profiles measured by the REA. A radial integral of the product of average ion energy times the density gives a measurement of the total stored ion energy. A plot of stored plasma energy vs. time is shown in Fig. 6.6, along with three points showing stored ion energy, calculated from REA measurements. The ion stored energy is calculated by multiplying the REA measured energy (taken to be $\frac{3}{2}T_i$) and the density for each radius, then multiplying this by the area of a 2 cm annulus centered at that radius. These products are

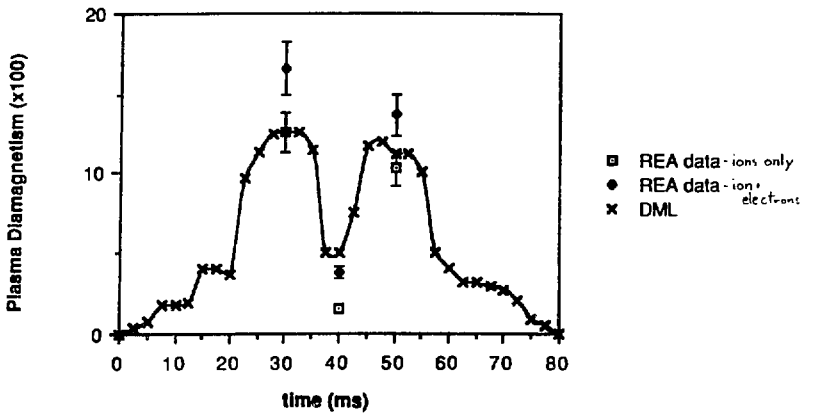

Figure 6.6: Measurement of Stored Plasma Energy by the REA and DML Show Good Agreement

summed and multiplied by the appropriate constants to give the stored energy in the same units as the DML measurement, Amp-cm. As shown in Fig. 6.6, the stored ion energies the REA obtained at were within 10% of the DML measurement during ICRH, but was nearly 70% lower than the DML measurement with no ICRH (at 40 ms.). This discrepancy for the time without ICRH could be explained by poor signal-to-noise ratio in the DML at low signal level giving an erroneously large reading, or the contribution of the electrons. A two-layer, electron temperature profile is used to estimate the contribution of electron diamagnetism to the DML measurement. For consistency, the same profile used in Chapter 8 is used for this check. The electron temperature is taken to be 40 eV out to 9.3 cm and then 20 eV out to the plasma edge. The stored energy is calculated in the same manner as the ions, using the density measured by the REA. Adding this estimate of the electron diamagnetism to that for the ions brings the total diamagnetism to within 25% of the DML measurement when both ICRH systems are off, but raises the total

well over the DML measurement when either ICRH is on. The total diamagnetism from the REA measured ion and assumed electron profile is 132% of the DML measurement during operation of the West ICRH and 122% during operation of the East. Ignoring the uncertainty in the DML measurement and the assumed electron temperature profile, this would indicate an uncertainty of 10 to 15% in the REA measurement of each the ion temperature and density. This is comparable to the difference between the REA and the MIS measurement of density, and the difference between the REA and the ELIS measurement of ion temperature (at low T_i only). This comparison with the DML provides an additional validation of both the temperature and density measured by the REA.

The DML measurement was also used to evaluate the perturbing effect of inserting the REA into the center-cell plasma. A plot of the DML signal vs. the REA position in the plasma is shown in Fig. 6.7. This plot shows that the DML signal was constant, within normal shot-to-shot variations, until the REA was inserted to a radius of 4 cm. Even then, there was only a 25% reduction in stored energy. Microwave interferometer measurements of the line density in the central cell show a larger variation as the REA is inserted, but the changes in density are still near the shot-to-shot variation level. This is shown in Fig. 6.8. This small perturbation is to be expected as the REA probe is small compared to the 24 cm plasma radius and the plasma temperature is modest. The effect of the probe can be assessed by comparing the ion current intercepted by the probe, to the current of ions lost axially and radially. If the probe current is small in comparison to other losses, it represents only a small perturbation to the plasma. The outer shield on the REA is electrically insulated from ground which forces the ion and electron current to the shield to balance. The potential of the shield drops to force the electron current to be equal to the random current of ions to the shield. This random current is

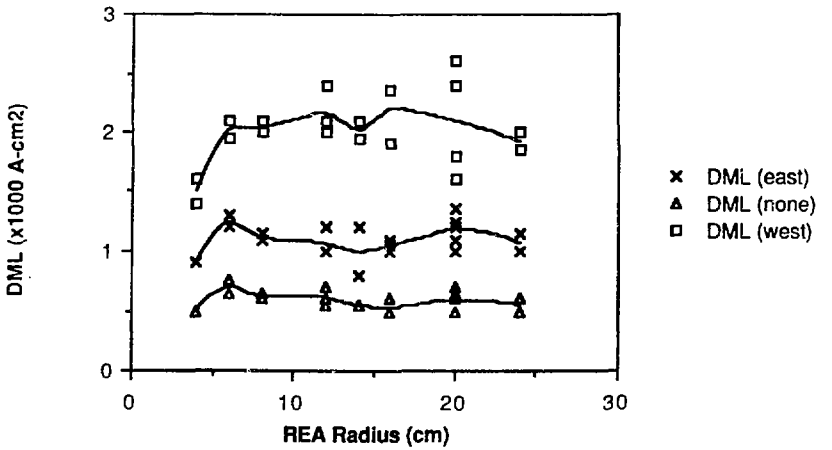

Figure 6.7: Plot of Diamagnetism vs. REA position in the central cell. The three traces are for the East, West, and no ICRH systems operating. The drawn lines are interpolations on the experimental data.

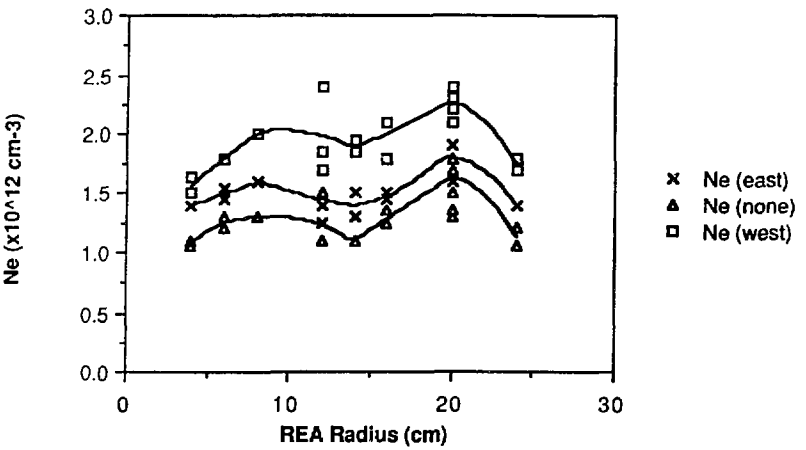

Figure 6.8: Plot of central-cell density vs. REA position in the central cell. The three traces are for the East, West, and no ICRH systems operating. The drawn lines are interpolations on the experimental data.

approximated by: $I_{random} = \frac{1}{4} n e v_{th} \cdot A_{shield}$, where v_{th} is the ion thermal velocity and A_{shield} is the surface area of the probe shaft. Using the surface area of the shaft neglects the fact that the ions are constrained to move along the magnetic field lines so the area normal to the field receives more current than the area parallel to the field. Using the total surface area is therefore an over-estimate of the current to the shield. In the limit of a cold plasma, the effective area is reduced a factor of π. The current to the shield was calculated for the measured profiles of density and temperature, for one of the scans used in the power balance in Chapter 8 (Scan #4) and the probe pushed in to its minimum radius of 4 cm. The total current to the shield was calculated to be 9 to 12% of the total of axial and radial losses measured during ICRH. Without ICRH, the central-cell ion temperature is much lower and the probe loss represents less than 3% of the total. The effect of this perturbation on the REA measurements is lessened even further due to the fact that ions reaching the collector are predominantly from orbits centered beyond or beside the end of the probe shield. These ions are therefore largely unaffected by the presence of the probe.

6.5 Time-of-Flight (Passing-Ion Temperature)

As an additional check on the ion temperature measurement, the REA measurement was compared to the passing-ion temperature measurement. The Time-Of-Flight (TOF) measurement of the passing-ion temperature is based on measuring the velocity spread of passing-ions that charge-exchange in the east plug region (described in Section 2.4.12). The TOF measurement showed an increase in passing-ion temperature with ICRH, but was generally lower than the REA measurement of ion temperature in the central cell, or the ELIS measurement at the end wall. The temperature measured by the TOF is shown as a function of

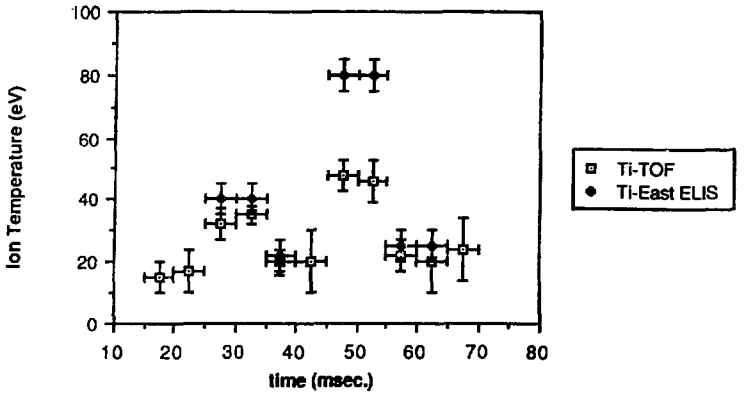

Figure 6.9: Passing-Ion Temperature Measured by the Time-of-Flight Spectrometer

time during one shot in Fig. 6.9. The TOF diagnostic is located on the East end of TMX-U, so the temperature measured by the East ELIS is plotted for comparison. The fact that the TOF measures a lower temperature than either the REA or the ELIS can be explained as before as a consequence of RF heating in the perpendicular direction. The TOF line-of-sight is inclined 22.5° to the magnetic axis, within the 30° loss-cone of the center cell (as measured at the midplane of the plug). In order to be detected by the TOF, an ion must scatter through a larger angle than is required to escape and be detected by the ELIS (see Section 2.4.11. Since lower energy ions scatter faster, it is plausible that ions at the lower pitch angles are colder. Since it is difficult to calculate the magnitude of this effect, and considering the fact that TOF measurements were not often available, the TOF was used only for qualitative comparisons.

This chapter has presented the experimental verification of the REA measurements of ion temperature, density, and plasma potential. Comparisons with other

diagnostics available on TMX-U have shown that the REA system functions as predicted, and yields measurements that are generally within 10 to 15% of other diagnostics. Although this is only a relative measure of accuracy, this will be taken to be the uncertainty in the REA measurements.

Chapter 7

Radial Profiles

The goal of this dissertation is the measurement of the radial profile of ion cyclotron resonance heating power in the center cell of TMX-U. Toward this goal, the REA was implemented to measure the radial profiles of ion temperature, density and plasma potential.

The REA was positioned at the edge of the plasma during many days operation of TMX-U, where it underwent the multitude of modifications, revisions, and system checks common to all new diagnostic applications. Although the goal of this dissertation is to measure the power deposition profile of ICRH under varied conditions, practical considerations dictate the extent to which this is possible. The TMX-U plasma discharges last approximately 70 ms, and are repeated at a maximum rate of one every 10 minutes. Allowing time for minor repairs and adjustments, a good day of operation will yield 30 to 40 plasma discharges, or *shots*. Of these, several shots will be used for set-up of desired plasma conditions, background subtraction, and system shake-out. Each scan of the REA probe requires 5-10 radial points to resolve the radial structure, which gives a practical limit of one or two scans per day of operation.

The pressure to achieve proposed milestones on schedule dictated much of the TMX-U experimental program, and limited the time available to ICRH studies. As such, TMX-U was made available for REA radial scans on only six days. Of these,

one was spent conditioning TMX-U after a maintenance period, one was spent searching for proper plasma conditions to perform a scan, and one was nearly completely taken by another experiment and equipment failures. Of the remaining three days, only on the last day did all necessary supporting diagnostics yield useful data. The following sections describe the radial profiles obtained on these days.

7.1 Plasma Conditions for Radial Measurements

For each day, the experimental conditions were set-up to provide as quiescent a central-cell plasma as practical, while keeping the density in the $1-3\times10^{12}\,\mathrm{cm}^{-3}$ range. The central-cell conditions were affected most by adjustments in the gas fueling rate and location, and by adjustments in the ECRH power levels. Neutral beam heating and fueling in the plugs was kept at the highest available current. This was done under the assumption that higher plasma pressure in the plugs would provide MHD stabilization for the center cell, and reduce the low-frequency fluctuation level, although a systematic study of this was not done. No central-cell neutral beams were used to avoid confusing the data analysis by introducing an additional power source, and an unknown interaction between the high energy ions and the ICRH.

After the first few days of running, a correlation between the 10 kG ECRH power and the fluctuation level in the central-cell was noticed. For the last day's running, the 10 kG system was only used for plasma start-up, with only end-cell beams, gas, and the 5 kG ECRH system sustaining the plasma for the time used for the ICRH study. Although outwardly these conditions were different from those used for the thermal barrier experiments, the conditions in the central cell were nearly the same. Since the RF coupling and heating is governed predominantly by the central-cell plasma conditions, the heating profile measured can be assumed

Scan #	Date of Scan	East ICRH Frequency (and ω_{ci} Ratio) (on-off times)	West ICRH Frequency (and ω_{ci} Ratio) (on-off times)
1 and 2	9/12/86	2.88 MHz ($0.85\omega_{ci}$) (40 - 55 ms)	2.78 MHz ($0.95\omega_{ci}$) (15 - 30 ms)
3	9/19/86	3.2 MHz ($0.95\omega_{ci}$) (40 - 50 ms)	2.3 MHz ($0.79\omega_{ci}$) (10 - 32 ms)
4 and 5	9/30/86	2.88 MHz ($0.85\omega_{ci}$) (42 - 55 ms)	2.55 MHz ($0.87\omega_{ci}$) (21 - 34 ms)

Taole 7.1: ICRH Frequency and Scan Identification

valid for thermal barrier conditions as well.

The plasma conditions and RF frequency were intentionally varied to check the modeling codes at more than one point in parameter space. Given the vastness of that multi-dimensional space, and the limited experimental time available, a thorough comparison between the codes and experiment was not possible. We were able to complete five radial scans with the REA, each of which had a different density profile, and included five different frequencies between the two antenna systems, covering three different frequency ratios with the local cyclotron frequencies. As noted above, the ECRH and gas fueling were varied on the three days as well. A summary of these different configurations is given in Tables 7.1 and 7.2. For ease of future reference, each scan will be given a number, as shown in these tables. In all the plots in this chapter, the lines drawn are smoothed, interpolated curves drawn through the experimental points. These lines are meant only to help group the data, not to indicate any theoretical fit.

Scan #	5 kG ECRH Power (on-off)	10 kG ECRH Power (on-off)	West Gas Box (on-off)	Mid-plane Gas Box (on-off)	Trans. Valves (each end) (on-off)
1	135 kW (5-70 ms)	75 kW (5-60 ms)	22 T-l/sec. (0-70 ms)	0 T-l/sec.	8 T-l/sec. (0-70 ms)
2	135 kW (5-70 ms)	75 kW (5-60 ms)	14 T-l/sec. (0-70 ms)	0 T-l/sec.	4.5 T-l/sec. (0-70 ms)
3	125 kW (5-70 ms)	75 kW (5-55 ms)	19 T-l/sec. (0-70 ms)	0 T-l/sec.	7 T-l/sec. (0-70 ms)
4	135 kW (15-70 ms)	95 kW (1-15 ms)	0 T-l/sec.	26 T-l/sec. (0-75 ms)	11 T-l/sec. (0-15 ms)
5	135 kW (15-70 ms)	95 kW (1-15 ms)	0 T-l/sec.	36 T-l/sec. (0-75 ms)	11 T-l/sec. (0-15 ms)

Table 7.2: ECRH Power and Gas Fueling Rates and Locations

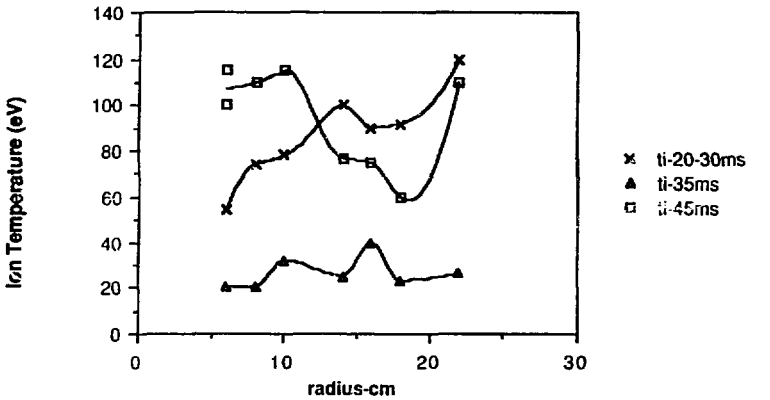

Figure 7.1: Radial Profiles of Ion Temperature for Scan Number 1

7.2 Temperature Profiles

The ion temperature profiles measured by the REA for the five scans are shown in Figs. 7.1 through 7.5. Each plot shows the ion temperature at times during the shots when each of the two ICRH systems were operating, and when there was no ICRH in the center cell

This temperature is, by itself, not a direct indication of the RF heating profile, but is crucial in the power balance used to obtain it. That is, a higher temperature near the axis could mean the power deposition is greater there, or that the energy confinement is better on-axis. The power balance performed in Chapter 8 will address this question.

7.3 Density Profile

The local density is calculated for the REA data by taking the current to the ion collector at zero bias voltage to be the random ion-current in the plasma, times

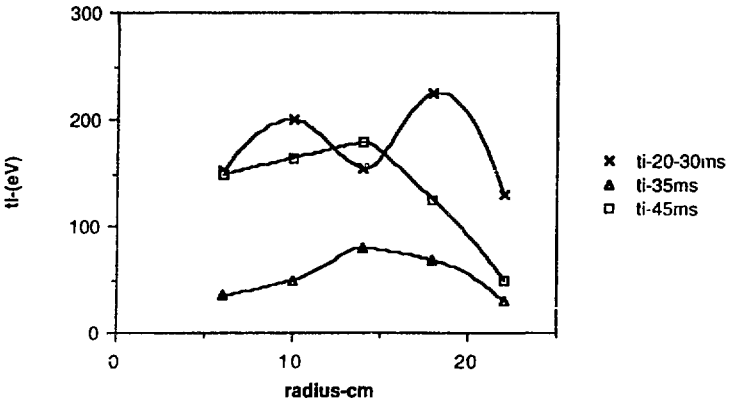

Figure 7.2: Radial Profiles of Ion Temperature for Scan Number 2

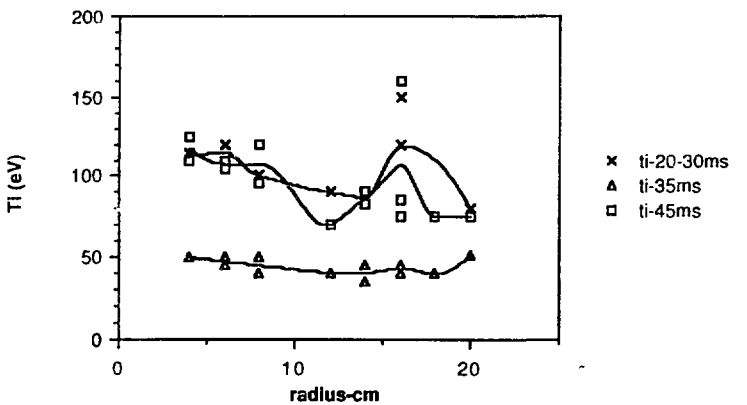

Figure 7.3: Radial Profiles of Ion Temperature for Scan Number 3

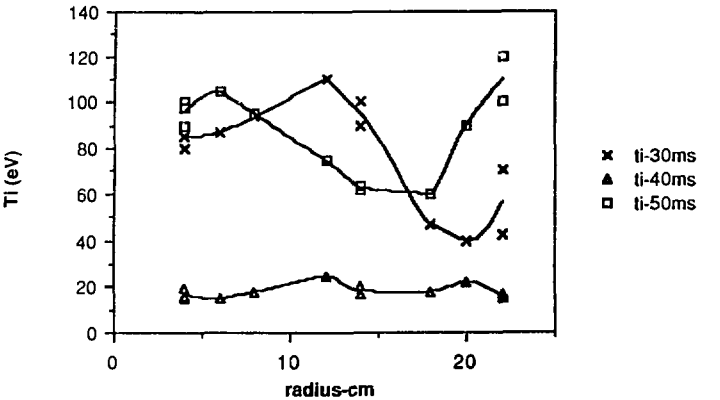

Figure 7.4: Radial Profiles of Ion Temperature for Scan Number 4

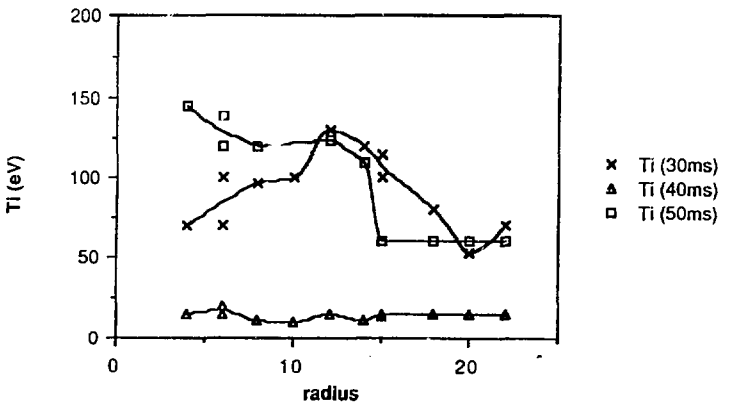

Figure 7.5: Radial Profiles of Ion Temperature for Scan Number 5

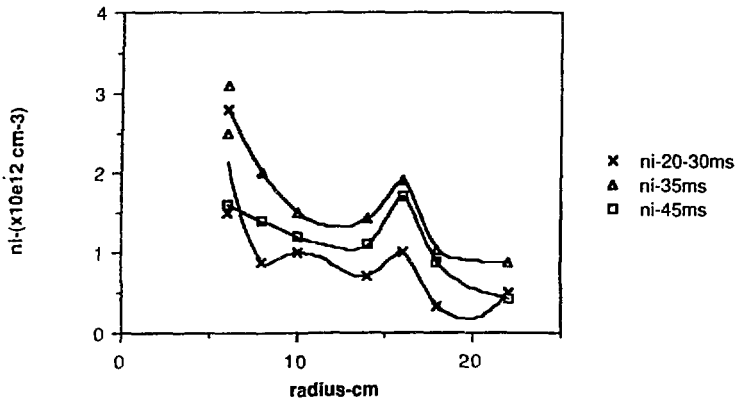

Figure 7.6: Radial Density Profile for Scan Number 1

two correction factors, as described in Section 6.3. The density profiles are shown in Figs. 7.6 through 7.10.

7.4 Potential Profiles

The break in the $\log_e(I)$ vs. V plot is identified as the plasma potential. This is described in Section 5.2. The radial profiles of the plasma potential for the five scans are shown in Figs. 7.11 through 7.15.

7.5 Summary of Profiles

There were several observed trends in the profiles measured by the REA. The potential profiles were generally flat, rising slightly toward the edge of the plasma, with the notable exception of Scan #2. This series of shots were taken with a low gas fueling rate, and the 10 kG ECRH system operating the whole shot. The combination of low density and 10 kG ECRH has been correlated with

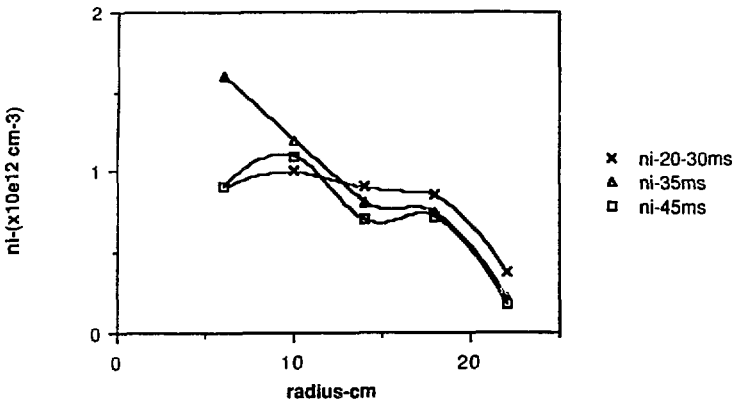

Figure 7.7: Radial Density Profile for Scan Number 2

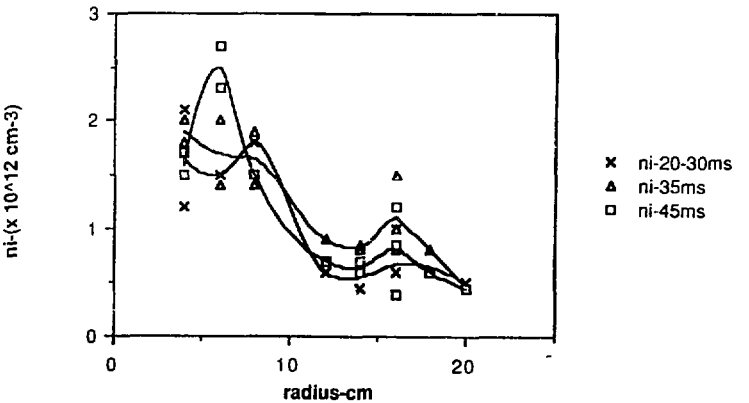

Figure 7.8: Radial Density Profile for Scan Number 3

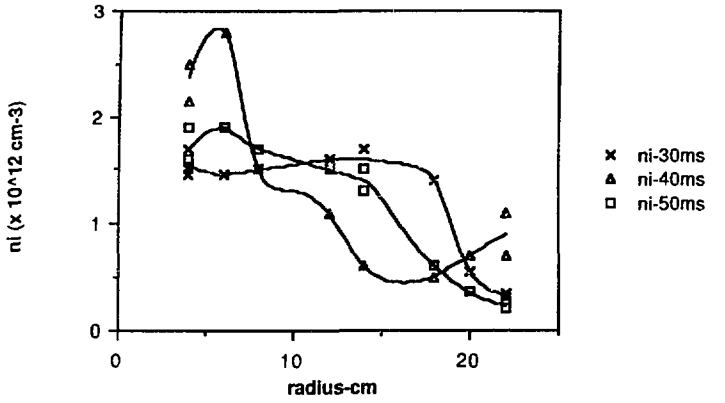

Figure 7.9: Radial Density Profile for Scan Number 4

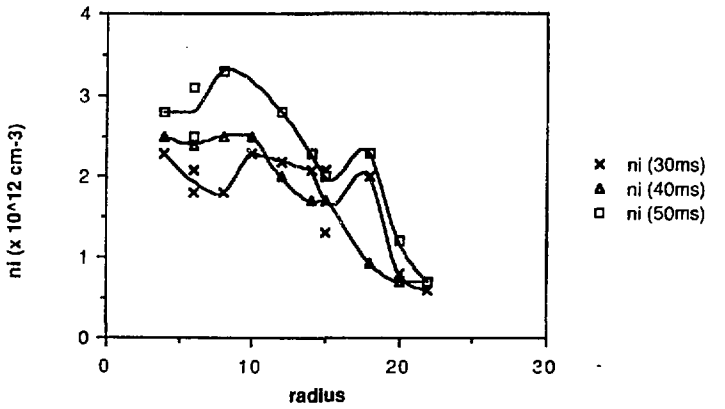

Figure 7.10: Radial Density Profile for Scan Number 5

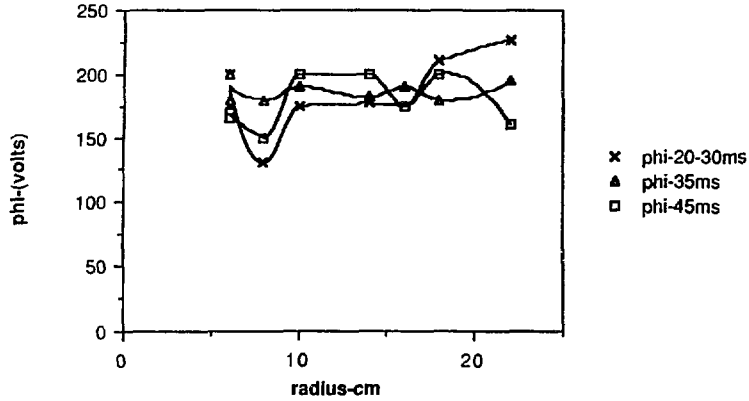

Figure 7.11: Radial Potential Profile for Scan Number 1

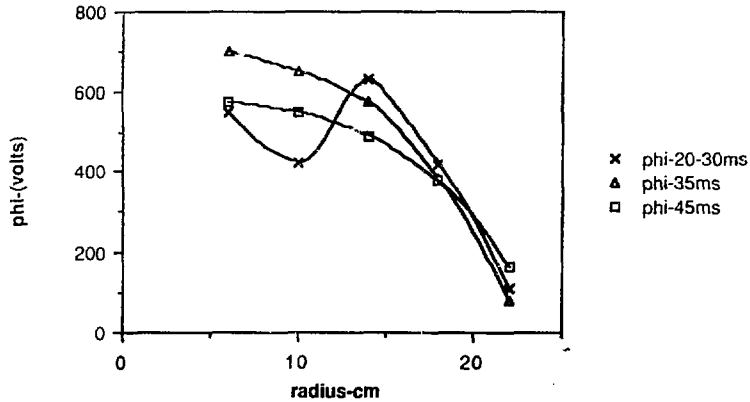

Figure 7.12: Radial Potential Profile for Scan Number 2

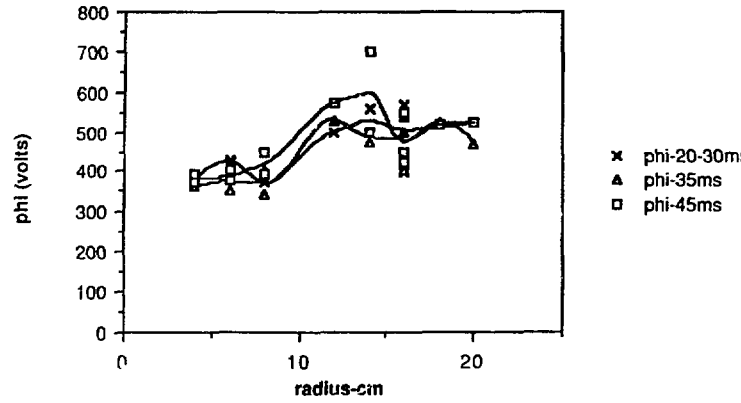

Figure 7.13: Radial Potential Profile for Scan Number 3

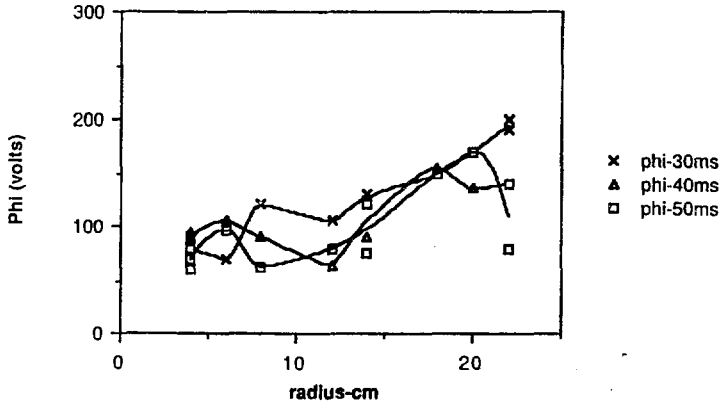

Figure 7.14: Radial Potential Profile for Scan Number 4

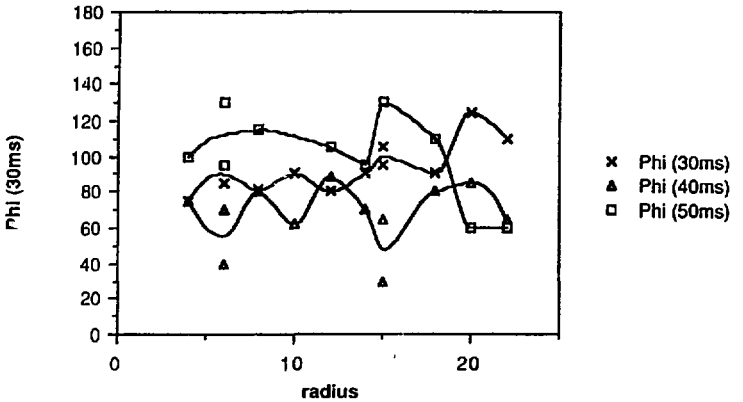

Figure 7.15: Radial Potential Profile for Scan Number 5

high potentials for much of TMX-U operation. Scan #3, also shows the higher potentials. The potential measured at a radius of 22 cm was generally over 100 volts, requiring a steep gradient to the grounded limiter at 24 cm.

The temperatures were generally higher in the core than off-axis, with a sharp increase at the plasma edge noted on Scans #1 and #4. Edge heating has been predicted by runs of the codes ANTENA and GARFIELD, and are associated with absorption of a surface wave. The temperature profile measured on Scan #1 during heating via the West antenna rises steadily with radius, and may be due to a transmitter frequency closer to the local cyclotron frequency.

Temperature profiles taken with no ICRH in the center cell were almost flat. In addition, the temperature showed a rough correlation with both density and potential. The higher density shots had a lower temperature, while higher potential shots had a higher temperature. This behavior is assumed due to heating from ions moving radially in the potential gradient, and sharing that energy between a greater number of ions. This is demonstrated by the first two scans, during the time when

ICRH is not used. The density for Scan #1 (Fig. 7.6) peaks at $\simeq 2.7 \times 10^{12}$ cm, while the density for Scan #2 (Fig. 7.7) peaks at $\simeq 1.6 \times 10^{12}$ cm. The plasma potential in the first case (Fig. 7.11) is a nearly uniform 150-200 volts, while in the lower density case (Fig. 7.12), the potential rises to over 700 volts, and is sharply peaked on-axis. The ion temperatures for the two cases follows the potential. For the times without ICRH, the temperature profile for Scan #1 (Fig. 7.1) is a flat 20-40 eV, while for Scan #2 (Fig. 7.2), the temperature rises from 40 eV near the axis, to near 70 eV at a 15 cm radius before dropping the edge. The off-axis peak supports the hypothesis of ion heating by the potential, as the potential gradient is largest off-axis.

The density profiles measured are generally far from the Gaussian shape used to convert the line-density measured by the microwave interferometer, to on-axis density. As shown in Section 6.3, however, the line densities indicated by these profiles are within 20% of the microwave interferometer measurement. The density was generally lower without ICRH, but not more than 25%. This is also noted by the microwave interferometer system.

All of the scans have some shot-to-shot variations that obscure the profile shape somewhat, but the general shape is assumed to hold true. The profiles to be used in the power balance in Chapter 8 are all fit to radially stepped curves. The value for each step being the average of the data points within each radial shell. The radii chosen for the step boundaries are those used by the PPC plates and Faraday cups diagnostics to report the end-loss currents.

Chapter 8

Power Balance

The goal of this dissertation, as stated previously, is to experimentally measure the radial power deposition profile of ion cyclotron resonance heating in the central cell of TMX-U. However, the radial profile of ion heating is not directly measurable by available means, so an indirect method had to be employed. Conservation of energy is used to set the power input to the ions equal to the sum of all the power loss mechanisms for ions in the center cell. These losses can be measured more easily. The input power to the ions as a function of radius is calculated both with and without ICRH, and the profiles subtracted, to remove the contributions of ECRH and neutral beam heating in the plugs. The following sections describe the individual loss mechanisms, and the equations used to model them. The REA provides the radial profiles of ion temperature, density, and potential that make this undertaking possible.

8.1 Description of Power Loss Mechanisms

The power absorbed from the ICRH system is equated to the sum of five terms, each describing a major power-loss mechanism for the central cell ions. In each term, the loss of ions is expressed as a current density, j, yielding power densities, in watts per square centimeter. The plasma profile is broken up into 6 radial shells, with parameters assumed constant across each one. The shell boundaries are at

2.9, 5.3, 9.3, 13.4, 17.7, and 22.4 cm. These correspond to the radii at which the integrated Faraday cup data are reported by the main TMX-U computer. The power-loss channels included in the power balance are: charge exchange, end losses, electron drag, radial ion transport, and excitation losses. These mechanisms are discussed in the following sections.

1) *charge exchange*

Cold gas is supplied to the center cell of TMX-U to fuel the plasma via ionization. However, other molecular processes occurring in addition to ionization are not all as beneficial. One of the largest energy loss channels for the center-cell ions is the process of charge exchange. In this process, a cold, neutral atom, unaffected by the confining magnetic field, travels into the plasma and collides with an ion. The ion captures the electron from the atom, becomes a neutral atom itself, crosses the field and is lost. The newly-formed cold ion is confined, but has only a small fraction of the original ion's energy. Charge exchange, therefore, is only an energy loss. There is no net loss of ions. Charge exchange also occurs off molecular deuterium, but in the range of ion energies encountered in TMX-U, the reaction rate[55] for molecules is 1 to 2 orders-of-magnitude smaller than for atoms, and will be neglected for this calculation.

The power lost to charge exchange is obtained by multiplying the current of ions lost to charge-exchange, times their average energy. The average energy of an ion lost to charge exchange is 3/2 times the local ion temperature, measured directly by the REA. Measuring the charge-exchange current is not as straightforward. The process of charge exchange does not emit any observable radiation, but the process of excitation of atomic deuterium does. Electrons that are knocked to higher-energy states can return to a lower-energy state via photon emission. This

T_i (eV)	$< \sigma v >_{cx}$ ($\times 10^{-8}$ cm^3 sec^{-1})	T_e (eV)	$< \sigma v >_{ion}$ ($\times 10^{-8}$ cm^3 sec^{-1})
10	1.71	10	0.6
20	2.15	20	1.5
30	2.45		
40	2.70	40	2.2
50	2.91		
75	3.33		
100	3.66		
125	3.94		
150	4.18		
175	4.40		

Table 8.1: Charge Exchange and Ionization Crossections Used in C-X Loss Calculation

light is measured by the H_α system and the ionization rate inferred from the ratio of cross sections, as described in Section 2.4.3. The charge exchange current is calculated from the ionization rate, and the ratio of ionization to charge-exchange cross sections. The charge-exchange cross section depends on the ion temperature, while the ionization cross section depends predominantly on the electron temperature. The ratio of charge-exchange to ionization rates, $\mathcal{R}_{cx}$, ranges from 0.9 to 2.5 for the conditions of this experiment. The cross sections for charge exchange and ionization are listed in Table 8.1[55]. The electron temperature is measured on-axis by Thompson scattering and at the edge by a Langmuir probe. For the shots in Scans #4 and #5, the on-axis measurement averaged 40 eV. At the edge, the electron temperature is generally measured to be in the 20-25 eV range. The

radial profile of ion temperature measured by the REA is used to find the proper charge exchange cross section. The electron temperature profile is assumed to be a constant 40 eV out to 9.3 cm, and then 20 eV from 9.3 cm out to the edge of the plasma. These temperatures are used to look up the ionization cross section. Contributions of $D_2+e^- \rightarrow D+D+e^-$, $D_2+e^- \rightarrow D_2^+ + 2e^-$, and $D^0+e^- \rightarrow D^+ + 2e^-$, reactions are included in the values given in the table. The power lost in charge exchange is given by:

$$P_{cx} = j_{cx} \cdot \bar{E}_{ion} = j_{cx} \cdot \frac{3}{2} \cdot T_{REA}$$

where:

$$j_{cx} \cong \mathcal{R}_{cx} \cdot j_{ionize}$$

2) *end-losses*

Ions that escape to the end wall carry both their thermal energy and the energy gained from the potential difference between the center cell and the end wall. The temperature of ions escaping off-axis is not measured, and must by inferred from the temperature measurements made by the REA in the center cell. The ratio between the perpendicular and parallel temperatures is not a constant, rather, it varies with the collisionality and confinement time of the ions. The ratio of end-loss temperature to central-cell temperature was measured directly on TMX-U by the REA and the ELIS when the two diagnostics were positioned at the same radius in the plasma. This ratio ranged from unity for temperatures near 20 eV, to less than 0.4 for the higher central-cell temperatures. An empirical fit to the temperatures measured by the REA and ELIS was used in the calculation of the end-loss power. This factor, $\mathcal{F}_T$, is assumed to hold for off-axis measurements as well, and is used to model the off-axis end-loss ion temperature. Power is

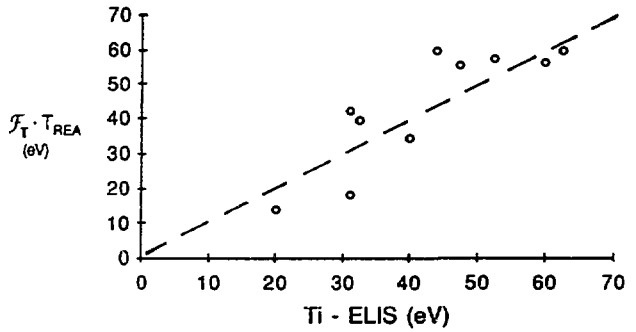

Figure 8.1: Plot of $\mathcal{F}_T \cdot T_{REA}$ vs. T_{ELIS}

calculated to be the ion current, as measured by the Faraday cup array, times the sum of end-loss temperature and central-cell potential, as measured by the REA:

$$P_{end-loss} = j_{FC} \cdot (e\Phi_{REA} + \mathcal{F}_T \cdot T_{REA})$$

where :

$$\mathcal{F}_T = \left(1 - \frac{T_{REA}}{240}\right)$$

A plot of $\mathcal{F}_T \cdot T_{REA}$ vs. T_{ELIS} is shown in Fig. 8.1. The data for this plot was taken when the REA was positioned near the axis.

3) *electron drag*

Power is also transferred from the ions to the electrons when the ion temperature is greater than the electron temperature. The electron temperature is taken to vary in a 2-step profile from the on-axis value of 40 eV, given by Thompson scattering, to the edge value of 20 eV, given by the Langmuir probe. This is the same profile described in the charge exchange section above. The ion temperature and density

is measured by the REA. The classical electron drag formula[5] is used to calculate the power lost by the ions:

$$\begin{aligned} P_{drag} &= \frac{\frac{3}{2} q \cdot n_c^2 (T_i - T_e)\, L_c}{4.8 \times 10^7 \cdot T_e^{1.5}} \\ &= 2.5 \cdot (n_{12})^2 \left(\frac{T_i - T_e}{T_e^{1.5}} \right) \end{aligned}$$

In the above equation, a center-cell length of $L_c = 500$ cm is used, the density, n_{12} is expressed in units of 10^{12}cm^{-3}, and the temperatures are expressed in eV. This term can be a loss or gain of power for the ions depending on the magnitudes of ion and electron temperatures.

4) *radial losses*

The cross-field transport of ions leads to a radial power loss when these ions strike a limiter. The radial loss current is taken to be the difference between the ionization current measured by the H_α system and the end-loss current as measured by the Faraday cup array on the end wall. A correction factor to the H_α measurement of ionization rate at larger radii was used to account for the larger number of ionization events per photon emitted due to the presence of neutral deuterium molecules. Runs of the neutral-particle transport code, DEGAS,[56] indicate that 18 to 20 ionizations occur per photon emitted at the edge of gas-fueled plasmas such as TMX-U. The cold deuterium molecules are quickly disassociated by the plasma, forming atoms with 2-4 eV of energy, which penetrate further into the plasma. Therefore, the core of the plasma is predominantly fueled by neutral atoms, and the ratio of 11.5 ionizations-per-photon used in the H_α data reduction is correct. To model this effect in a simple fashion, a correction factor, $\mathcal{F}_{D_2}$, is used to multiply the ionization current given by the H_α system. A factor of 1.75 is used for the outer-most radial shell, and a factor of 1.5 is used in the next.[57] The

factor $\mathcal{F}_{D_2}$ is set to one for the remaining four shells.

Ions that are lost radially take with them both their thermal energy and the potential at which they were ionized. Radial power losses are taken to be the product of the difference between the ionization and end-loss currents, and the sum of potential and ion temperature measured by the REA:

$$P_{radial} = (\mathcal{F}_{D_2} \cdot j_{ionize} - j_{FC}) \cdot (\Phi_{REA} + T_{REA})$$

5) *excitation loss*

The last term in the power balance models the energy expended to ionize the fueling gas. For every ionizing event, there are also competing processes. The contribution of all these processes are assumed to take 30 eV per ionization.[58] The power lost to excitation is calculated as the product of the ionization current and the 30 eV per ion:

$$P_{ex} \cong \mathcal{F}_{D_2} \cdot j_{ionize} \cdot (30\,\mathrm{eV})$$

This power is mainly expended by the electrons in the plasma, but is included in the ion power balance to model the effects of the change in ionization profile during ICRH. Since ICRH is the only heating source added, any additional power expended to ionize the fueling gas is attributed to electron drag on the heated ions. This effect is handled in this manner because the electron temperature as a function of radius and time during the shot is not available. This change in ionization is clearly seen in Fig. 2.6.

8.2 Radial Profile of ICRH

The above five terms are added to give the total power loss rate for ions in the center cell. This is equated to the total power input to the ions:

$$P_{input} = P_{cx} + P_{end-loss} + P_{drag} + P_{radial} + P_{ex}$$

The power balance was calculated for three times during the shots: once during operation of the West ICRH system, again when the East ICRH system was on, and again when neither were operating. During the times when there was no RF heating in the center cell, the only power sources active in the machine were ECRH and neutral beam injection in the plugs. These sources were held constant as the RF power was turned on and off in the center cell and were assumed to provide the same power to the center-cell ions independent of ICRH. The timing of the fueling and power systems used during these series of shots (scans #4 and #5) is shown in Tables 7.1 and 7.2.

Figures 8.3 through 8.8 illustrate the relative contributions of the individual terms in the power balance for each of the three conditions, for the two scans For all of the conditions, the power lost to electron drag and excitation is only a small percentage of the total. During ICRH, the higher ion temperature makes charge exchange and radial losses predominate. The power lost with ions escaping out the ends of the machine does not increase as much because the end-loss ion temperature is much lower than the perpendicular ion temperature in the center cell. The radial losses are predominantly in the outer radial shells, with or without ICRH. The measurements, in fact, indicate the radial transport in the core region is less with ICRH than without. Although this result is opposite to observations made in other experiments, the reduction in this case can be explained as the contribution of two effects. First, resonant radial transport is driven by $\vec{E} \times \vec{B}$

rotation spoiling the cancellation of radial drifts in the quadrupole fields at each end of the central cell. Ions are heated by ICRH predominantly in the perpendicular direction, which causes them to be trapped closer to the midplane of the central cell. Near the midplane, the magnetic field is nearly axisymmetric, and resonant radial transport is greatly reduced. Second, collisions with neutral gas can also move ions out radially, in a random-walk fashion. During ICRH, the ionization rate in the plasma periphery is increased, shielding the core from the fueling gas. This lowers the core ionization rate, and the collisional transport as well.

This can be best illustrated by comparing the ionization current to the sum of axial loss currents and dn/dt currents. The difference between the two currents is the current lost radially. Figure 8.2 shows the core ionization (out to 10 cm in radius) and the sum of axial and dn/dt terms as a function of time for Shot 30 on 9/30/86, which is typical for shots in this series of experiments. The ionization current is higher than the sum of axial and density change terms, indicating a substantial radial loss current, except when ICRH is operating. During these times, 21-34 msec and 42-55 msec, the ionization current is nearly equal to the sum of axial and dn/dt currents, indicating minimal radial transport.

In each of figures 8.3 through 8.8, the top envelope of the columns is the total power deposition profile as a function of radius. The radial profile of ICRH is calculated by subtracting the power deposition profile without ICRH from the power deposition profile calculated during ICRH. The profile was calculated for each antenna, for Scans #4 and #5. The resultant radial profiles are given in Figures 8.9 through 8.12. The profiles for the West antenna (Figs. 8.10 and 8.12), indicate a power deposition profile peaked of-axis in both cases, while the profiles for the East antenna indicate a fairly flat profile in the higher density case, and a steadily rising profile in the lower density case. These profiles will be compared to

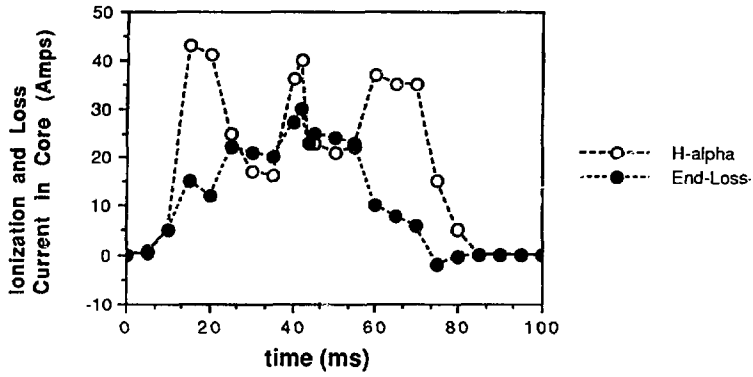

Figure 8.2: Comparison of ionization current to axial losses shows minimal radial transport during ICRH. The ionization current was measured by the H_α system, the axial losses by the Faraday cups, and the dn/dt term was calculated from the microwave interferometer data. The West ICRH system was on from 21 to 34 msec, the East from 42 to 55 msec.

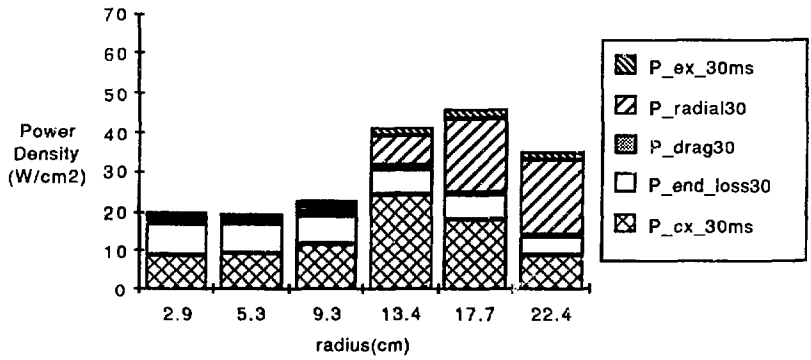

Figure 8.3: Radial Profile of Power Loss Terms for the West Antenna, for Scan Number 4

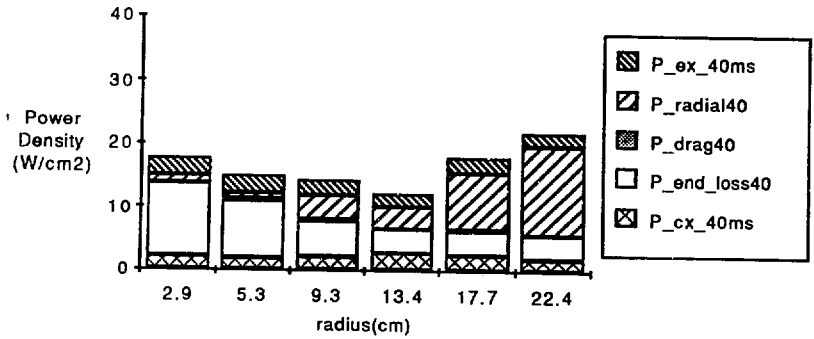

Figure 8.4: Radial Profile of Power Loss Terms with no ICRH, for Scan #4

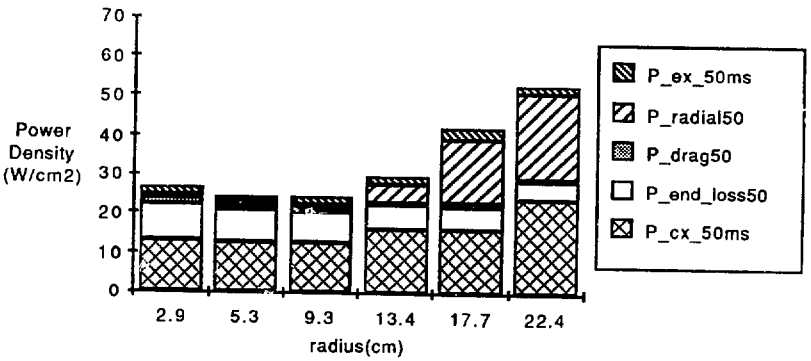

Figure 8.5: Radial Profile of Power Loss Terms for the East Antenna, for Scan Number 4

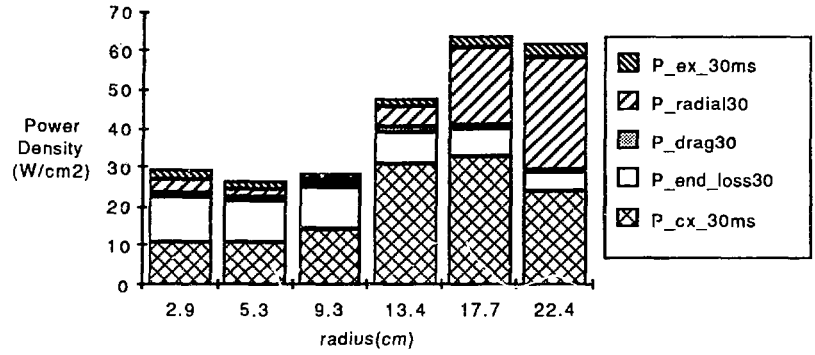

Figure 8.6: Radial Profile of Power Loss Terms for the West Antenna, for Scan Number 5

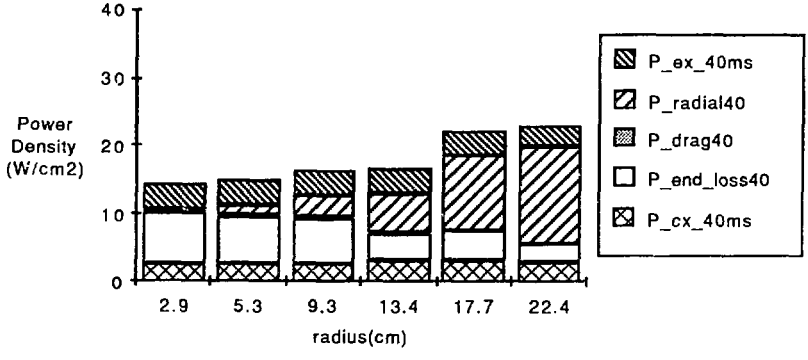

Figure 8.7: Radial Profile of Power Loss Terms with no ICRH, for Scan #5

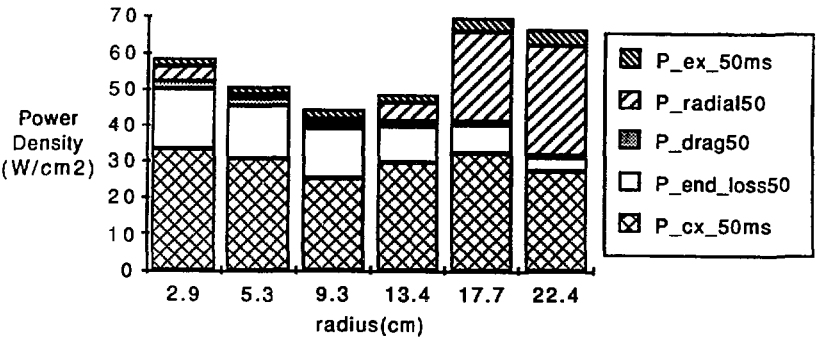

Figure 8.8: Radial Profile of Power Loss Terms for the East Antenna, for Scan Number 5

code predictions in Section 8.4.

The calculated power deposition was compared to the power required to heat the current of ionized deuterium to the bulk ion temperature as an order-of-magnitude check on the power balance method. For Scan #4, during West ICRH operation, the ionization rate in the core was $\simeq$50 mA/cm^2, with an ion temperature of $\simeq$80 eV. This gives a power requirement of $\simeq$4 watt/cm^2 in the core. The power calculated on axis for this case is 0.2 watt/cm^2. Since the power delivered by the RF is calculated as the difference of numbers on the order of 20, an error of $\pm$10% could easily account for the disparity.

8.3 ICRH efficiency

As a check on the above power balance, the total power to the plasma was calculated and compared to the broadcast power. The broadcast power is calculated

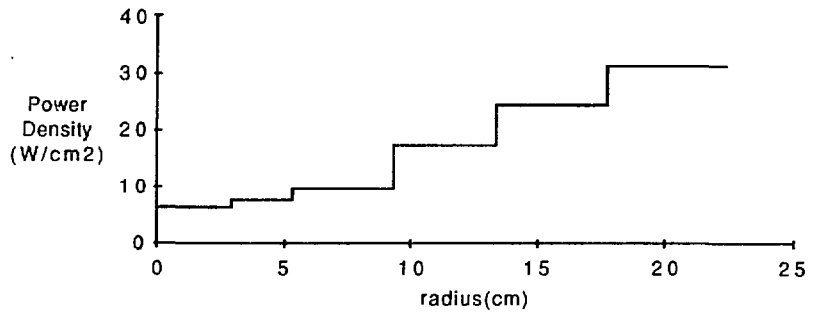

Figure 8.9: Radial Profile of ICRH for the East Antenna, Scan Number 4

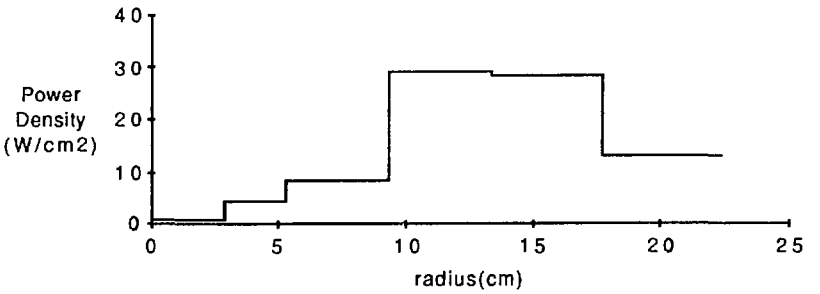

Figure 8.10: Radial Profile of ICRH for the West Antenna, Scan Number 4

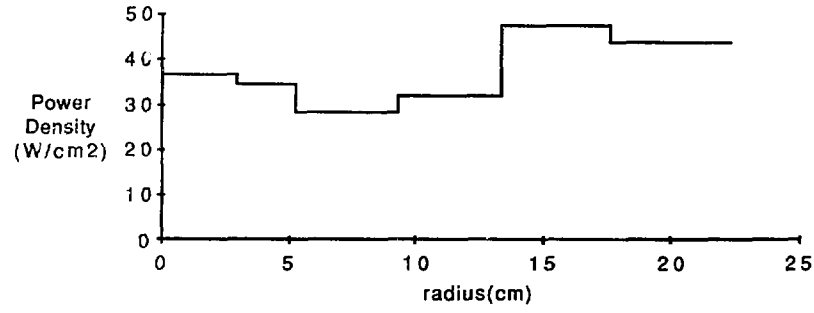

Figure 8.11: Radial Profile of ICRH for the East Antenna, Scan Number 5

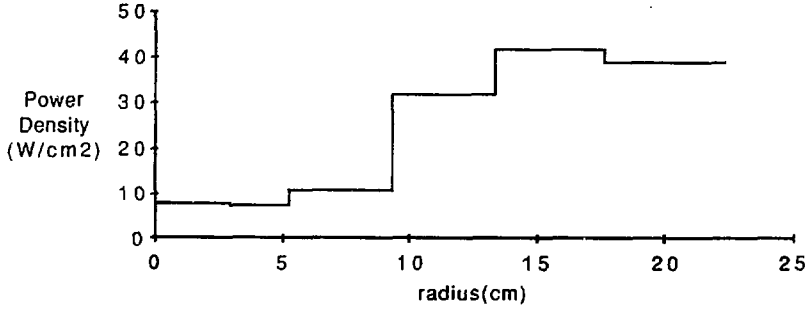

Figure 8.12: Radial Profile of ICRH for the West Antenna, Scan Number 5

	Scan	East ICRH	West ICRH
Broadcast Power	4	33 kW	40 kW
Calculated Power	4	35.5 kW	29.3 kW
Percent Accounted	4	108%	73%
Broadcast Power	5	65 kW	67 kW
Calculated Power	5	62.4 kW	51.4 kW
Percent Accounted	5	96%	77%

Table 8.2: Comparison of Broadcast and Calculated ICRH Powers

from the measured forward and reflected power on the line feeding the matching network, the antenna internal resistance, and the plasma loading resistance. The net power broadcast from the antenna is therefore given by:

$$P_{net} = (P_{forward} - P_{reflected}) \cdot \left(\frac{\mathcal{R}_{plasma}}{\mathcal{R}_{plasma} + \mathcal{R}_{antenna}} \right) \tag{8.1}$$

where the $\mathcal{R}$'s are the respective resistances. The total calculated power is taken to be the calculated power densities multiplied by the respective ring areas and summed. The comparison between these two results is summarized in Table 8.2. The power balance accounts for 73% of the power broadcast from the West antenna system, and 108% of the power from the East system for Scan #4, and 77% and 96% respectively for Scan #5. The accountability of the power from the West antenna is well within the uncertainty of the power calculation, when one considers the number of measurements and assumptions involved. The accuracy of each of the measurements that enter into the power balance is ± 10 to 15%, and most terms involve the product of two measurements, giving an expected variation of ± 20 to 32%. The power calculated for the East antenna also reflects these same considerations. Although much effort was expended to keep all of the shots for

a given condition identical, there could have been some uncontrollable, and/or unmeasured variations between shots that contributed to this discrepancy. Also, the radial integral only extends to 22.4 cm, while the plasma limiter in located at 24 cm in the center cell. Some additional power could be lost in this low density region.

The validity of the shape of the power deposition profile is supported by the fact that the total power calculated is within 25% of the broadcast power (which is only known to within ±10%), and the calculated stored-energy is within 10 to 32% of that measured by the DML, depending on the assumptions made (see Section 6.4). However, as stated earlier, the radial profile of ICRH is the key issue, not the total power absorbed. The radial profiles will be compared to code predictions in the following section.

8.4 Heating profiles from ANTENA and GARFIELD codes

In order to be a useful power source for plasma heating, ICRH must be predictable in its effect. There are two accepted methods of predicting the outcome of a given experiment, theoretical understanding, and empirical scaling laws. Two codes are in use to model ICRH in mirror-like configurations, ANTENA[42] and GARFIELD,[43] which are described in Section 3.2. As with all theoretical models, there are many assumptions and simplifications made in these codes to make the problem mathematically tractable. Both codes use a simplified plasma model, assume azimuthal symmetry, as well as other approximations to the actual experimental situation. The effect of these simplifications on the solution is unknown, only by comparing the codes to experiment can the code be validated. It is the stated goal of this

dissertation to provide that comparison. However, there are assumptions made in the interpretation of the experimental data as well. Considering all of the above, the overall shape of the predicted profiles and the experimental profiles will be compared, not the actual magnitudes.

The experimental power deposition profiles show a qualitative difference between the different antenna systems. The difference in profiles between the two density cases is not as great, for either antenna. Functionally, there are few physical differences between the two antennas. Apart from the difference in axial position of the antennas, the major difference is in the antenna elements themselves. The East antenna is a single strap, while the West is a 3-1/2 turn coil. The effect of these differences, however, is not easily modeled by the codes. Rather than attempt a detailed study involving variation of dozens of input parameters, the codes were run with input parameters closest to the experimental conditions, with only small variations from that point made.

Runs of the ANTENA code quickly showed the limitations of its power absorption model. The code models only an axially uniform magnetic field, and as such, cannot correctly model the antenna coupling and the cyclotron resonance at the same time. Previous experience on TMX-U[35,59] has shown that setting the magnetic field in the code equal to the local TMX-U field under the antenna yields the correct plasma loading resistance. However, the driving frequency is below the cyclotron frequency so the waves do not experience cyclotron damping. If the magnetic field strength and frequency are set so the antenna is driven at the cyclotron frequency, the coupling is incorrect, the field profiles are changed, and the power absorption is still incorrect. A compromise is to run the code with the magnetic field set to the local value, to get the coupling correct, and to vary the collision frequency of the ions and electrons to artificially increase collisional damping of

the waves to simulate the cyclotron resonance. Unfortunately, varying the collision frequency changes the profile of power absorption as well. Two runs will illustrate this point (input files for the two cases are given in Appendix C). The first uses collision frequencies suitable for the measured experimental conditions, the second uses an ion collision frequency 10 times larger, and an electron collision frequency 10 times smaller. The radial profiles of E^+ for the two cases, shown in Fig.8.13a and 8.13b, indicate little difference in either the profile of E^+ for the two cases, but the magnitude has changed a factor of three. The radial profile of power absorption is changed markedly, but the peak value is nearly the same. The case using the experimental parameters (Fig.8.14a) shows strong peaking of the absorption on-axis, while the modified case (Fig.8.14b) shows nearly a flat profile. Variations in density and temperature did not affect the absorption profile to the extent the collision frequency did.

The general conclusions that can be made from these runs is that ANTENA cannot predict the radial profile of ICRH as it stands due to the lack of an axial magnetic field gradient. The power deposition profile is dependent on the collisionality of the plasma, and not cyclotron damping. Simply inputting the experimental conditions to the code yields, in this case, a much more peaked profile than observed.

The restriction of axial uniformity is removed in the GARFIELD code. However, it uses a cold-plasma dielectric tensor, and still cannot model the cyclotron resonance correctly. Instead, the cyclotron damping is approximated by adding a small damping term to $\overleftrightarrow{\varepsilon}$, as discussed in Section 8.4. This scheme succeeds in placing the absorption at the cyclotron resonance, but the radial profile is still dependent on the choice of the damping parameter. GARFIELD produces contour plots of the RF fields as a convenient way to get an overview of the field struc-

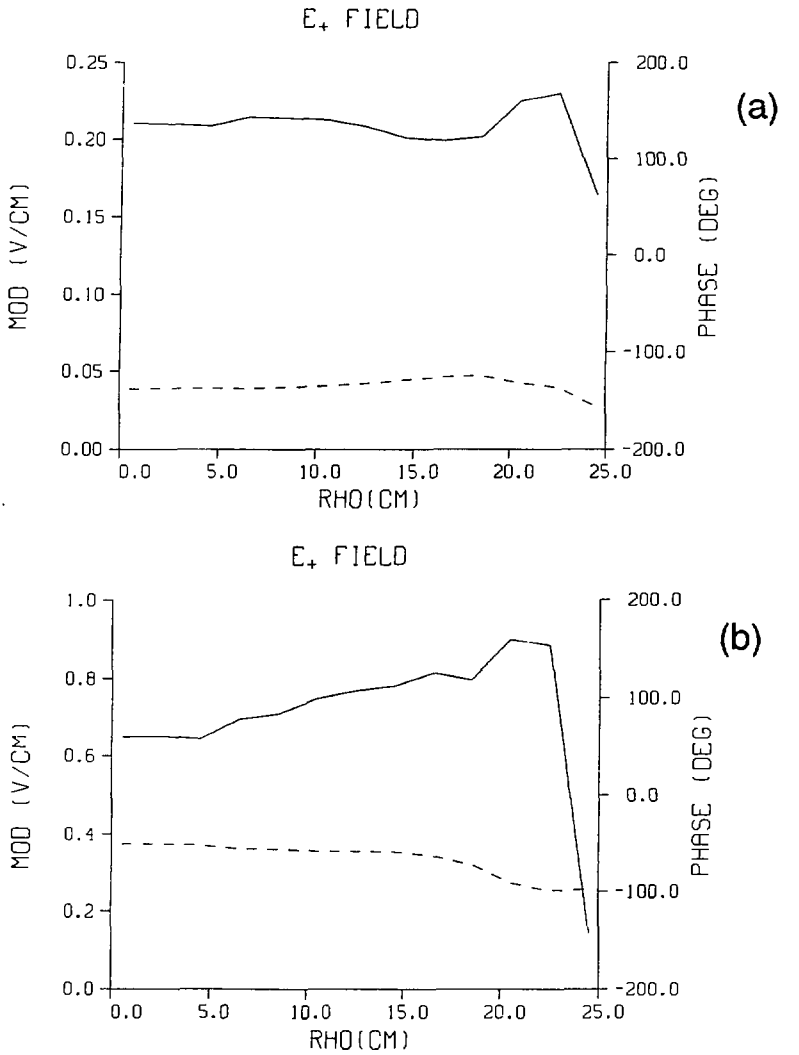

Figure 8.13: Radial Profiles of E^+ from ANTENA for (a) Experimental Conditions and (b) with Higher Ion Collisionality

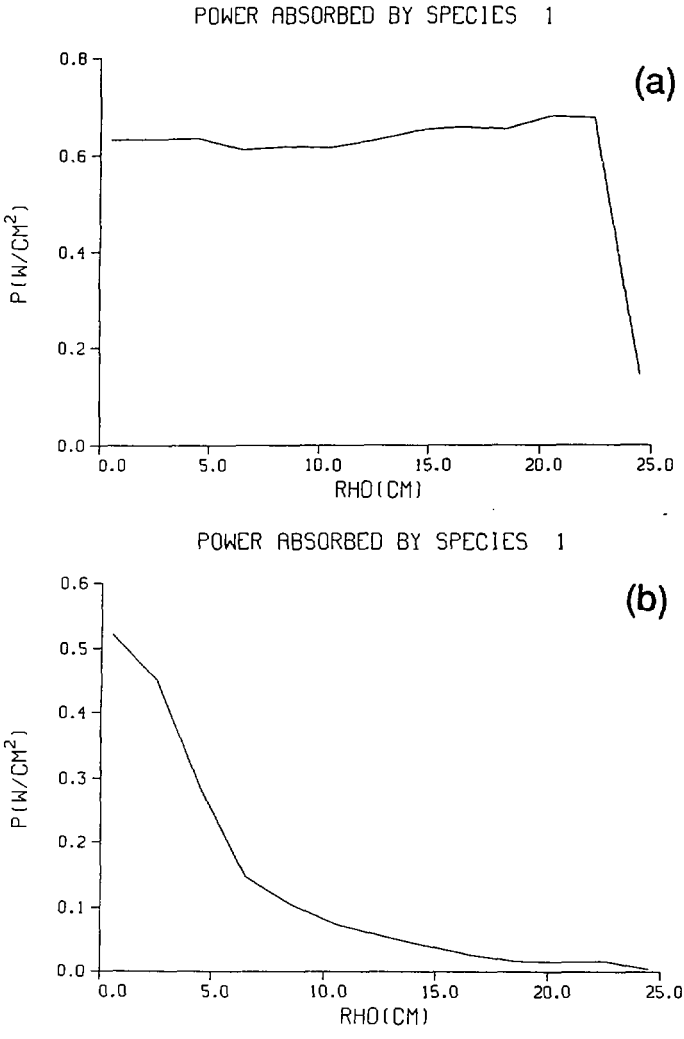

Figure 8.14: Radial Profiles of Absorbed Power from ANTENA for (a) Experimental Conditions and (b) with Higher Ion Collisionality

ture. Shown in Fig. 8.15a and 8.15b are plots of the magnitude of E^+ for (a) the experimental conditions, and again with (b) a collisionality parameter 10 times as large. The contours for the two cases look similar in structure at first. Both have strong fields around the antenna, and virtually no fields to the left of the resonance location. The case with heavier damping, however, has field strengths roughly half the other (note the values of the contours). The code as originally supplied, gave only a contour plot of the power absorption, which was difficult to interpret, so an axial-integral routine was written and incorporated into GARFIELD. The resultant radial profiles are given in Fig. 8.16. The two cases give similar radial profiles of absorption, with the lighter damping case yielding a broader peak. The profiles peak on-axis, at nearly the same value as well. The antennas, due to their configuration, launch wave predominantly in the m=$\pm$1 modes. The power absorbed in each of these modes is shown, along with their sum. Power is absorbed mainly at the plasma edge from the m=+1 mode, identifying this mode as the surface wave described by Paoloni,[60] although the majority of the power absorption is in the m=-1 mode, the slow wave.

The broad conclusions reached from running GARFIELD are similar to those obtained from the running of ANTENA. The radial profile of ICRH is dependent on parameters governing the collisional damping used to model cyclotron damping. These parameters may be manipulated to give a variety of radial profiles, which may or may not mimic reality. The experimentally measured profiles generally showed absorption increasing with radius, which was not indicated for these conditions by either of the codes. As they stand, neither code adequately models the absorption of RF waves in experimental plasma devices. The GARFIELD code is nearly able to provide a complete model, if it can incorporate a suitable cyclotron damping model. Until then, ICRH will continue to be guided by experimental

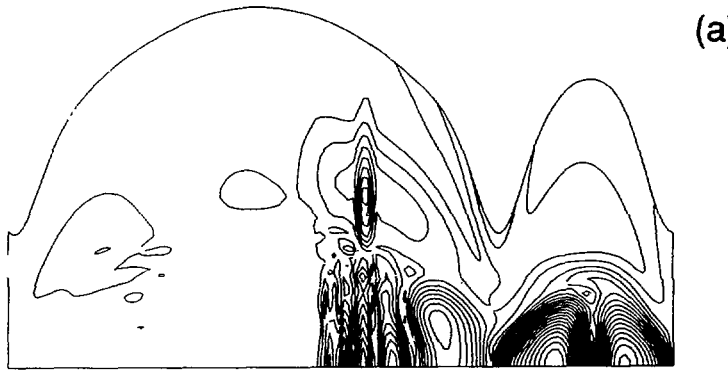

Values Plotted:

0.	0.18113e+01	0.36225e+01	0.54338e+01	0.72451e+01
0.90564e+01	0.10868e+02	0.12679e+02	0.14490e+02	0.16301e+02
0.18113e+02	0.19924e+02	0.21735e+02	0.23547e+02	0.25358e+02
0.27169e+02	0.28980e+02	0.30792e+02	0.32603e+02	0.34414e+02
0.36225e+02				

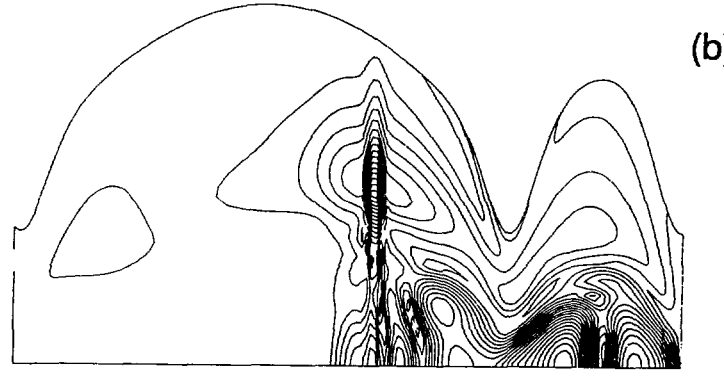

Values Plotted:

0.	0.77469e+00	0.15494e+01	0.23241e+01	0.30987e+01
0.38734e+01	0.46481e+01	0.54228e+01	0.61975e+01	0.69722e+01
0.77469e+01	0.85216e+01	0.92962e+01	0.10071e+02	0.10846e+02
0.11620e+02	0.12395e+02	0.13170e+02	0.13944e+02	0.14719e+02
0.15494e+02				

Figure 8.15: Contours of E^+ Generated by GARFIELD using (a) Experimental Conditions, and (b) with Enhanced Damping

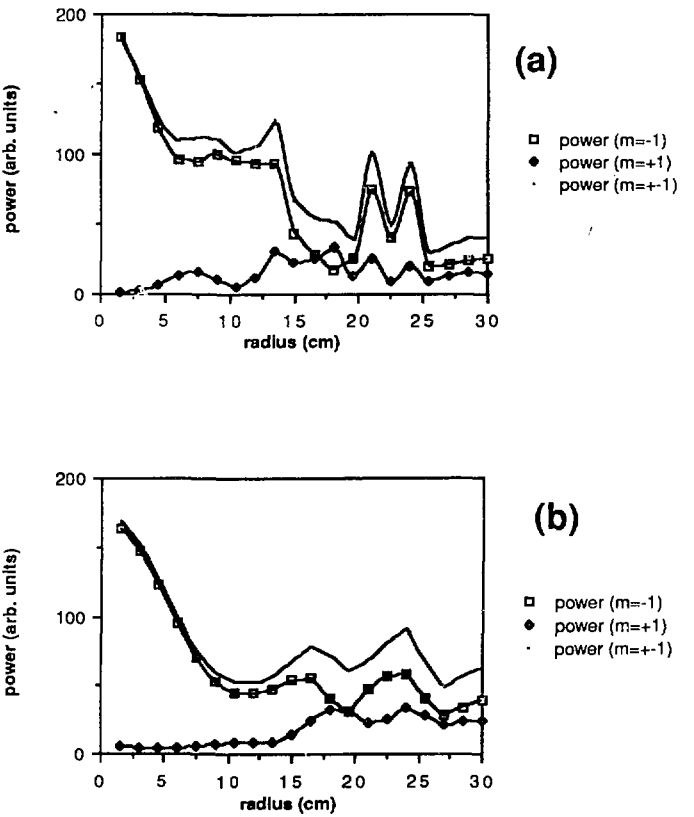

Figure 8.16: Radial Profiles of Absorbed Power from GARFIELD using (a) Experimental Conditions, and (b) with Enhanced Damping

experience.

Chapter 9

Summary

The REA has been successfully used to measure the profiles of ion temperature, density, and plasma potential in the central cell of TMX-U. The REA measurements were compared to similar and supporting diagnostics and found to be within experimental uncertainties. The radial profile of ICRH power deposition was calculated from these, and compared to predictions of the RF modeling codes ANTENA and GARFIELD. Overall efficiencies of the ICRH systems were calculated to be greater than 70% using a simple power balance model. The REA system has provided some of the first information about the radial profiles of the TMX-U plasma characteristics.

9.1 Other Uses for the REA

The REA has been shown to be a reliable diagnostic of ion temperature in a regime where unshielded probes are dominated by electron physics. In addition to the measurement of ion temperature, density, and plasma potential, the REA can be used in other ways. The REA can measure ion density fluctuations directly, without the confusion of electron phenomena. The REA can also give a direct indication of the fraction of hot ions present in a neutral-beam heated plasma.

9.1.1 Characterization of Tokamak Edge Regions

The REA is a fairly rugged probe, and may have uses on other devices. Although the heat loading in tokamak plasmas is generally too great, the REA may be usable in scrape-off and diverter regions. In these edge regions, the electron temperature is generally in the 10-60 eV range,[61] too great to allow measurement of the ion temperature by Langmuir probes. (When the electron temperature is comparable to the ion temperature, ion flow to a bare, biased tip is governed by the ion sound speed, $\sqrt{T_e/m_i}$). The edge conditions in many present-day tokamaks are very close to those encountered in TMX-U,[61] but with generally stronger magnetic fields. The higher field strength, and the absence of ECRH-heated electrons will allow use of the probe with a smaller recession distance, and subsequently a larger acceptance angle. Measurement of the ion temperature and fluctuation level in the edge will aid in the understanding of important atomic physics processes taking place there.

9.1.2 Hot Ion Fraction

Measurements of the hot ion fraction during Neutral Beam heating in the central cell have been made under various plasma conditions. It was observed that a large decrease in the hot ion fraction (at the edge of the plasma) occurred when the ICRH was turned on in the middle of a shot. The loss has not been fully explained, but may be due to ICRH evolving gas from the walls, or setting up azimuthally asymmetric potentials that distort ion drift surfaces outward into limiters. In TMX-U, neither of these quantities were measured. The central cell has several *ion gauges* to measure the neutral gas pressure, and none showed increases during ICRH, but the central-cell is quite large, and localized sources could have gone undetected. There were no diagnostics available to measure azimuthal asymmetries in plasma potential.

9.1.3 Edge Fluctuations

With the sweep supply off, the current measured by the REA can be used to study the level of ion density and temperature fluctuations in the plasma. Since the probe measures only ion current, direct electron effects are muted. A Fourier transform of the current signal shows that the harmonic content changes with varying plasma conditions. At present, there is no coherent theory that explains the observed changes in frequencies (such as a change in $\vec{E} \times \vec{B}$ rotation due to changing plasma potential).

9.2 Conclusions

The REA has been successfully implemented on TMX-U and has measured radial profiles of ion temperature, density and plasma potential. Ion cyclotron resonance heating was found to heat the center-cell plasma from 20 eV to over 150 eV on axis, with $\simeq$60 kW of broadcast power, at an on-axis density of nearly 3×10^{12} cm^{-3}. The increase in ion temperature was seen across the plasma column, indicating the RF power was able to propagate radially.

The REA has allowed the first measurement of the radial power deposition profile of ICRH in the center cell of TMX-U. The power input to the ions was set equal to the sum of the power losses, divided into radial shells. The sum for each radius when no ICRH was on was subtracted from the similar sum when the ICRH system was operating. This was done to remove the contributions of the end-cell heating systems. The total absorbed-power calculated in this manner was greater than 70% of the broadcast power, indicating the power balance model used was reasonably accurate, and should produce a valid radial profile.

The radial profile measured was not as predicted by either of the modeling

codes, ANTENA or GARFIELD. Some profile differences were expected due to the shortcomings in the power absorption models in these codes, as well as geometrical differences between the plasma configuration assumed and the actual experimental configuration in TMX-U. Changes in the collisionality parameters input to the codes changed the profiles of both the resonant E^+ field, and the power absorption. Collisionality determines the RF damping in both codes, as neither can correctly model the cyclotron resonant wave damping in a magnetic beach configuration. However, ANTENA does yield plasma loading resistances in agreement with experimental measurements, and useful in ICRH system design.

The REA has proved a versatile and fairly straightforward diagnostic. Its small, but rugged construction allows it to be inserted into modest density plasmas without degradation of the plasma, or damage to the probe. The REA has furthered the understanding of ion cyclotron resonant heating on TMX-U, and can be used in future applications.

Appendix A

Modeling of Space Charge Effects

A.1 Introduction

Whenever there is a net charge in a region of space, the effect of that charge on potentials must be evaluated. Since the magnetic field of TMX-U excludes electrons from the interior of the REA, collected ions must travel in a region of net space charge. This positive charge increases the potential above its expected profile in vacuum. If the density of ions is great enough, the space potential can rise high enough to reduce the current flow. The theory of currents limited by space charge has long been known and has been experimentally verified.[21] For particles emitted at zero energy and accelerated to a plate a distance x away, held at potential V, the space-charge limited current density j is given by:

$$j = (\frac{2}{me})^{\frac{1}{2}} \frac{V^{\frac{3}{2}}}{9\pi x^2} \tag{A.1}$$

In this case, the current is limited by the space charge reducing the potential gradient at the emitting surface to zero, eliminating the force that accelerates ions away from the emitting surface. However, for a finite temperature Maxwellian distribution, particles leave the emitting surface with finite velocity and can overcome a small unfavorable potential gradient, unlike their zero energy counterparts. For warm a ion distribution accelerating to a negatively biased plate, the potential builds positive near the emitting surface, low velocity ions reflect which reduces

the current. Unfortunately, an exact, analytic solution for the space-charge limit for a finite temperature is mathematically intractable, so approximate or numerical methods must be employed. Langmuir[21] calculated the limit to first order in $\eta^{-\frac{1}{2}}$, where $\eta = \frac{eV}{kT}$, to be:

$$j = (\frac{2}{me})^{\frac{1}{2}} \frac{(V - V_m)^{\frac{3}{2}}}{9\pi(x - x_m)^2}(1 + \frac{2.66}{\sqrt{\eta}}) \tag{A.2}$$

where x_m is the position of potential extrema, V_m. In the operation of the REA, however, the collected current is not often limited by space charge, only reduced by it. The effects of un-neutralized charge need to be evaluated under a wide range of temperature, density, and bias voltage to cover the range of operation of the REA. To handle all the varying conditions analytically (even approximately) would have been an overwhelming task, so a code was written to model the effect.

A.2 Description of Code Model

The model used to calculate the effects of space charge on the REA currents is straightforward. The space between the two plates, held at fixed voltages, is divided into 25-150 gridpoints. The vacuum potential is then calculated for each gridpoint. A one-dimensional Maxwellian ion distribution is divided into energy bins, and the trajectory for each is followed through the grid. For each energy group, the sheet-charge density at each gridpoint is calculated using the velocity at each point and the continuity equation:

$$Q = en_i\Delta x = en_0\frac{v_0}{v_i}\Delta x \tag{A.3}$$

where n_0 and v_0 are the initial density and velocity and n_i and v_i are the density and velocity for each energy group at gridpoint "i" and Δx is the spacing between gridpoints.

The charge density for each energy bin is then summed to get the total charge density to be associated with each grid point. The potential profile for this charge distribution is then calculated. The ion trajectories are then re-calculated for the new potential profile, and the procedure is iterated until converged.

To ease the computational effort, the code is fully 1-D. A 2-D relaxation calculation of the vacuum potential inside the REA tip shows that the contours near the ion collector are nearly straight and evenly spaced, so the 1-D approximation should be reasonably accurate. Restricting the calculation to 1-D greatly simplifies the calculation of the potential profile from the charge density. Instead of a relaxation method, the analytic solution for an infinite charge sheet, and the superposition principle is used. The charge at each spatial bin is assumed to be concentrated in a sheet located at the gridpoint. The potential due to a sheet charge located between two grounded plates is given by (in MKS units):

$$\phi(x) = \frac{Q}{\epsilon_o} \frac{(x_{max} - MAX(x,x'))(MIN(x,x') - x_o)}{(x_{max} - x_o)} \qquad (A.4)$$

where: x_o is the position of the first plate (taken to be zero without loss of generality), x_{max} is the position of the second plate, x' is the location of the charge sheet, and Q is the surface charge on the sheet. The potential for a unit charge density is calculated at each gridpoint and stored in matrix form. This only needs to be calculated once for a given grid size, and is arranged so a standard matrix multiplication with the charge density (stored as a vector) yields the potential due to space charge everywhere between the plates in one operation. This potential is then added to the vacuum potential profile to get the total potential profile.

A.3 Verification of the Code

The code was benchmarked against the Langmuir formula for space-charge limited flow of deuterium ions at low temperature. The code cannot model a zero temperature for the emitted ions, so 2 eV was chosen. The ions accelerate to a plate biased to -100 volts, 0.1 cm away. Under these conditions, the code gives a space-charge limit 92% of that given by Eq. A.2. Plate bias and spacing were varied and the code gave the same current as the Langmuir formula within 2 to 10%.

A.4 Modeling of the REA Current Traces

The operation of the REA was modeled, for a given temperature and density, by stepping the potential of the collecting plate plus and minus a few times the ion temperature and calculating the equilibrium current to the plate. The ions all start at the zero potential plate. The equilibrium potential profile for an ion temperature of 50 eV and a density of 2×10^{12} cm^{-3} and -50 volts on the collector is shown in Fig. A.1. The potential increase is greater at the lower temperatures and higher densities, as shown in Figures A.2 through A.4. In each of these figures, the voltage increase is measured from the higher of the voltages on the two plates, and normalized to the ion temperature. The left plate is held at zero, while the right plate is varied negative and positive in voltage. Taking the negative exponential of this voltage ratio, ΔV_* gives the reduction from the expected collector current due to space charge effects:

$$I_{collected} = I_{random}\, e^{-MAX(V_1,V_2)/kT}\, e^{-\Delta V_*}$$

The result of a calculated sweep compared to REA data for the same conditions is shown in Figure A.5. The rounding of the curve near V=0 is due to the potential

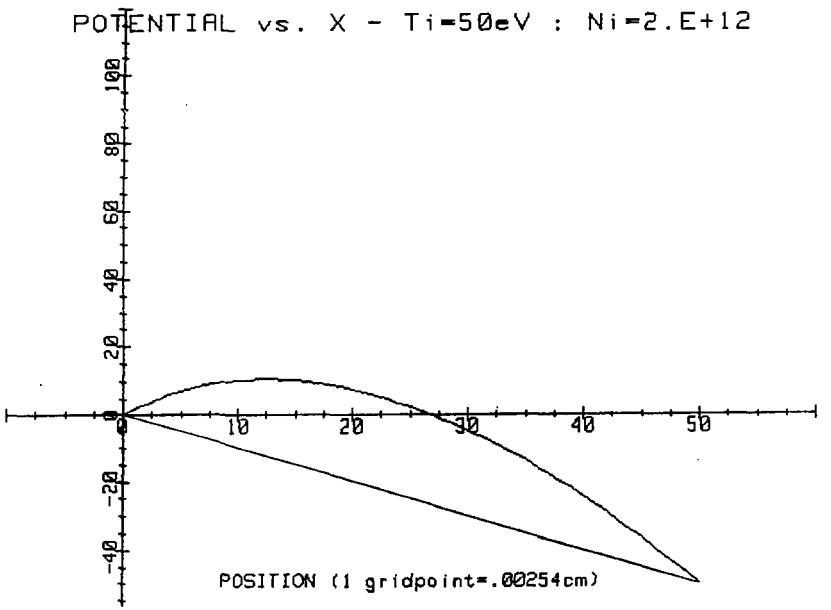

Figure A.1: Potential modification due to space charge. The straight line is the vacuum potential profile, net space charge increases the potential between the plates.

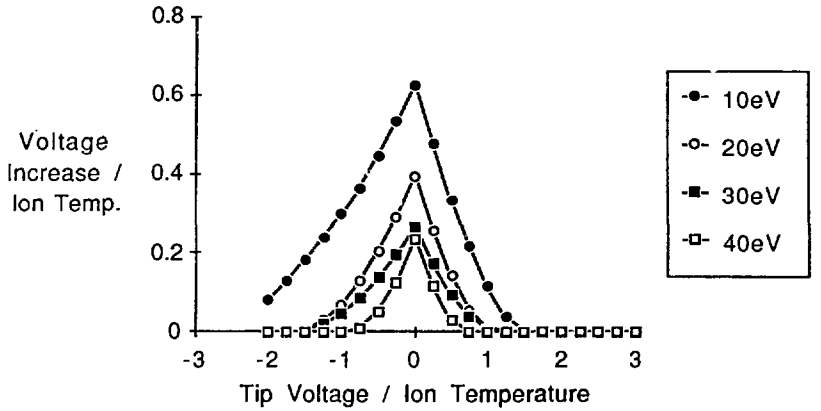

Figure A.2: Space-charge effect at $n_i = 0.5 \times 10^{12} cm^{-3}$.

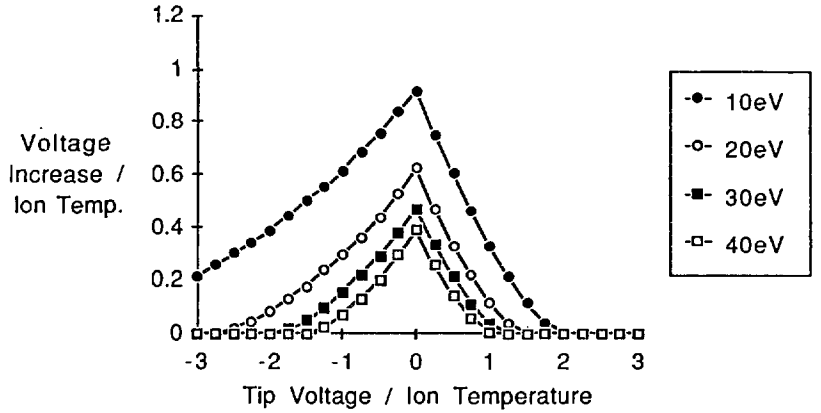

Figure A.3: Space-charge effect at $n_i = 1.0 \times 10^{12} cm^{-3}$.

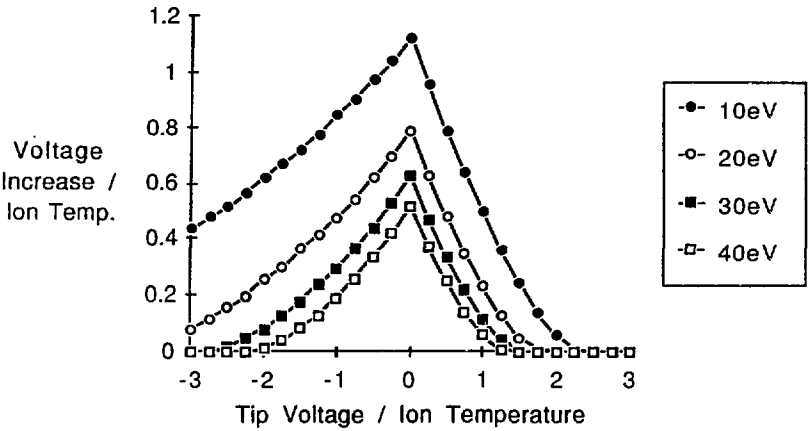

Figure A.4: Space-charge effect at $n_i = 1.5 \times 10^{12} cm^{-3}$.

in the gap rising above the plate voltage due to space charge. The code predicts a greater reduction in current than was observed in the experiment for the same conditions. This is likely an artifact of the 1-D approximation. In 1-D, an ion with insufficient energy to reach the biased collector slows to a complete stop and then retraces its trajectory. This results in an artificially high density near the turning point. In the actual experiment, these ions are deflected to the side as they slow their forward progress, giving a smaller density increase than the code would predict. The code is therefore overestimates the effect of space charge on the collected current, but is nonetheless useful is predicting a conservative range of operating parameters for the REA, or other similar instruments.

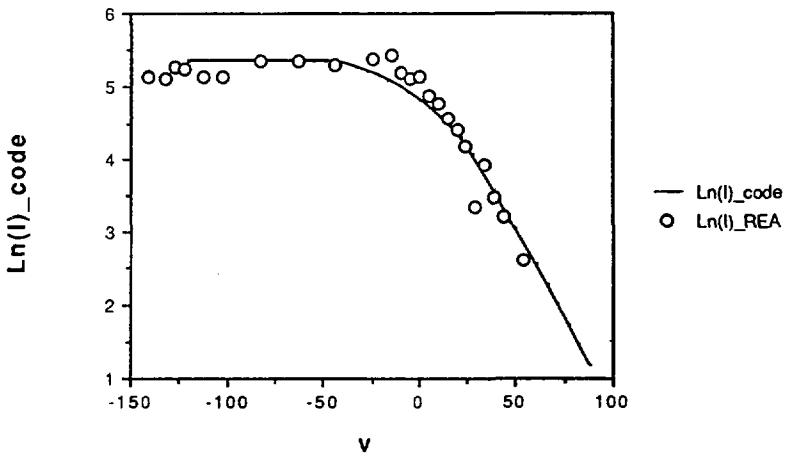

Figure A.5: An REA sweep simulated by the 1-D space-charge code compared to REA data. The ion temperature is 22 eV and the density is 0.8×10^{12} cm^{-3} in both cases. The solid line is the code result and the circles are the REA data points.

Appendix B

Tables of Values Used in the Power Balance

The plots in Chapter 8 were generated using the spreadsheet program, EXCEL, by Microsoft, and an Apple Macintosh computer and Laserwriter. A copy of the spreadsheet is provided here to show the exact values that went into producing the plots. The labels are mostly similar to those used in the text, with the 30, 40, and 50's referring to the time during the shot, in milliseconds. These times correspond to the West ICRH on, neither on, and the East ICRH on, respectively.

	A	B	C	D	E	F	G	H	I	J
1	REA9/30_a	Ti_30ms	Ti_40ms	Ti_50ms	Phi_30ms	Phi_40ms	Phi_50ms	Ni_30ms	Ni_40ms	Ni_50ms
2	r_2.9cm	77	16	96	80	105	73	1.6	1.72	1.78
3	r_5.3cm	84	16	97	87	95	73	1.6	1.65	1.78
4	r_9.3cm	94	17	92	92	85	80	1.63	1.25	1.73
5	r_13.4cm	100	19	72	110	80	87	1.75	0.65	1.53
6	r_17.7cm	68	17	60	140	100	120	1.6	0.4	0.95
7	r_22.4cm	51	16	96	180	145	135	0.5	0.5	0.4
8										
9	REA_hi_dens	Ti_30ms	Ti_40ms	Ti_50ms	Phi_30ms	Phi_40ms	Phi_50ms	Ni_30ms	Ni_40ms	Ni_50ms
10	r_2.9cm.	72	16	153	71	45	112	2	2.5	2.7
11	r_5.3cm.	74	16	145	75	50	113	2.1	2.5	2.75
12	r_9.3cm.	92	17	125	85	57	114	2	2.45	3
13	r_13.4cm.	112	15	112	90	62	114	2.1	2.1	2.8
14	r_17.7cm.	92	14	80	100	67	109	1.8	1.4	2.2
15	r_22.4cm.	68	15	60	111	74	71	0.7	0.8	1.1
16										

	K	L	M	N	O	P	Q	R	S	T
1	Te	cx_ion_30ms	cx_ion_40ms	cx_ion_50ms	H_a_30ms	H_a_40ms	H_a_50ms	F.C._30ms	F.C._40ms	F.C._50ms
2	40	1.53	0.91	1.64	0.0505	0.096	0.0567	0.061	0.0971	0.07
3	40	1.57	0.91	1.65	0.0484	0.0852	0.0527	0.0542	0.0852	0.0627
4	40	1.63	0.92	1.62	0.0509	0.0874	0.0572	0.0482	0.0592	0.0573
5	20	2.44	1.41	2.19	0.0666	0.0686	0.0679	0.0368	0.0394	0.0455
6	20	2.15	1.36	2.06	0.0822	0.0747	0.0868	0.0328	0.0336	0.0368
7	20	1.94	1.33	2.41	0.0598	0.0632	0.0685	0.0224	0.023	0.0262
8										
9	Te	cx_ion_30ms	cx_ion_40ms	cx_ion_50ms	H_a_30ms	H_a_40ms	H_a_50ms	F.C._30ms	F.C._40ms	F.C._50ms
10	40	1.49	0.91	1.91	0.067	0.12	0.077	0.0985	0.128	0.0995
11	40	1.5	0.91	1.88	0.065	0.12	0.076	0.08596	0.1087	0.0865
12	40	1.62	0.92	1.79	0.064	0.121	0.076	0.0745	0.0919	0.0786
13	20	2.53	1.3	2.53	0.073	0.114	0.071	0.0544	0.0522	0.0553
14	20	2.37	1.27	2.26	0.1	0.125	0.12	0.0456	0.0543	0.0482
15	20	2.15	1.3	2.06	0.11	0.107	0.15	0.0312	0.0299	0.0317
16										

	U	V	W	X	Y	Z	AA	AB	AC	AD
1	PPC_30ms	PPC_40ms	PPC_50ms		P_cx_30ms		P_cx_40ms		P_cx_50ms	Temp_frac_30
2	-0.8	-1.43	-1.33	2.9	8.9241075	2.9	2.09664	2.9	13.390272	0.67916667
3	-6.1	-11.3	-12.9	5.3	9.574488	5.3	1.860768	5.3	12.6519525	0.65
4	-1.04	-0.79	-1.99	9.3	11.698347	9.3	2.050404	9.3	12.787632	0.60833333
5	-6.9	-9.3	-11.6	13.4	24.3756	13.4	2.756691	13.4	16.059708	0.58333333
6	-2	-2.6	-1.5	17.7	18.02646	17.7	2.590596	17.7	16.09272	0.71666667
7	-16.7	-14.5	-15.2	22.4	8.874918	22.4	2.017344	22.4	23.77224	0.7875
8										
9	PPC_30ms	PPC_40ms	PPC_50ms		P_cx_30ms		P_cx_40ms		P_cx_50ms	Temp_frac_30
10	-0.9	-2.4	-1.7	2.9	10.78164	2.9	2.6208	2.9	33.752565	0.7
11	-8	-13.2	-7.1	5.3	10.8225	5.3	2.6208	5.3	31.0764	0.69166667
12	-1.44	-3	-4.8	9.3	14.30784	9.3	2.83866	9.3	25.5075	0.61666667
13	-6.9	-9.8	-12	13.4	31.02792	13.4	3.3345	13.4	30.17784	0.53333333
14	-1.4	0.92	-3.9	17.7	32.706	17.7	3.33375	17.7	32.544	0.61666667
15	-25.5	-17.8	-19.3	22.4	24.123	22.4	3.12975	22.4	27.81	0.71666667
16										

	AE	AF	AG	AH	AI	AJ	AK	AL	AM	AN
1	Temp_frac_40	Temp_frac_50	P_end_loss30	P_end_loss40	P_end_loss50	P_drag30	P_drag40	P_drag50	P_radial30	P_radial40
2	0.93333333	0.6	8.07004583	11.6455267	9.142	0.23843574	0.04682011	0.3142629	-0.85565	1.0285
3	0.93333333	0.59583333	7.67472	9.36632	8.20089875	0.26057168	0.04608227	0.31759831	-0.16416	0.94572
4	0.92916667	0.61666667	7.19063667	5.96711333	7.83482	0.2948253	0.04402259	0.29682912	1.44894	3.76788
5	0.92083333	0.7	6.19466667	3.84133583	6.2517	0.32493133	0.03698561	0.21791644	7.6566	3.56994
6	0.92916667	0.75	6.19045333	3.89074	6.072	0.20997524	0.0262469	0.14388705	18.824	9.17865
7	0.93333333	0.6	4.93164	3.67846667	5.04612	0.08927223	0.02740039	0.15115687	18.99975	14.1036
8										
9	Temp_frac_40	Temp_frac_50	P_end_loss30	P_end_loss40	P_end_loss50	P_drag30	P_drag40	P_drag50	P_radial30	P_radial40
10	0.93333333	0.3625	11.9579	7.67146667	16.6625188	0.24748737	0.05336344	0.61742025	-3.5464	0.244
11	0.93333333	0.39583333	10.8467193	7.05825333	14.7392396	0.2604825	0.05336344	0.58973735	-2.15454	1.5378
12	0.92916667	0.47916667	10.5591333	6.68993708	13.6682125	0.31819805	0.05693588	0.5282755	-0.7257	3.0488
13	0.9375	0.53333333	8.14549333	3.9704625	9.60745333	0.39815058	0.04673469	0.45681637	5.2318	5.6364
14	0.94166667	0.66666667	7.14704	4.353955	7.82446667	0.30254	0.0372713	0.28849012	20.0448	10.7892
15	0.9375	0.75	4.98368	2.63306875	3.6772	0.14076805	0.03175217	0.1544371	28.8727	14.00415
16										

	AO	AP	AQ	AR	AS	AT	AU	AV	AW	AX
1	P_radial50	P_ex_30ms	P_ex_40ms	P_ex_50ms		P_total_30ms		P_total_40ms		P_total_50ms
2	-1.28947	1.515	2.88	1.701	2.9	17.8919391	2.9	17.6974868	2.9	23.2580649
3	-0.8041	1.452	2.556	1.581	5.3	18.7976197	5.3	14.7748903	5.3	21.9473496
4	0.96664	1.527	2.622	1.716	9.3	22.159749	9.3	14.4514199	9.3	23.6019211
5	4.64121	1.998	2.058	2.037	13.4	40.549798	13.4	12.2629524	13.4	29.2075344
6	16.812	2.466	2.241	2.604	17.7	45.7168886	17.7	17.9272329	17.7	41.7246071
7	21.638925	1.794	1.896	2.055	22.4	34.6895802	22.4	21.7228111	22.4	52.6634419
8										
9	P_radial50	P_ex_30ms	P_ex_40ms	P_ex_50ms		P_total_30ms		P_total_40ms		P_total_50ms
10	-3.922	2.01	3.6	2.31	2.9	21.4506274	2.9	14.1896301	2.9	49.420504
11	-0.7482	1.95	3.6	2.28	5.3	21.7251618	5.3	14.8702168	5.3	47.9371769
12	1.195	1.92	3.63	2.28	9.3	26.3794714	9.3	16.264333	9.3	43.178988
13	5.1528	2.19	3.42	2.13	13.4	46.9933639	13.4	16.4080972	13.4	47.5249097
14	24.9102	3	3.75	3.6	17.7	63.20038	17.7	22.2641763	17.7	69.1671568
15	30.2348	3.3	3.21	4.5	22.4	61.420148	22.4	23.0087209	22.4	66.3764371
16										

	AY	AZ	BA	BB	BC	BD
1		P_west_ICRH	P_east_ICRH		Total_p_west	Total_p_east
2	2.9	0.19445229	5.56057812	0.0264	0.00513354	0.14679926
3	5.3	4.02272941	7.17245929	0.0618	0.24860468	0.44326798
4	9.3	7.70832905	9.1505012	0.1835	1.41447838	1.67911697
5	13.4	28.2868456	16.944582	0.2924	8.27107364	4.95459578
6	17.7	27.7896557	23.7973741	0.4201	11.6744343	9.99727688
7	22.4	12.9667692	30.9406308	0.5921	7.67762403	18.3199475
8					29.2913486	35.5409944
9		P_west_ICRH	P_east_ICRH		Total_p_west	Total_p_east
10	2.9	7.26099727	35.2308739	0.0264	0.19169033	0.93009507
11	5.3	6.85494506	33.0669602	0.0618	0.4236356	2.04353814
12	9.3	10.1151384	26.914655	0.1835	1.8561279	4.9388392
13	13.4	30.5852667	31.1168125	0.2924	8.94313199	9.09855598
14	17.7	40.9362037	46.9029805	0.4201	17.1972992	19.7039421
15	22.4	38.4114271	43.3677162	0.5921	22.743406	25.6780248
16					51.355291	62.3929952

Appendix C

Code Input Listings

Herein are listed the input files used for the ANTENA and GARFIELD code runs discussed in Chapter 8. Definition of the various parameters are given in the references.

The following is the input to GARFIELD, with conditions modeling the experimental conditions:

```
TMX East Ant. ICRH Fields for UPIC12 Case
itype="general" igrid="flux" npsi=41 nchi=141 istp=0 nblk=2
rmax=0.60 zedge=0. zmin= -4.2 zmax=+7.0 rjac=1. bsol=0.220 ncur=8
cur= 1.26e6 1.26e6 7.80e5 7.80e5 1.20e5 1.20e5 1.36e6 1.36e6
rc= .457 .457 2.30 2.30 1.35 1.35 .457 .457
zc= -4.1 +4.1 -3.52 +3.52 -5.65 5.65 -6.99 6.99
ivac=0 narc=0 nic=10
rin= .283 .283 .399 .382 .276 .264 .248 .237 .207 .198
zin= 1.80 1.80 1.65 2.05 1.65 2.05 1.65 2.05 1.65 2.05
cin= 0.5 0.5 -.030 -.030 -.200 -.200 -.150 -.150 -.100 -.100
dmax=1.7e18 dedge=.005 dcoef1=8. dcoef2=5000. dend=-.226
frat=1.05 cfrat=0.0015
nions=1 xmass=2. xchrg=1. drat=1.
maxit=2 errlim=1.e-10 m0=-3 mend=+3 minc=2
nplt=1 pltscale=10. nsurf=21 nrout=3  znout= 1.40 1.85 5.65
ieqdsk="eqdske" irfdsk="rfdske"
$end
```

The input deck with increased ion collisionality is exactly the same as the above, with the change of the parameter, "cfrat", from 0.0015 to 0.015.

The input to ANTENA used for the runs shown in Chapter 8 is listed below:

```
*  west loop radial scan with 9-layer profile
*  freq=2.55e6
*234567890123456789012345678901234567890123456789012345678901234567890
icoord=1        ibfld=1         iefld=1         iedotj=1        ipabs=1
indvar=1        ivarlow=0.5     ivarhi=24.5     ivarinc=2.0
ispectr=0       ifield=2        integkz=2       ifast=1         islow=1
kmincm=1.e-5    kmaxcm=10.
nmax=7
$
acm=25.0        ccm=52.500
rhocm=5.        phideg=45.0     zcm=20.
wnor=.87       freq=2.55e6
ncoils=4
icoil=    6 6 6 6
iseries=0       iparall=0       imutual=0       iantcon=0       nstep=3
cur=     (100.0,0.0) (-100.0,0.0) (-100.0,0.0) (100.0,0.0)
bcm=            29.6  44.  29.6  44.
widcm=          13.0 13.0 13.0 13.0
angdeg=         171. 171. 171. 171.
z0cm=             0.   0.   0.   0.
phi0deg=          0.   0.  180.  180.
$
*234567890123456789012345678901234567890123456789012345678901234567890
ikij=1          npart=2         bfld=3840.      ntot=1.2e12
mass=           2.              5.447e-4
charge=         1.              -1.
conc=          100.            100.
tpar=          100.             40.
tper=          100.             40.
colfreq=        1.5e3           3.5e5
iprof=4         nstrat=8
rs=   5.0    10.0    15.0    17.0    19.0    21.0    23.0    25.0
fden= 1.0     0.9     0.85    0.77    0.65    0.40    0.3     0.2
ftemp=          1.0             1.0             1.0
```

```
                .8          .8          1.0
                .8          .8          1.0
                .8          .8          1.0
                .8          .5          1.0
                .7          .5          1.0
                .6          .5          1.0
                .5          .5          1.0
*234567890123456789012345678901234567890123456789012345678901234567890
$
```

Again, this models the collision frequencies for the experimental conditions. The modified case is the same as the above, except that the parameter "colfreq" is changed from 1.5e3 and 3.5e5 to 1.5e4 and 3.5e4.

Bibliography

[1] T. K. Fowler and B. G. Logan, *Tandem Mirror Reactor*, Comments Plasma Phys. Controlled Fusion, **2**, p167 (1976).

[2] G. I. Dimov, V. V. Zakaidakov, and M. E. Kishinevsky, Fizika Plasmy, **2**, p597 (1976).

[3] F. F. Chen, *Introduction to Plasma Physics*, Plenum Press, New York, p202 (1974).

[4] D. R. Nicholson, *Introduction to Plasma Theory*, John Wiley & Sons, New York, pp17-29 (1983).

[5] L. Spitzer, Jr., *Physics of Fully Ionized Gases*, 2nd Ed., Interscience Publishers, New York (1962).

[6] D. E. Baldwin, *End-Loss Processes from Mirror Machines*, Reviews of Modern Physics, **49**(2), p317 (1977).

[7] R. H. Cohen, et al., Nuclear Fusion, **18**, 1229 (1978).

[8] D. E. Baldwin and B. G. Logan, Phys. Rev. Lett. *43*, p1318 (1979).

[9] L. V. Berzins and T. A. Casper, *Ion Microinstability at the Outer Sloshing-Ion Turning Point of TMX-U*, Phys. Rev. Letters, **59**(13), p1428 (1987).

[10] T. C. Simonen, et al., *Operation of the Tandem-Mirror Plasma Experiment with Skew Neutral-Beam Injection*, Phys. Rev. Letters, p1668 (1983).

[11] D. E. Baldwin, *Drift Pumping of Thermal Barriers*, Invited paper presented at meeting of Am. Phys. Soc., Div. Plasma Physics, New York (1981).

[12] D. L. Correll, et al., *Throttle Coil Operation of TMX-U*, LLNL, UCID-19650, p133 (1983).

[13] D. L. Goodwin, R. S. Post, D. L. Smatlak, and D. K. Smith, *RF Pumping on CONSTANCE*, Bull. Am. Phys. Soc., p1270 (1984), and p1489 (1985).

[14] TMX-U Major Project Proposal, F. H. Coensgen, et al., LLNL, LLL-PROP-172 (1980).

[15] D. E. Baldwin, B. G. Logan, T. C. Simonen, eds, *Physics Basis for MFTF-B*, LLNL, UCID-18496 (Jan. 1980).

[16] T. C. Simonen, et al, *Plasma Physics and Controlled Nuclear Fusion Reasarch, 1986*, Vol. 2, IAEA, Vienna, pp231-241 (1987).

[17] L. S. Hall and B. McNamara, *Three-Dimensional Equillibrium of the Anisotropic Finite-Pressure, Guiding-Center Plasma: The Theory of the Magnetic Plasma*, Physics of Fluids, **18**(5), p552 (1975).

[18] TMX-U Final Report, G. D. Porter, ed., LLNL, UCID-20981 (1987).

[19] R. Eisberg and R. Resnick, *Quantum Physics*, John Wiley & Sons, New York, p108 (1974).

[20] L. C. Johnson and E. Hinnov, *Ionization, Recombination, and Population of Excited Levels in Hydrogen Plasmas*, J. Quant. Spectrosc. Radiat. Transfer, **13**, pp333-358, (1973).

[21] I. Langmuir, Phys. Rev., **28**, p727 (1926).

[22] R. H. Huddlestone and S. L. Leonard, eds., *Plasma Diagnostic Techniques*, Academic Press, New York, pp113-199 (1965).

[23] R. S. Hornady, in *Summary of TMX-U Results: 1984*, Vol. 2, T. C. Simonen, Ed., Lawrence Livermore National Laboratory, Livermore, CA, UCID-20274, p7.145 (1984).

[24] J. H. Foote et al., Rev. Sci. Instrum., **56**(5), p1117 (1985).

[25] J. H. Foote et al., Rev. Sci. Instrum., **57**(8), p1786 (1986).

[26] M. R. Carter, *Plasma Potential Measurements in TMX-U Using a Time-of-Flight Neutral Particle Analyzer*, Ph.D. Dissertation, LLNL, UCRL-53834 (Nov. 1987).

[27] W. M. Hooke, F. H. Tenney, M. H. Brennan, H. M. Hill, T. H. Stix, *Experiments on Ion Cyclotron Waves*, Phys. Fluids, **4**, p1131 (1961).

[28] J. C. Hosea and R. M. Sinclair, *Ion Cyclotron Wave Generation in the Model C Stellerator*, Phys. Fluids **13**, 701 (1970).

[29] A. W. Molvik et al., *Initial TMX Central-Cell ICRH Experiments*, LLNL, UCID-18866 (1980).

[30] R. Bruen, S. N. Golovato, L. Yujiri, B. McVey, A. W. Molvik, D. Smatlak, R. S. Post, D. K. Smith, N. Hershkowitz, *Experiments in a Tandem Mirror Sustained and Heated Solely by RF*, Phys. Rev. Lett., **47**, p1833 (1981).

[31] A. P. Biddle and J. C. Sprott, *High Power Heating in the Ion Cyclotron Range of Frequencies in the Wisconsin Tokapole II*, Plasma Physics, **23**, No. 8, pp679-691 (1981).

[32] S. N. Golovato, B. D. McVey, J. E. Scharer, R. A. Bruen, D. K. Smith, J. Yugo, L. Yujiri, *Plasma Heating at Twice the Ion Cyclotron Frequency in a Quadrupole Minimum-B Mirror*, Nuclear Fusion, **22**, No. 6, p741 (1982).

[33] T. L. Owens, et al., *Heating Experiments in the Ion Cyclotron Range on Frequencies on EBT-S*, Nuclear Fusion, **23**, No. 1, p49 (1983).

[34] S. N. Golovato, et al., *Fueling and Heating of Tandem Mirror End Cells Using RF at the Ion Cyclotron Frequency*, Phys. Fluids, **28** (2), p734 (1985).

[35] A. W. Molvik, S. Falabella, et al., *ICRF Heating in the Tandem Mirror Experiment-Upgrade*, LLNL, UCRL-90096.

[36] J. Dawson, *On Landau Damping*, Phys. Fluids, **4**, p869 (1961).

[37] T. H. Stix, *The Theory of Plasma Waves*, McGraw-Hill Book Company, New York (1962).

[38] P. L. Bhatnagar, E. P. Gross, and M. Krook, Physical Review, **94**, p511 (1954).

[39] H. Alfvén, *On the Existence of Electromagnetic-Hydrodynamic Waves*, Arkiv. Mat. Astrom. Fysik, **29B**(2) (1942).

[40] K. Appert, J. Vaclavik, and L. Villard, Phys. Fluids, **27** (2), pp432-437 (1984).

[41] B. D. McVey, *Excitation Theory of the Inductive Drive*, TRW Report Task II, 2740 (1980).

[42] B. D. McVey, *ICRF Antenna Coupling Theory for a Cylindrically Stratified Plasma*, MIT Report No. PFC/RR-84-12 (1984).

[43] M. W. Phillips, A. M. M. Todd, Computer Physics Communication, **40**, p65-72 (1986).

[44] R. R. Mett, *A Comparison of Measured and Computed Plasma Loading Resistances in the TMX-U Central Cell*, LLNL, UCID-20051 (1984).

[45] A. W. Molvik and S. Falabella, *Use of ICRH for Startup and Initial Heating of the TMX-U Central Cell*, LLNL, UCID-19342 (1982).

[46] D. R. Whaley, *Results of McVey Code Runs for TMX-U ICRH Loop Antennas*, LLNL, M-Division Memorandum (July 23, 1985).

[47] S. W. Fergusen, *Ion Cyclotron Resonant Heating System used on TMX-U*, LLNL, UCRL-92518 (1985).

[48] M. Makowski, *FREA Test Report*, TRW Report PSP-TR-350 (Apr., 1985).

[49] J. J. Thomson, *REA Current Traces*, TRW Report PSP-5404 (Feb., 1983).

[50] I. Katsumata and M. Okazaki, *Ion Sensitive Probe - A New Diagnostic Method for Plasma in Magnetic Fields*, Japan J. Appl. Phys., **6**, p123-124 (1967).

[51] R. W. Motley and T. Kawabe, *Energy Analysis of Cesium Ions in a Q Machine*, Physics of Fliuds, **14**, p1019 (1971).

[52] M. J. McCarrick, R. F. Ellis, M. Koepke, and R. P. Majeski, Rev. Sci. Instrum., **56**, p1463 (1985).

[53] R. P. daSilva, I. C. Nascimento, and D. F. daCruz, Jr., A. Hershcovitch, *Electrostatic Ion Probe for Tokamak-Plasma-Edge Diagnostic*, Rev. Sci. Instrum., **9**, p2205 (1986).

[54] P. R. Bevington, *Data Reduction and Error Analysis for the Physical Sciences*, McGraw-Hill, New York (1969).

[55] R. L. Freeman and E. M. Jones, CLM-R 137, Culham Lab., Abingdon, Perkshire, England (1974).

[56] D. Heifetz, et al., *A Monte-Carlo Model of Neutral-Particle Transport in Diverted Plasmas*, Journal of Computational Physics, **46**, pp309-327, (1982).

[57] S. A. Allen, LLNL, private communication

[58] W. T. Miles, R. Thompson, and A. E. S. Green, *Electron-Impact Cross Sections and Energy Deposition in Molecular Hydrogen*, J. App. Phys., **43**, p678 (1972).

[59] G. Dimonte, A. W. Molvik, J. Barter, W. F. Cummins, S. Falabella, P. Poulsen, T. Romesser, *Ion Cyclotron Heating in TMX-U*, Nuclear Fusion, **27**(12), p1959 (1987).

[60] F. J. Paoloni, Phys. Fluids, **18**, p640 (1975).

[61] P. C. Stangby, *Edge Probes*, J. Nuc. Mat., **145-147**, p106 (1987).

[62] V. P. Pastukhov, Nucl. Fusion, **14**, p3 (1974).